Topics in LIGO-Related Physics: Interferometric Speed Meters and Tidal Work

Thesis by

Patricia Marie Purdue

In Partial Fulfillment of the Requirements

for the Degree of

Doctor of Philosophy

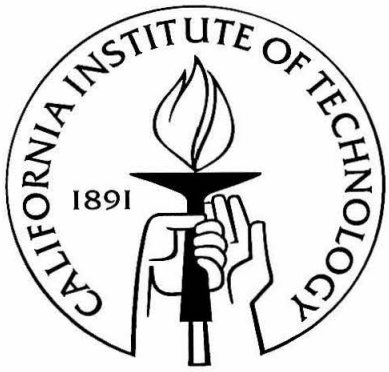

California Institute of Technology

Pasadena, California

2003

(Defended June 18, 2002)

Acknowledgements

First and foremost, I would like to thank my advisor Kip Thorne for suggesting research problems, offering helpful advice about their solutions, and improving the prose of my papers. I feel honored to have had the opportunity to work with him, as he has been a very supportive and patient mentor. I hope that I can do as well with my students.

Many thanks also go to my collaborator, Yanbei Chen, without whose efforts Chapter 3 would not have been finished in a such a timely manner. His abilities provided an excellent counterpoint to my own. I have also appreciated helpful discussions with Stan Whitcomb, Farid Khalili, Alessandra Buonanno, and numerous others.

I have benefitted, in one way or another from the advice, support, and/or friendship of various others along the way, including Teviet Creighton, Shane Larson, Scott Hughes, Michele Vallisneri, Kashif Alvi, and the other Kiplings. Also, I think Chris Mach for keeping my computer running, Jo-Ann Ruffolo for enthusiastic support and advice during my job search, and Shirley Hampton and Donna Driscoll for their help with the bureaucracy.

Others who have helped make my time at Caltech more enjoyable include Eileen Lau, Pu Chen, Michelle Larson, Janice Yeung, Ravinder Bhatia. Also, I am grateful for the opportunity to study taiji under two very talented and accomplished instructors, Master Ming (Helen) Zhu and Master Lijun Wang.

Finally, I thank my family for their long support of me and my education. I'm fortunate to follow in the footsteps of my father and grandfather, who always encouraged my curiosity and persistence, to become a third generation science Ph.D. I've also been incredibly lucky to have some remarkable women to look up to. My mother and step-mother have always taught me, and tried to demonstrate, that women can do anything. My two grandmothers did not live long enough to see this achievement, but they always loved to hear about my progess and never stopped believing I would reach my goal. I am also grateful for the rest of my family and the acceptance and encouragement they have provided over the years.

In addition, this work was supported in part by a Special Institute Scholarship for my first year, plus NSF Grant AST-9731698, NASA Grant NAG5-6840, and NSF Grant PHY-0099568.

Abstract

In the quest to develop viable designs for third-generation optical interferometric gravitational-wave detectors, one strategy is to monitor the relative momentum or speed of the test-mass mirrors, rather than monitoring their relative position. The most straightforward design for a *speed-meter interferometer* that accomplishes this is described and analyzed in Chapter 2. This design (due to Braginsky, Gorodetsky, Khalili, and Thorne) is analogous to a microwave-cavity speed meter conceived by Braginsky and Khalili. A mathematical mapping between the microwave speed meter and the optical interferometric speed meter is developed and used to show (in accord with the speed being a quantum nondemolition observable) that *in principle* the interferometric speed meter can beat the gravitational-wave standard quantum limit (SQL) by an arbitrarily large amount, over an arbitrarily wide range of frequencies. However, *in practice*, to reach or beat the SQL, this specific speed meter requires exorbitantly high input light power. The physical reason for this is explored, along with other issues such as constraints on performance due to optical dissipation.

Chapter 3 proposes a more sophisticated version of a speed meter. This new design requires only a modest input power and appears to be a fully practical candidate for third-generation LIGO. It can beat the SQL (the approximate sensitivity of second-generation LIGO interferometers) over a broad range of frequencies ($\sim$ 10 to 100 Hz in practice) by a factor $h/h_{\rm SQL} \sim \sqrt{W_{\rm circ}^{SQL}/W_{\rm circ}}$. Here $W_{\rm circ}$ is the light power circulating in the interferometer arms and $W_{\rm SQL} \simeq 800$ kW is the circulating power required to beat the SQL at 100 Hz (the LIGO-II power). If squeezed vacuum (with a power-squeeze factor e^{-2R}) is injected into the interferometer's output port, the SQL can be beat with a much reduced laser power: $h/h_{\rm SQL} \sim \sqrt{W_{\rm circ}^{SQL}/W_{\rm circ}e^{2R}}$. For realistic parameters ($e^{2R} \simeq 10$ and $W_{\rm circ} \simeq 800$ to 2000 kW), the SQL can be beat by a factor ~ 3 to 4 from 10 to 100 Hz. [However, as the power increases in these expressions, the speed meter becomes more narrow band; additional power and re-optimization of some parameters are required to maintain the wide band.] By performing frequency-dependent homodyne detection on the output (with the aid of two kilometer-scale filter cavities), one can markedly improve the interferometer's sensitivity at frequencies above 100 Hz.

Chapters 2 and 3 are part of an ongoing effort to develop a practical variant of an interferometric speed meter and to combine the speed meter concept with other ideas to yield a promising third-

generation interferometric gravitational-wave detector that entails low laser power.

Chapter 4 is a contribution to the foundations for analyzing sources of gravitational waves for LIGO. Specifically, it presents an analysis of the tidal work done on a self-gravitating body (e.g., a neutron star or black hole) in an external tidal field (e.g., that of a binary companion). The change in the mass-energy of the body as a result of the tidal work, or "tidal heating," is analyzed using the Landau-Lifshitz pseudotensor and the local asymptotic rest frame of the body. It is shown that the work done on the body is gauge invariant, while the body–tidal-field interaction energy contained within the body's local asymptotic rest frame is gauge dependent. This is analogous to Newtonian theory, where the interaction energy is shown to depend on how one localizes gravitational energy, but the work done on the body is independent of that localization. These conclusions play a role in analyses, by others, of the dynamics and stability of the inspiraling neutron-star binaries whose gravitational waves are likely to be seen and studied by LIGO.

Contents

Acknowledgements iii

Abstract iv

1 Introduction and Overview 1

1.1 Background on Interferometric Speed Meters 1

1.1.1 Conventional Interferometric Gravitational-Wave Detectors 1

1.1.2 Standard Quantum Limit 4

1.1.3 Beating the SQL 5

1.1.4 Initial Design for Interferometric Speed Meter 6

1.1.5 Practical Interferometric Speed Meter 6

1.2 Background on Tidal Work 8

1.2.1 Context 8

1.2.2 Description of Slow-Motion, Isolated-Body Formalism 9

1.2.3 Mass-Energy Ambiguity and Tidal-Work Uniqueness 10

1.3 Bibliography 11

2 Analysis of a Quantum Nondemolition Speed-Meter Interferometer 15

2.1 Summary 15

2.2 Introduction 16

2.3 Mathematical Description of the Interferometer 20

2.3.1 Carrier Light 21

2.3.2 Sideband Light 22

2.4 Speed Meter in the Lossless Limit 24

2.4.1 Mathematical Analysis 24

2.4.2 Numerical Analysis 30

2.4.3 Discussion of Lossless Speed Meter 30

2.5 Sensitivity of Speed Meter with Losses 34

2.6 Conclusions 36

2.7 Bibliography 38

3 Practical Speed-Meter Designs for QND Gravitational-Wave Interferometers 40

3.1 Summary 40
3.2 Introduction 41
3.3 Mathematical Description of the Interferometer 49
3.4 Speed Meter in the Lossless Limit 50
3.4.1 Mathematical Analysis 51
3.4.2 Optimization 54
3.4.3 Discussion of Three-Cavity Speed-Meter Design 58
3.5 Squeezed Vacuum and FD Homodyne Dectection 61
3.5.1 Injection of Squeezed Vacuum into Dark Port 61
3.5.2 Frequency-Dependent Homodyne Detection 63
3.6 Optical Losses 65
3.6.1 Internal losses 65
3.6.2 Internal and External Losses in Compact Form 67
3.6.3 Performance of Lossy Speed Meters and Comparisons with Other Configurations 70
3.7 Conclusions 74
3.8 Bibliography 75

4 The Gauge Invariance of General Relativistic Tidal Heating 78

4.1 Summary 78
4.2 Introduction 78
4.3 Newtonian Analysis 81
4.4 Relativistic Analysis 85
4.4.1 deDonder Gauge 86
4.4.2 General Gauge 89
4.5 Conclusions 91
4.6 Bibliography 92

A FP Cavities as Optical Filters 94

B Semi-Analytical Treatment of the Loss Terms 97

B.1 Arms, Extraction Mirror, and Sloshing Cavity (AES) 97
B.2 Port-Closing Mirror 98
B.3 The RSE Cavity 99
B.4 Detection and Filter Cavities 102

C Effects due to Mode-Mismatching: A Simple Analysis **104**

D Transmissivity Mismatch between the Internal Mirror and the RSE Mirror **108**

List of Figures

1.1 Conventional LIGO interferometer design 3

2.1 Design for a QND speed-meter interferometer 18
2.2 Squared amount by which the speed meter beats the standard quantum limit 29
2.3 Lossless noise curve for speed meter 31
2.4 Plot of ξ^2 for the lossless speed meter with varying amounts of power in the "empty" cavity 34
2.5 Plot of ξ^2 for the speed meter with losses 37

3.1 Comparison of typical noise curves (with losses) for several interferometer configurations 42
3.2 Simple version of three-cavity design for speed-meter interferometer 44
3.3 Practical three-cavity speed-meter design 47
3.4 Squeezed-variational three-cavity speed-meter design 48
3.5 Typical curves for the coupling constant $\kappa(\omega)$ in terms of the sloshing frequency Ω . . 53
3.6 Typical curves for the coupling constant $\kappa(\omega)$ in terms of the optimal frequency $\omega_{\rm opt}$. 55
3.7 Squared amount by which the speed meter beats the SQL 56
3.8 Noise curves corresponding to the ξ^2 curves in preceding plot 57
3.9 Noise curves for varying optimal frequencies 59
3.10 Comparison of typical noise curves for frequency-dependent and fixed-angle homodyne detection 65
3.11 Moduli-squared of the loss factors 70
3.12 Noise curves showing the effects of losses 71
3.13 Comparison of noise curves of a conventional interferometer and a speed meter 72
3.14 Comparison of the speed meter's κ^* with the position meter's $\mathcal{K}_*$ 74
3.15 Comparison of noise curves for a squeezed-variational position meter and speed meter 75

4.1 Schematic diagram for tidal heating analysis 82

B.1 Schematic diagram for RSE loss 100

List of Tables

2.1 Mapping of the parameters in the BGKT microwave-resonator speed meter paper to those in this chapter 26
2.2 Interferometer parameters and their fiducial values 30

3.1 Three-arm speed-meter interferometer parameters and their fiducial values 60
3.2 Loss factors due to shot noise and radiation pressure for each type of cavity in the interferometer 68
3.3 Fiducial values for the fractional losses 69

Chapter 1

Introduction and Overview

This thesis consists of two main topics—interferometric speed meters as candidates for third-generation gravitational-wave detectors (Chapters 2 and 3) and tidal work in binary systems (Chapter 4). Accordingly, this introduction will be divided into two main sections to provide background for each subject.

1.1 Background on Interferometric Speed Meters

1.1.1 Conventional Interferometric Gravitational-Wave Detectors

Interferometric gravitational-wave detectors are essentially Michelson interferometers with Fabry-Perot-cavity arms where mirrors act as "test masses"—free particles that travel through the horizontal part of space-time on geodesics. Since, according to general relativity, gravity is the curvature of space-time and gravitational waves are ripples in that curvature, the test masses' geodesics will be changed by passing gravitational waves. In essence, gravity waves will cause the interferometer's mirrors to move relative to one another.

Around the world, there are several such detectors that have been built, are under construction, or are being planned. These are as follows.

- The Laser Interferometer Gravitational-Wave Observatory (LIGO) has two sites and three interferometers. The interferometer in Livingston, Louisiana, has arms 4 kilometers long, while the Hanford, Washington, site has a 2-kilometer and a 4-kilometer interferometer. LIGO's first interferometers (LIGO-I) have recently been brought into operation, and during 2002–03 are undergoing "debugging" interleaved with short data runs. Searches at design sensitivity are planned for 2004–05, followed by an upgrade to advanced interferometers (LIGO-II) in 2006–07 [1]; see below.

- The Japanese TAMA300 detector, with 300-meter arms, began operation in 2001 [2] and is now in the late stages "debugging" interleaved with short data runs; it has collected more than

1000 hours of data [3].

- GEO-600 is a German-British collaboration in Hanover, Germany. It is maintaining approximately the same schedule as LIGO; its current debugging interleaved with short data runs is being carried out in tight collaboration with LIGO—the data runs are carried out in coincidence and the data are analyzed jointly [4].

- VIRGO is a French-Italian collaboration and is located near Pisa, Italy. This detector is currently operating with an arm length of 8 meters and will be extended to 3-kilometer length by 2004 [5].

- The Large Cryogenic Gravitational Telescope (LCGT), a Japanese 3-kilometer interferometer is being planned as a follow-on to TAMA. It will be built underground at the site of current Japanese neutrino detectors and will likely go into operation late in this decade. Its test masses will be cryogenically cooled to control thermal noise [6].

- EURO, a pan-European follow-on to VIRGO and GEO600, is tentatively being planned for early in the next decade—the same time frame as a possible second upgrade of the LIGO interferometers (to "LIGO-III") [7]; see below.

My discussion will focus primarily on LIGO, which will start out with a "conventional" optical topology (see Fig. 1.1). Basically, the LIGO detectors will be Michelson interferometers with Fabry-Perot cavities in each 4-kilometer-long arm. The Fabry-Perot cavities cause the light to bounce multiple times, amplifying the gravity wave signal. (The cavities also permit high circulating powers to be used without having too much power flowing through the beam splitter, a fact which will be important in the interferometer described in Chapter 3.) The distances between the mirrors are adjusted so that, upon recombination at the beam splitter, the light returning from the arms has a relative phase such that (almost) all of the carrier light is directed back towards the laser. A power-recycling mirror placed between the laser and the beam splitter directs the carrier light back into the interferometer, boosting the circulating power. When a gravitational wave (or other force) moves the arm-cavity mirrors, that motion puts sidebands on the carrier; these sidebands exit through the dark port, where they are detected via an RF modulation/demodulation technique.

Since gravitational radiation causes a strain in space itself, the sensitivities of the interferometers are measured in terms of their sensitivity to that strain. The initial version of LIGO is expected to have a gravitational-wave strain sensitivity of $h \sim 10^{-21}$. Since the arms are 4 km long, this means that the interferometers will be sensitive to mirror displacements of $hL \sim (10^{-21})(4\text{ km}) = 4 \times 10^{-18}$ m. There is a planned upgrade (LIGO-II) in 2007, which should increase the sensitivity by about a factor of 15. An important difference between the LIGO-I and *LIGO-II interferometers*

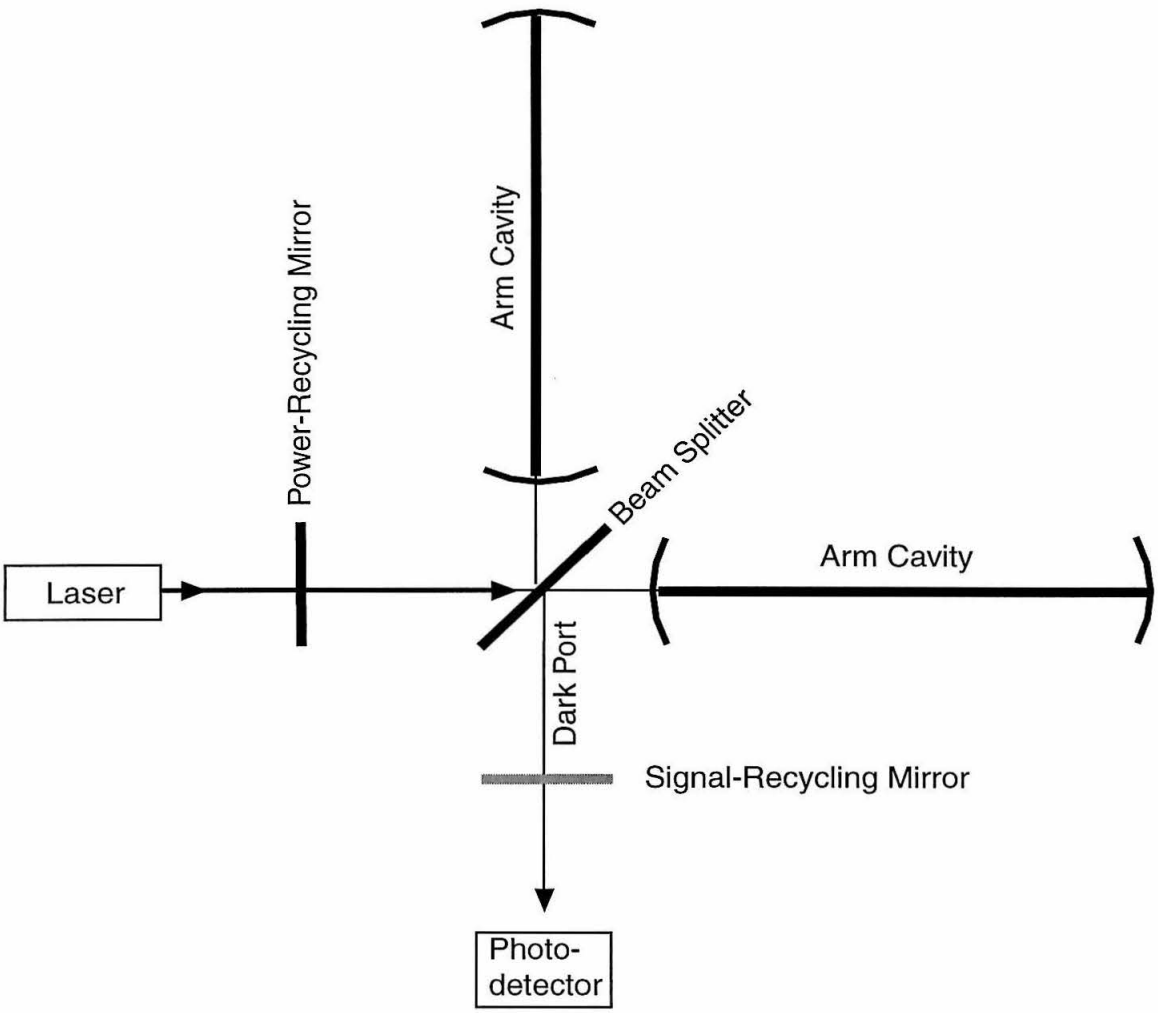

Figure 1.1: Schematic design for a conventional LIGO (position meter) interferometer, consisting of a Michelson interferometer with Fabry-Perot arm cavities. The mirror portrayed in gray is a signal-recycling mirror, which will be included in LIGO-II.

is a signal recycling mirror placed between the dark port and the photodetector to further amplify the signal (see Fig. 1.1) and alter the shape of the noise curve [8, 9].

This second-generation sensitivity will be near or modestly better than the *standard quantum limit* (SQL), a limit that constrains interferometers [10] such as LIGO-I which have conventional optical topology, but does not constrain more sophisticated "quantum nondemolition" (QND) interferometers [11, 12].

1.1.2 Standard Quantum Limit

To understand how the standard quantum limit arises, it is necessary to examine the role of the Heisenberg uncertainty principle in a conventional interferometer.

First, we can model the relative motion of the four "free-particle" test masses (each with mass m) as being the motion of a single free particle of mass $\mu = m/4$. Then suppose a single measurement of the position of this particle is made with accuracy Δx_1. According to the uncertainty principle, the laser light that performs this measurement will randomly "kick" the particle's momentum by an amount

$$\Delta p_1 \sim \frac{\hbar}{\Delta x_1} .$$

After a time τ has passed, another position measurement is made with accuracy Δx_2. This measurement will be affected by the momentum kick from the first measurement so that (*if* position and momentum are uncorrelated, as is the case in a conventional interferometer)

$$\Delta x_2 \gtrsim \Delta p_1 \frac{\tau}{\mu} \sim \left(\frac{\hbar}{\Delta x_1}\right)\left(\frac{\tau}{\mu}\right) .$$

Therefore,

$$\Delta x_1 \Delta x_2 \gtrsim \frac{\hbar\tau}{\mu} .$$

The best one can do is to balance the uncertainties of the two measurements; this optimal uncertainty corresponds to the standard quantum limit

$$(\Delta x)_{\rm SQL} = \Delta x_1 = \Delta x_2 \sim \sqrt{\frac{\hbar\tau}{\mu}} .$$

For LIGO (with 40-kilogram mirrors), this gives $(\Delta x)_{\rm SQL} \sim 10^{-19}$ m, a level of sensitivity that should be attainable with LIGO-II interferometers.

The goal of LIGO-III interferometers is to improve the sensitivity even further. Of course, achieving this goal means that methods—called *quantum nondemolition* (QND) techniques—must be devised to beat the SQL.

1.1.3 Beating the SQL

It is hoped that third-generation gravitational-wave interferometers will beat the SQL by a factor of ∼5 or more over a frequency band somewhat greater than the typical frequency of operation. Research on such third-generation detectors has entailed, thus far, the conception and theoretical exploration of a number of ideas that might prove useful in a final design. Examples of such QND techniques include

(i) injecting squeezed vacuum into an interferometer's dark port [11–13],

(ii) performing homodyne detection on the output light with frequency-dependent homodyne angle (achieved using large Fabry-Perot filter cavities together with conventional, frequency-independent homodyne detection) [14–19],

(iii) using light pressure to transfer the gravity-wave signal onto a small test mass that moves relative to local inertial frames and then reading out that motion using local QND techniques (the *Optical Bar*) [20, 21],

(iv) a variant of this involving *Symphotonic States* [22],

(v) another variant of the optical bar, the *Optical Lever* [23],

(vi) producing *Optical-Spring* behavior by means of a signal-recycling mirror [24, 25],

(vii) operating the interferometer as a *speed meter*, instead of a position meter (Chapters 2 and 3 of this thesis), and

(viii) changing the dynamics of the test-mass mirrors by other more general means [26, 27].

Since it has long been planned for LIGO-II to have a signal-recycling mirror (the gray mirror in Fig. 1.1), it is anticipated that LIGO-II will be able to operate as an optical spring [item (v) above] and beat the SQL by as much as a factor of 2 over a frequency band $\Delta f \sim f$ [24]—if thermoelastic noise can be made small enough [28, 29].

The goal for LIGO-III, however, is to achieve a sensitivity significantly better than the SQL over a wide band. Speed meters are capable of doing just that. To understand why, recall the manner in which the SQL arose from the uncertainty principle (Sec. 1.1.2). If the velocity (which is directly proportional to the momentum) of the test mass is measured instead of the position, then the velocity measurement will randomly kick the position. That position kick is irrelevant *if* the velocity is being measured without collecting position information, as in a speed meter. Another way to say this is to note that the velocity (or momentum) is a constant of the free motion of the test mass. Consequently, the velocity (unlike position) commutes with itself at different times and is therefore a QND observable [30, 31]. The result is that speed meters are not constrained by the SQL.

1.1.4 Initial Design for Interferometric Speed Meter

The original idea for a speed meter that measures the velocity of a single test mass was conceived, in a primitive form, by Braginsky and Khalili [32]. Braginsky, Gorodetsky, Khalili, and Thorne [33] (henceforth called BGKT) devised a refined and marginally practical form based on two coupled microwave cavities. In their appendix, BGKT also sketched a design for an optical-interferometer speed-meter gravity-wave detector that, they speculated, would be able to beat the gravity-wave SQL in essentially the same manner as the microwave speed meter beats the free-mass SQL.

In Chapter 2, I present a detailed analysis of the BGKT optical-interferometer speed meter, with the objective of determining whether it actually does measure the test masses' relative velocity without collecting position information and whether it actually can beat the SQL. As we shall see, the answers are both "yes." Moreover, I show that there is a mathematical mapping between the analysis of the microwave-cavity speed meter, which measures the velocity of a single mass, and that of the optical-interferometer speed meter, which measures the relative speeds of widely separated test masses. The main objective of my analysis is to explore the features of this optical-interferometer speed meter that are important in attempts to design practical third-generation interferometers.

This speed meter design is shown in Fig. 2.1 and introduced in more detail in Sec. 2.2. I show in Chapter 2 that, *in principle*, this design is capable of beating the SQL by an arbitrarily large amount, over an arbitrarily wide range of frequencies, and can do so without the use of squeezed vacuum or any auxiliary filter cavities at the interferometer's input or output (see Fig. 2.2 or 2.3). However, *in practice*, optical losses will limit the amount by which the SQL can be beaten, and to beat the SQL at all, this speed meter requires an uncomfortably high circulating power[1]. In addition, this design requires an exorbitantly high input laser power, rendering it quite impractical for use in LIGO. Nevertheless, the analysis of this speed meter has motivated the invention of a more practical interferometric speed meter.

1.1.5 Practical Interferometric Speed Meter

While the speed meter design described in Chapter 2 is clearly impractical because of the laser powers involved, Yanbei Chen—leaning heavily on my analysis of the original speed meter—has devised an altered form of speed meter that solves the problem of the high input power and appears to be fully practical. Together we have analyzed this improved speed meter, as described in Chapter 3 (which was largely written by me based on our joint analysis). Like the original interferometric speed meter, this design can beat the gravitational-wave standard quantum limit (SQL) by an arbitrarily large amount, over an arbitrarily wide range of frequencies, but it eliminates the high input power problem.

[1] This is actually a common feature of designs that beat the SQL [34]. See Sec. 3.4.3 for a more detailed discussion.

This new speed meter can beat the standard quantum limit (the approximate sensitivity of second-generation LIGO interferometers, LIGO-II) over a broad range of frequencies ($\sim$ 10 to $f_{\rm opt} \simeq$ 100 Hz in practice) by a factor $h/h_{\rm SQL} \sim \sqrt{W_{\rm circ}^{SQL}/W_{\rm circ}}$. Here $W_{\rm circ}$ is the light power circulating in the interferometer arms and $W_{\rm circ}^{SQL} \simeq (800\ {\rm kW})(f_{\rm opt}/100\ {\rm Hz})^3$ is the circulating power required to reach the SQL (the LIGO-II power) at some "optimal" frequency $f_{\rm opt}$. If squeezed vacuum (with a power-squeeze factor e^{-2R}) is injected into the interferometer's output port, the SQL can be beat with a much reduced laser power: $h/h_{\rm SQL} \sim \sqrt{W_{\rm circ}^{SQL}/W_{\rm circ}e^{2R}}$. For realistic parameters ($e^{2R} \simeq 10$ and $W_{\rm circ} \simeq$ 800 to 2000 kW), the SQL can be beat by a factor of $\sim$ 3 to 4 from about 10 Hz to $f_{\rm opt} \simeq$ 100 Hz. [It should be noted that, as the power increases in these simple expressions, the speed-meter performance becomes more narrow band. Additional power and a re-optimization of some of the speed meter's parameters are required to maintain this wide band at higher sensitivities. See Sec. 3.4.2 for details.] By performing frequency-dependent homodyne detection on the output (with the aid of two 4-kilometer-long filter cavities), one can markedly improve the interferometer's sensitivity at frequencies above $f_{\rm opt}$.

In most other proposed designs for LIGO-III interferometers (e.g., the squeezed-variational interferometers of Kimble *et al.* [19]), a crucial role is played by "ponderomotive squeezing" of the signal light—squeezing that is easily destroyed by ordinary vacuum which leaks into the interferometer at all "dissipation locations" (locations where signal light can leak out, e.g., via light scattering or absorption). In Chapter 3, Chen and I analyze the effects of such dissipation on our new speed meter. We find that our interferometer's performance is degraded much less by dissipation than are the performances of other proposed LIGO-III interferometers (particularly those described in Ref. [19]). This appears to be because the key to our interferometer's beating of the SQL is its measurement of momentum, which is achieved without any crucial reliance on ponderomotive squeezing.

More specifically, our analysis indicates that losses for our speed meter are due primarily to the losses in the optical elements (as opposed to mode-mismatching effects). Since the mirrors and beam splitters that comprise the speed meter are expected to have fractional losses of order $\lesssim 2\times10^{-5}$ [19], we find that, without squeezed vacuum, the effect of losses on the sensitivity (measured in terms of the the spectral density of the noise $\sqrt{S_h(f)}$ in units of ${\rm Hz}^{-1/2}$) is less than 10% in the range 50–105 Hz. At higher frequencies, the effect is even smaller, but the sensitivity degrades at low frequencies. Injecting fixed-angle squeezed vacuum into the dark port allows this speed meter to operate at a lower power, thereby reducing the dominant losses (which come from the additional radiation pressure caused by vacuum that has leaked into the interferometer). In this case, the losses are less than 4% in the range 25–150 Hz. As before, they decrease at high frequencies, and they increase at low frequencies. Using frequency-dependent homodyne detection increases the losses by a few percent across the entire frequency band. For sample noise curves, please see Fig. 3.1.

1.2 Background on Tidal Work

Chapter 4 represents a very different direction of research. It is part of an effort to develop and understand the "slow-motion, isolated-body formalism" for analyzing a self-gravitating body interacting with an external tidal field (as occurs in a binary star system, for example). Section 1.2.1 outlines the development of this formalism and a controversy that spurred recent additional work on the subject. Section 1.2.2 gives a brief description of the formalism itself, which is followed by a description of my contribution in Sec. 1.2.3.

1.2.1 Context

The slow-motion, isolated-body formalism has been developed in a series of papers:

1. The book *Gravitation* [35], Section 20.6 (written by John Wheeler), laid the conceptual foundations for analyzing the motion of an isolated body through the external universe.

2. Thorne [36] developed the theory of multipole moments of an isolated body in the form later used by Thorne and Hartle (see item 3).

3. Thorne and Hartle [37] formulated the problem of analyzing the effects of the external universe's tidal fields on an isolated body, and conceived and initiated the development of the perturbative formalism for studying the influence of the tidal fields on the body's motion through the external universe, the precession of its spin axis, and its changes of mass-energy.

4. Zhang [38] extended the Thorne-Hartle analysis of motion and precession to include higher order moments than they considered.

5. Zhang [39] developed the theory of multipole moments for the external universe's tidal gravitational fields, which underlies the work of Thorne and Hartle.

6. Thorne [40] and Flanagan [41] initiated the study of tidally induced volume changes and accompanying mass-energy change in the isolated body, using the above formalism. An important piece of Thorne's analysis came from examining the work done on each star by its companion's tidal field—i.e., an analysis of "tidal heating"[2].

7. Purdue (Chapter 4) revisited an issue regarding a possible ambiguity in the definition of tidal heating; this issue was raised initially by Thorne and Hartle and re-emerged in connection with Thorne's analysis of tidally induced changes in an isolated body. In Chapter 4, I demonstrated

[2]It should be noted that the term "tidal heating" is a bit of a misnomer; the more correct term is "tidal work." "Tidal heating" has been commonly used because the gravitational energy that is transfered between the body and the external field often goes into heat (as, e.g., in the moons of Jupiter). However, the energy added to the body via tidal work may instead deform the body or add vibrational energy. Nevertheless, I will use the terms "tidal heating" and "tidal work" interchangeably to mean the work done by an external tidal field on an isolated body.

that the tidal work is unambiguous in Newtonian theory and unaffected by a gauge change in general relativity. A key tool in my analysis is the Landau-Lifshitz stress-energy pseudotensor.

8. Favata [42] showed that the tidal work is independent of the pseudotensor one uses in computing it.

The impetus for the later work on this topic (items 6–8 above) came from some numerical solutions of Einstein's equations by Wilson, Mathews, and Maronetti [43–45] (WMM), which seemed to show each neutron star in a massive inspiraling binary being compressed to the point of collapse by gravitational interaction with its companion. The surprising nature of these results prompted many other researchers to examine the issue, most failing to reproduce a star-crushing effect of the same magnitude (for example, Refs. [40, 41, 46–53]). Two of these papers, specifically Thorne [40] and Flanagan [41], used the slow-motion, isolated-body formalism, as mentioned in item 6 above. (They were among those who did not find a star-crushing effect of the large magnitude seen in the numerical solutions.) In a later paper, Flanagan [54] identified an error in the original WMM analysis. Upon correcting their code, WMM found that the amplitude of the star-crushing effect they had seen was significantly reduced, but the crushing was still present [55, 56]. Recent work by Favata and Thorne [57], again using the slow-motion, isolated-body formalism (and relying on the results in Chap. 4 of this thesis), supports the possibility that gravitomagnetic tidal coupling might be responsible for the tiny remaining star-crushing effect.

1.2.2 Description of Slow-Motion, Isolated-Body Formalism

The slow-motion, isolated-body formalism assumes that there is some self-gravitating body (e.g., a neutron star or black hole) that interacts with an external tidal field (e.g., that of a binary companion). The body must be isolated in the sense that both the radius of curvature $\mathcal{R}$ of the external universe in the body's vicinity and the lengthscale $\mathcal{L}$ on which the universe's curvature changes are large compared to the body's size R: $R/\mathcal{R} \ll 1$ and $R/\mathcal{L} \ll 1$. This implies that the external tidal field (embodied in the external Riemann curvature tensor) must be weak and nearly uniform in the vicinty of the body. Consequently, the application of this formalism to binary systems (with one body producing the external tidal field felt by the other) is limited to the regime in which the bodies are fairly widely separated compared to their size. It should be noted, however, that this formalism can be applied even to strongly gravitating bodies, as long as the source of the external tidal field is far enough away to allow around each body a "buffer zone," also known as the body's local asymptotic rest frame, where gravity is weak (for more details, see the beginning of Sec. 4.4).

An additional assumption in the "slow-motion, isolated-body formalism" is the "slow-motion" requirement, meaning that the shortest timescale τ for changes of the body's multipole moments and/or changes of the universe's tidal gravitational field is long compared to the body's size R/c:

$R/c\tau \ll 1$, where c is the speed of light. This assumption allows us to neglect changes in the mass-energy M due to gravitational radiation or other higher-order effects.

As a result of these assumptions, the slow-motion, isolated-body formalism is essentially a perturbative expansion in powers of the small parameters $R/c\tau$, $R/\mathcal{R}$, and $R/\mathcal{L}$. The expansion terms of interest are the total mass-energy M and quadrupole moment $\mathcal{I}_{jk}$ of the isolated body, plus the external tidal field $\mathcal{E}_{jk} = R_{j0k0}$, where $R_{\alpha\beta\gamma\delta}$ is the Riemann tensor of the external universe. (In some cases [38, 39, 57], other moments of the body and other components of the external Riemann tensor will be of interest as well.)

Two examples of isolated, slow-motion bodies are (i) a neutron star or black hole in a compact binary system that spirals inward due to emission of gravitational waves; and (ii) some of the Galilean satellites (particularly Io and Europa) that travel around Jupiter in elliptic orbits and get heated by Jupiter's tidal gravitational field [58–62].

1.2.3 Mass-Energy Ambiguity and Tidal-Work Uniqueness

It was shown by Thorne and Hartle [37] that the total mass-energy of an isolated body is ambiguous by an amount of order

$$\delta M \sim \mathcal{I}_{jk}\mathcal{E}_{jk} ,$$

where $\mathcal{I}_{jk}$ is the body's mass quadrupole moment and $\mathcal{E}_{jk} = R_{j0k0}$ is the external tidal field. Physically, this ambiguity arises from the standard method for measuring the mass-energy of a gravitating body, which is to apply the general relativistic version of Kepler's law to a test particle in orbit around the body. If the body is non-spherical and is located in an external tidal field, a $\mathcal{I}_{jk}\mathcal{E}_{jk}$ cross-term will appear in the analysis of the relativistic Kepler problem. This term is monopolar and has dimensions of mass, so that the Kepler's law calculation gives a total mass-energy term of the form $M + \mathcal{O}(\mathcal{I}_{jk}\mathcal{E}_{jk})$, where the $\mathcal{O}(\mathcal{I}_{jk}\mathcal{E}_{jk})$ term has an ambiguous numerical coefficient.

The rate at which work is done by the external field on the body can be calculated as

$$\frac{dW}{dt} = -\frac{1}{2}\mathcal{E}_{jk}\frac{d\mathcal{I}_{jk}}{dt} .$$

This expression was derived by Zhang [38] using the Landau-Lifshitz pseudotensor, which represents one of an infinite number of methods of localizing the gravitational-field energy. Given the mass-energy ambiguity $\delta M \sim \mathcal{I}_{jk}\mathcal{E}_{jk}$, there was some question about whether the work done was also ambiguous by a similar amount.

In Thorne's work [40] on tidally induced volume changes and associated mass-energy changes, he argued (but did not prove) that the rate of work done is unambiguous at $\mathcal{O}(\mathcal{I}_{jk}\mathcal{E}_{jk})$ and that the ambiguity δM in the body's mass resides entirely in an ambiguity of how the interaction energy

between the body and the field is localized. In Chapter 4, I verify this via detailed calculations in Newtonian theory using all possible localizations of the gravitational energy. In each case, the work is unambiguously given by the above expression, but the interaction energy is $E_{\rm int} = \beta \mathcal{E}_{jk}\mathcal{I}_{jk}$, where β depends on the localization used.

A general relativistic analysis in Chapter 4 produces the same result. Using the Landau-Lifshitz pseudotensor but performing gauge transformations (infinitesimal coordinate transformations) on the spacetime metric, I demonstrate that the result for the rate of work done is the same as the Newtonian case $\frac{dW}{dt} = -\frac{1}{2}\mathcal{E}_{jk}\frac{d\mathcal{I}_{jk}}{dt}$, whereas the interaction energy term depends on the choice of gauge. It should be noted that the general relativistic gauge transformations represent a freedom that has no Newtonian analog; the general relativistic analog of the choice of a particular Newtonian gravitational-energy localization is the choice of a particular general relativistic pseudotensor. Favata [42] has verified that the results are unchanged with pseudotensors other than Landau-Lifshitz. In addition, Booth and Creighton [63] arrived at the same conclusion through an independent approach using quasilocal energy techniques.

This result that the tidal work is a well-defined and precise quantity should not be surprising, given that its physical effects have been observed on some of Jupiter's moons. In particular, tidal heating is responsible for volcanic activity on Io [58, 64–67] and for the presence of a subsurface liquid water ocean on Europa [59–62]. This Newtonian regime demonstration does not automatically guarantee the well-defined nature of tidal heating in highly relativistic neutron stars, but my analysis (together with the work of Favata, Booth, and Creighton) does guarantee it for neutron stars—and also for black holes.

1.3 Bibliography

[1] See http://www.ligo.caltech.edu/.

[2] M. Ando et al., Phys. Rev. Lett. **86**, 3950 (2001).

[3] See http://tamago.mtk.nao.ac.jp/.

[4] See http://www.geo600.uni-hannover.de/.

[5] A. Buonanno, private communication.

[6] K. Kuroda et al., *Large-scale Cryogenic Gravitational-wave Telescope*, Int. J. Mod. Phys. D **8**, 577 (1999); available at http://www.icrr.u-tokyo.ac.jp/gr/LCGT.pdf .

[7] Although there as yet are no detailed papers on EURO (or LIGO-III), they are much discussed within the gravitational-wave community and at conferences on long-range plans

for gravitational-wave detection; see, for example, the presentation by A. Rüdiger at http://www.ligo.caltech/~veronica/Aspen2001/ .

[8] A. Buonanno and Y. Chen, Class. Quantum Grav. **18**, L95 (2001).

[9] A. Buonanno and Y. Chen, Phys. Rev. D **64**, 042006 (2001).

[10] C. M. Caves, Phys. Rev. Lett. **45**, 75 (1980).

[11] W. G. Unruh, in *Quantum Optics, Experimental Gravitation, and Measurement Theory*, eds. P. Meystre and M. O. Scully (Plenum, 1982), p. 647.

[12] M. T. Jaekel and S. Reynaud, Europhys. Lett. **13**, 301 (1990).

[13] C. M. Caves, Phys. Rev. D **23**, 1693 (1981).

[14] S. P. Vyatchanin and A. B. Matsko, JETP **77**, 218 (1993).

[15] S. P. Vyatchanin and E. A. Zubova, Phys. Lett. A **201**, 269 (1995).

[16] S. P. Vyatchanin and A. B. Matsko, JETP **82**, 1007 (1996).

[17] S. P. Vyatchanin and A. B. Matsko, JETP **83**, 690 (1996).

[18] S. P. Vyatchanin, Phys. Lett. A **239**, 201 (1998).

[19] H. J. Kimble, Yu. Levin, A. B. Matsko, K. S. Thorne, and S. P. Vyatchanin, Phys. Rev. D **65**, 022002 (2001).

[20] V. B. Braginsky and F. Ya. Khalily, Phys. Lett. A **218**, 167 (1996).

[21] V. B. Braginsky, M. L. Gorodetsky, and F. Ya. Khalili, Phys. Lett. A **232**, 340 (1997).

[22] V. B. Braginsky, M. L. Gorodetsky, and F. Ya. Khalili, Phys. Lett. A **246**, 485 (1998).

[23] F. Ya. Khalili, gr-qc/0203002.

[24] A. Buonanno and Y. Chen, Phys. Rev. D 65, 042001 (2002); gr-qc/0107021.

[25] A. Buonanno and Y. Chen, to appear in Class. Quantum Grav.; gr-qc/0201063.

[26] V. B. Braginsky and F. Ya. Khalili, Phys. Lett. A **257**, 241 (1999).

[27] F. Ya. Khalili, gr-qc/0107084.

[28] V. B. Braginsky, M. L. Gorodetsky, and S. P. Vyatchanin, Phys. Lett. A **264**, 1 (1999).

[29] Y. T. Liu and K. S. Thorne, Phys. Rev. D **62**, 122002 (2000).

[30] C. M. Caves, K. S. Thorne, R. W. P. Drever, V. D. Sandberg, and M. Zimmermann, Rev. Mod. Phys. **52**, 341 (1980).

[31] C. M. Caves, in *Quantum Optics, Experimental Gravitation, and Measurement Theory*, eds. P. Meystre and M. O. Scully (Plenum, 1982), p. 567.

[32] V. B. Braginsky and F. Ya. Khalili, Phys. Lett. A **147**, 251 (1990).

[33] V. B. Braginsky, M. L. Gorodetsky, F. Ya. Khalili, and K. S. Thorne, Phys. Rev. D **61**, 044002 (2000).

[34] V. B. Braginsky, M. L. Gorodetsky, F. Ya. Khalili and K. S. Thorne, "Energetic Quantum Limit in Large-Scale Interferometers," in *Gravitational Waves*, Proceedings of the Third Edoardo Amaldi Conference, AIP Conference Proceedings Vol. 523, ed. Sydney Meshkov (American Institute of Physics, 2000) pp. 180–192; gr-qc/9907057.

[35] C. W. Misner, K. S. Thorne and J. A. Wheeler, *Gravitation*, (W. H. Freeman, San Francisco, 1973).

[36] K. S. Thorne, Rev. Mod. Phys. **52**, 299 (1980).

[37] K. S. Thorne and J. B. Hartle, Phys. Rev. D, **31**, 1815 (1985).

[38] X.-H. Zhang, Phys. Rev. D, **31**, 3130 (1985).

[39] X.-H. Zhang, Phys. Rev. D, **34**, 991 (1986).

[40] K. S. Thorne, Phys. Rev. D, **58**, 124031 (1998).

[41] E. E. Flanagan, Phys. Rev. D, **58**, 124030 (1998).

[42] M. Favata, Phys. Rev. D **63**, 064013 (2001).

[43] J. R. Wilson and G. J. Mathews, Phys. Rev. Lett. **75**, 4161 (1995).

[44] J. R. Wilson, G. J. Mathews and P. Maronetti, Phys. Rev. D **54**, 1317 (1996).

[45] G. J. Mathews, P. Maronetti, and J. R. Wilson, Phys. Rev. D **58**, 043003 (1998).

[46] D. Lai, Phys. Rev. Lett. **76**, 4878 (1996).

[47] A. G. Wiseman, Phys. Rev. Lett. **79**, 1189 (1997).

[48] P. R. Brady and S. A. Hughes, Phys. Rev. Lett. **79**, 1186 (1997).

[49] S. L. Shapiro, Phys. Rev. D **57**, 908 (1998).

[50] T. W. Baumgarte, G. B. Cook, M. A. Scheel, S. L. Shapiro, and S. A. Teukolsky, Phys. Rev. D **57**, 6181 (1998).

[51] T. W. Baumgarte, G. B. Cook, M. A. Scheel, S. L. Shapiro, and S. A. Teukolsky, Phys. Rev. D **57**, 7299 (1998).

[52] M. Shibata, T. W. Baumgarte, and S. L. Shapiro, Phys. Rev. D **58**, 023002 (1998).

[53] M. D. Duez, E. T. Engelhard, J. M. Fregeau, K. M. Huffenberger, and S. L. Shapiro, Phys. Rev. D **60**, 104024 (1999).

[54] E. E. Flanagan, Phys. Rev. Lett. **82**, 1354 (1999).

[55] P. Maronetti, G. J. Mathews, and J. R. Wilson, Phys. Rev. D **60**, 087301 (1999).

[56] G. J. Mathews and J. R. Wilson, Phys. Rev. D **61**, 127304 (2000).

[57] M. Favata and K. S. Thorne, in preparation. Their results were presented at the April 2002 meeting of the Americal Physical Society; their abstract is available at http://www.aps.org/meet/APR02/baps/abs/S4720010.html .

[58] S. J. Peale, P. Cassen, and R. T. Reynolds, Science **203**, 894 (1979).

[59] P. Cassen, R. T. Reynolds, and S. J. Peale, Geophys. Res. Lett. **6**, 731 (1979).

[60] P. Cassen, R. T. Reynolds, and S. J. Peale, Geophys. Res. Lett. **7**, 987 (1980).

[61] S. J. Peale, Annu. Rev. Astron. Astrophys. **37**, 37 (1999).

[62] A. P. Showman and R. Malhotra, Science **286**, 77 (1999).

[63] I. Booth and J. Creighton, Phys. Rev. D **62**, 067503 (2000).

[64] M. N. Ross and G. Schubert, Icarus **64**, 391 (1985).

[65] G. W. Ojakangas and D. J. Stevenson, Icarus **66**, 341 (1986).

[66] B. A. Smith *et al.*, Science **204**, 951 (1979).

[67] L. A. Morabito *et al.*, Science **204**, 972 (1979).

Chapter 2

Analysis of a Quantum Nondemolition Speed-Meter Interferometer

Published as P. Purdue, *Physical Review D* **66**, 022001 (2002).

2.1 Summary

In the quest to develop viable designs for third-generation optical interferometric gravitational-wave detectors (e.g., LIGO-III and EURO), one strategy is to monitor the relative momentum or speed of the test-mass mirrors, rather than monitoring their relative position. This paper describes and analyzes the most straightforward design for a *speed meter interferometer* that accomplishes this—a design (due to Braginsky, Gorodetsky, Khalili, and Thorne) that is analogous to a microwave-cavity speed meter conceived by Braginsky and Khalili. A mathematical mapping between the microwave speed meter and the optical interferometric speed meter is developed and is used to show (in accord with the speed being a Quantum Nondemolition [QND] observable) that *in principle* the interferometric speed meter can beat the gravitational-wave standard quantum limit (SQL) by an arbitrarily large amount, over an arbitrarily wide range of frequencies, and can do so without the use of squeezed vacuum or any auxiliary filter cavities at the interferometer's input or output. However, *in practice*, to reach or beat the SQL, this specific speed meter requires exorbitantly high input light power. The physical reason for this is explored, along with other issues such as constraints on performance due to optical dissipation. This analysis forms a foundation for ongoing attempts to develop a more practical variant of an interferometric speed meter and to combine the speed meter concept with other ideas to yield a promising LIGO-III/EURO interferometer design that entails low laser power.

2.2 Introduction

The first generation of kilometer-scale interferometric gravitational-wave detectors (LIGO-I [1, 2], VIRGO [3], and GEO600 [4]) will begin operation in 2002, at sensitivities where it is plausible but not highly probable that gravitational waves can be detected. Vigorous research and development is now underway for second-generation detectors (LIGO-II [5] and its European and Japanese partners [6, 7]) that are planned to begin operation in $\sim$ 2008 at a sensitivity where a rich variety of gravitational-wave sources should lie. This second-generation sensitivity will be near or modestly better than the *standard quantum limit* (SQL), a limit that constrains interferometers [8] such as LIGO-I which have conventional optical topology, but does not constrain more sophisticated "quantum nondemolition" (QND) interferometers [9, 10].

Conceptual-design research and development is now underway, at a modest level, for third-generation gravitational-wave interferometers that (it is hoped) will beat the SQL by a factor of $\sim$5 or more over a frequency band somewhat greater than the typical frequency of operation. This third-generation R&D has entailed, thus far, conceiving and exploring theoretically a number of ideas that might prove useful in a final design. Examples include (i) injecting squeezed vacuum into an interferometer's dark port [9–11], (ii) performing homodyne detection on the output light with frequency-dependent homodyne angle (achieved using large Fabry-Perot filter cavities) [12–17], (iii) using light pressure to transfer the gravity-wave signal onto a small test mass that moves relative to local inertial frames and then reading out that motion using local QND techniques (the *Optical Bar*) [18, 19], (iv) a variant of this involving *Symphotonic States* [20], (v) producing *Optical-Spring* behavior by means of a signal-recycling mirror [21], and (vi) other more general means of changing the dynamics of the test-mass mirrors [22, 23].

The purpose of this paper is to carry out a first detailed analysis of another idea that may prove helpful in third-generation interferometers: operating each interferometer as a *speed meter*, so instead of monitoring the relative position of its test-mass mirrors, it measures their relative speed (or, more precisely, a combination of their speed and higher-order time derivatives of position).

The motivation for measuring speed rather than position, stated in somewhat heuristic terms, is as follows: If a single measurement of the relative position of the test masses is made, then according to the uncertainty principle, there will be a corresponding random "kick" to the relative momentum. This kick will affect the future positions of the test masses. If another position measurement is made at a later time, its accuracy will be limited because of the earlier momentum kick. The best one can do is balance the uncertainties of the two measurements; this optimal uncertainty corresponds to the SQL.

If, on the other hand, the velocity (which is directly proportional to the momentum) is measured directly, this velocity measurement will randomly kick the relative position. That position kick is

irrelevant *if* the velocity is being measured without collecting position information, as in a speed meter. Another way to say this is to note that the velocity (or momentum) is a constant of the free motion of the test mass. Consequently, the velocity commutes with itself at different times and is therefore a quantum nondemolition (QND) observable [24, 25]. The result is that speed meters are not constrained by the SQL.

The original idea for a speed meter that measures the velocity of a single test mass was conceived, in a primitive form, by Braginsky and Khalili [26]. Braginsky, Gorodetsky, Khalili, and Thorne [27] (henceforth called BGKT) devised a refined and marginally practical form based on two coupled microwave cavities. In their appendix, BGKT also sketched a design for an optical-interferometer speed meter gravity-wave detector that, they speculated, will be able to beat the gravity-wave SQL in essentially the same manner as the microwave speed meter beats the free-mass SQL.

This paper presents a detailed analysis of the BGKT optical-interferometer speed meter, with the objective of determining whether it actually does measure relative velocity without collecting position information and whether it actually can beat the SQL. As we shall see, the answers are both "yes." Moreover, it will be shown that there is a mathematical mapping between the analysis of the microwave-cavity speed meter, which measures the velocity of a single mass, and that of the optical-interferometer speed meter, which measures the relative speeds of widely separated test masses. Another objective of this paper is to explore the features of this optical-interferometer speed meter that will be important in attempts to design practical third-generation interferometers.

The basic design of the speed meter to be analyzed here is shown in Figure 2.1. It consists of two nearly identical optical cavities of length $L = 4\text{km}$, which are weakly coupled by a mirror of power transmissivity T_s. In the absence of a driving force, laser light can "slosh" back and forth between these two cavities with frequency

$$\Omega = c\sqrt{T_s}/L\,, \tag{2.1}$$

where c is the speed of light. The addition of a driving laser [denoted $I(\zeta)$ in Fig. 2.1] into one cavity will cause the other cavity to become excited. It is from this excited cavity that we will extract our signal [denoted $K(\eta)$] at a rate

$$\delta = cT_o/4L\,, \tag{2.2}$$

where T_o is the transmissivity of the extraction mirror.

Since we cannot make T_o infinitely small (or equivalently, the extraction time infinite), a small amount of residual light will build up in the unexcited cavity. To counteract this, we also input a small amount of laser light [denoted $L(\zeta)$] through the output port in order to cancel out any such residual light. This is desirable because one cavity must be empty to achieve pure speed meter behavior[1].

[1] In general, one could allow some amount of light to build up in the "empty" cavity, and thereby (as we shall see

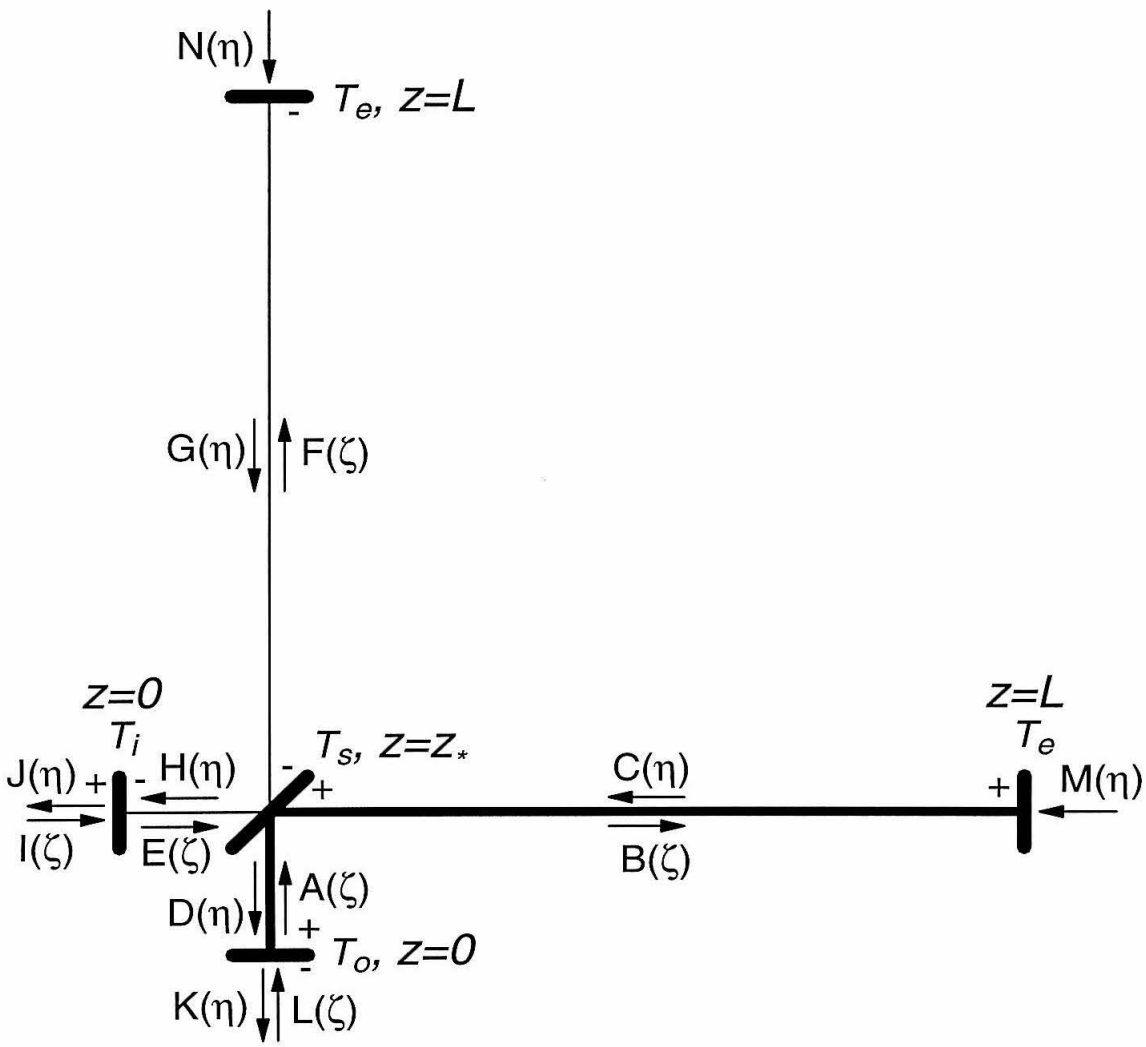

Figure 2.1: Design for a QND speed-meter interferometer. The main laser input port is the lower left mirror [denoted by $I(\zeta)$, where $\zeta = t - z/c$]. The signal is extracted at the bottom mirror [denoted $K(\eta)$, where $\eta = t + z/c$]. The "+" and "−" signs near the mirrors indicate the sign of the reflectivities in the junction conditions for each location.

To understand how this system produces a velocity signal, consider the effect of moving the end mirror in the excited cavity [the cavity labeled $C(\eta)$ and $B(\zeta)$ in Fig. 2.1]. That mirror motion will put a phase shift on the light in that cavity. If the input laser is driving the cavity's cosine quadrature, then the phase shift caused by the mirror motion will act as a driving force for the sine quadrature. This light will then slosh into the empty cavity and back. When it returns, it will be 180° out of phase compared to its initial phase shift. The resulting cancellation will cause the net signal in the sine quadrature of the excited cavity to be proportional to the difference in test-mass position between the start and finish of the sloshing cycle. In other words, the net signal is proportional to the velocity of the test mass, assuming that the frequencies ω of the test mass' motion are $\omega \ll \Omega$.

As it turns out, however, the optimal regime of operation for the speed meter is $\omega \sim \Omega$. Consequently, the output signal contains a sum over odd time derivatives of position [see Eq. (2.31) and the discussion following it]. Therefore, the speed meter monitors not just the relative speed of the test masses, but a mixture of all odd time derivatives of the position.

As we will show, this speed-meter design, *in principle*, is capable of beating the SQL by an arbitrary amount and over a wide range of frequencies. However, *in practice*, optical losses will limit the amount by which the SQL can be beaten, and to beat the SQL at all requires an uncomfortably high circulating power. (This is actually a common feature of designs that beat the SQL [28].) More seriously, this design requires an impossibly high input power because the photons are not getting "sucked" into the interferometer efficiently, as they are in conventional designs; this will be discussed in more detail in Sec. 2.4.3.

In view of this impracticality, one might wonder why a detailed analysis of this speed meter should be published. The answer is that this analysis teaches us a variety of things about optical-interferometer speed meters—things that are likely to be of value in the search for practical QND interferometers and in their optimization. Indeed, the author and Yanbei Chen are now exploring more sophisticated and promising speed-meter designs that rely, for motivation and insights, on the things learned in the analysis presented here.

This paper is organized as follows: The mathematical description of the interferometer is given in Sec. 2.3. Sec. 2.4.1 gives the analysis of the lossless limit and the mapping to the microwave-resonator speed meter, Sec. 2.4.2 presents the numerical analysis, and as mentioned above, Sec. 2.4.3 describes various problems or issues with the speed meter. In Sec. 2.5, we give the results and a description of the speed meter's performance if losses are included. The discussion there will address the role of optical dissipation in limiting the amount by which the SQL can be beaten. Finally, Sec. 2.6 summarizes the results of this analysis and its relevance for future research.

in Sec. 2.4.3), make it easier to inject light into the interferometer. Then, the ratio of the levels of excitation of the two cavities would become a tool for optimizing the design, balancing reduced input power against performance.

2.3 Mathematical Description of the Interferometer

The design of the speed meter is shown in Figure 2.1. In this section, we will set up the equations describing the interferometer with lossy mirrors. The method of analysis is based on the formalism developed by Caves and Schumaker [29, 30] and used by Kimble, Matsko, Thorne, and Vyatchanin (KLMTV) [17] to examine more conventional interferometer designs.

We express the electric field propagating in each direction down each segment of the interferometer in the form

$$E_{\text{field}}(\zeta) = \sqrt{\frac{4\pi\hbar\omega_0}{\mathcal{S}c}}A(\zeta)\,, \tag{2.3}$$

where $A(\zeta)$ is the amplitude, $\zeta = t - z/c$ (see Fig. 2.1), ω_0 is the carrier frequency, $\hbar$ is the reduced Planck's constant, and $\mathcal{S}$ is the effective cross-sectional area of the light beam; see Eq. (8) of KLMTV. We decompose the amplitude into cosine and sine quadratures,

$$A(\zeta) = \mathcal{A}_1(\zeta)\cos\omega_0\zeta + \mathcal{A}_2(\zeta)\sin\omega_0\zeta\,. \tag{2.4}$$

Note that the subscript 1 always refers to the cosine quadrature, and 2 to sine. Also note that we have designated $z = 0$ at both the input and output mirrors, $z = z_*$ at the sloshing mirror, and $z = L$ at the end mirrors; see Fig. 2.1. We choose the cavity lengths L to be exact half multiples of the carrier wavelength so $e^{i2\omega_0 L/c} = 1$.

As mentioned above, the power transmissivity for the sloshing mirror is T_{s} and for the output mirror is T_{o}. In addition, T_{i} will denote the transmissivity for the laser-input mirror and T_{e} for the end mirrors; again, see Fig. 2.1. Each of these has a complementary reflectivity such that each mirror satisfies the equation $T + R = 1$. If we now let $\zeta = t - z/c$, $\eta = t + z/c$, and $j = 1, 2$, then the junction conditions at the mirrors are given by:

$$\mathcal{A}_j(\zeta) = \sqrt{T_{\text{o}}}\mathcal{L}_j(\zeta) + \sqrt{R_{\text{o}}}\mathcal{D}_j(\eta)\,, \tag{2.5a}$$

$$\mathcal{B}_j(\zeta) = \sqrt{T_{\text{s}}}\mathcal{E}_j(\zeta) + \sqrt{R_{\text{s}}}\mathcal{A}_j(\zeta)\,, \tag{2.5b}$$

$$\mathcal{C}_j(\eta) = \sqrt{T_{\text{e}}}\mathcal{M}_j(\eta) + \sqrt{R_{\text{e}}}\mathcal{B}_j(\zeta)\,, \tag{2.5c}$$

$$\mathcal{D}_j(\eta) = \sqrt{T_{\text{s}}}\mathcal{G}_j(\eta) + \sqrt{R_{\text{s}}}\mathcal{C}_j(\eta)\,, \tag{2.5d}$$

$$\mathcal{E}_j(\zeta) = \sqrt{T_{\text{i}}}\mathcal{I}_j(\zeta) - \sqrt{R_{\text{i}}}\mathcal{H}_j(\eta)\,, \tag{2.5e}$$

$$\mathcal{F}_j(\zeta) = \sqrt{T_{\text{s}}}\mathcal{A}_j(\zeta) - \sqrt{R_{\text{s}}}\mathcal{E}_j(\zeta)\,, \tag{2.5f}$$

$$\mathcal{G}_j(\eta) = \sqrt{T_{\text{e}}}\mathcal{N}_j(\eta) - \sqrt{R_{\text{e}}}\mathcal{F}_j(\zeta)\,, \tag{2.5g}$$

$$\mathcal{H}_j(\eta) = \sqrt{T_s}\mathcal{C}_j(\eta) - \sqrt{R_s}\mathcal{G}_j(\eta)\,, \tag{2.5h}$$

$$\mathcal{J}_j(\eta) = \sqrt{T_i}\mathcal{H}_j(\eta) + \sqrt{R_i}\mathcal{I}_j(\zeta)\,, \tag{2.5i}$$

$$\mathcal{K}_j(\eta) = \sqrt{T_o}\mathcal{D}_j(\eta) - \sqrt{R_o}\mathcal{L}_j(\zeta)\,. \tag{2.5j}$$

2.3.1 Carrier Light

If we first consider only the carrier in a steady state, we can assume that all the mirrors are stationary and that all of the $\mathcal{A}_j(\zeta) = A_j$, $\mathcal{B}_j(\zeta) = B_j$, etc., are constant. (We denote the carrier amplitudes by capital Latin letters with a subscript indicating the quadrature.) Then we solve Eqs. (2.5) simultaneously. We ignore vacuum fluctuation noise since it is unimportant for the carrier light. In addition, we only drive the cosine quadrature, so that

$$L_2 = I_2 = 0\,. \tag{2.6}$$

Thus, all of the sine quadrature terms will be zero. As mentioned above, we want to have as little light as possible in the unexcited cavity, so we apply the condition

$$F_1 = G_1 = 0\,. \tag{2.7}$$

That means the input fed into the output port should be

$$L_1 = \frac{I_1}{4}\sqrt{\frac{T_o T_i}{T_s}}\,. \tag{2.8}$$

Then, the solution for the carrier is

$$A_1 = B_1 = C_1 = D_1 = \frac{I_1}{2}\sqrt{\frac{T_i}{T_s}}\,, \tag{2.9a}$$

$$E_1 = H_1 = \frac{I_1}{2}\sqrt{T_i}\,. \tag{2.9b}$$

In deriving Eqs. (2.9), we have assumed the following inequalities among the various mirror transmissivities:

$$T_o \gg T_s \gg T_i \gg T_e\,. \tag{2.10}$$

The motivations for these assumptions are that (i) they lead to speed-meter behavior; (ii) as with any interferometer, the best performance is achieved by making the end-mirror transmissivities T_e as small as possible; (iii) good performance requires a light extraction rate comparable to the sloshing rate, $\delta \sim \Omega$ [cf. the first paragraph of Sec. 2.4.2], which with Eqs. (2.1) and (2.2) implies $T_o \sim \sqrt{T_s}$ so $T_o \gg T_s$; and (iv) if the input transmissivity is larger than or of the same order as the sloshing frequency, too much light will be lost during the sloshing cycle, resulting in incomplete cancellation

of the position information and degraded performance (hence, we assume $T_{\rm i} \ll T_{\rm s}$).

2.3.2 Sideband Light

Sidebands are put onto the carrier by the mirror motions and by vacuum fluctuations, as we shall see below. We express the quadrature amplitudes for the carrier plus the side bands in the form

$$\mathcal{A}_j(\zeta) = A_j + \int_0^\infty [\tilde{a}_j(\omega)e^{-i\omega\zeta} + \tilde{a}_j^\dagger(\omega)e^{i\omega\zeta}]\frac{d\omega}{2\pi}\,, \tag{2.11}$$

where $\tilde{a}_j(\omega)$ is the field amplitude for the sideband at frequency ω in the j quadrature; cf. Eqs. (6)–(8) of KLMTV, where commutation relations and the connection to creation and annihilation operators are discussed. Then most of the junction conditions can easily be broken down into separate expressions for the constant and sideband terms; for example,

$$A_j = \sqrt{T_{\rm o}}L_j + \sqrt{R_{\rm o}}D_j\,, \tag{2.12a}$$

$$\tilde{a}_j = \sqrt{T_{\rm o}}\tilde{\ell}_j + \sqrt{R_{\rm o}}\tilde{d}_j\,. \tag{2.12b}$$

The exceptions are Eqs. (2.5c) and (2.5g) because the two end mirrors will change the phase of the sidebands on each bounce. Equation (2.5g) becomes

$$G_j = -\sqrt{R_{\rm e}}F_j + \sqrt{T_{\rm e}}N_j\,, \tag{2.13a}$$

$$\tilde{g}_j = -\sqrt{R_{\rm e}}\tilde{f}_j e^{i\beta} + \sqrt{T_{\rm e}}\tilde{n}_j\,, \tag{2.13b}$$

where $\beta = 2\omega L/c$ is the phase shift for the sidebands. At this point, we also want to allow mirror motion in order to detect gravitational waves, so we assume that the end mirror of the excited cavity is free to move. As a result, the junction condition there, expressed by Eq. (2.5c), is the most complicated. It becomes

$$C_j = \sqrt{R_{\rm e}}B_j + \sqrt{T_{\rm e}}M_j\,, \tag{2.14a}$$

$$\tilde{c}_1 = \sqrt{R_{\rm e}}\tilde{b}_1 e^{i\beta} - 2\sqrt{R_{\rm e}}B_2\omega_0\tilde{x}/c + \sqrt{T_{\rm e}}\tilde{m}_1\,, \tag{2.14b}$$

$$\tilde{c}_2 = \sqrt{R_{\rm e}}\tilde{b}_2 e^{i\beta} + 2\sqrt{R_{\rm e}}B_1\omega_0\tilde{x}/c + \sqrt{T_{\rm e}}\tilde{m}_2\,, \tag{2.14c}$$

where $\tilde{x}$ is the Fourier transform of the mirror's displacement. (We are ignoring the motion of the end mirror of the empty cavity since that will not have a significant effect.)

All of the junction condition equations [Eqs. (2.5) expressed in the form of Eqs. (2.12), (2.13), and (2.14)] can be solved simultaneously to get expressions for the carrier and sidebands in each segment of the interferometer. This yields an output $[K(\eta)]$ containing an $\omega\tilde{x}$ term, which is the

Fourier transform of the end-mirror velocity (relative to the input mirror), aside from a factor of i. Since there is no factor $\tilde{x}$ without a multiplying factor ω in the output, our interferometer is indeed a speed meter, as claimed by BGKT.

One more complication to be addressed is the issue of the back action force on the mirror produced by the fluctuating radiation pressure of the laser beam. The back action is included in $\tilde{x}$ along with the gravitational wave information, as follows.

From KLMTV, Eq. (B18), the back-action force is

$$F_{BA} = \frac{2\delta W_{\rm circ}}{c}\,, \tag{2.15}$$

where $\delta W_{\rm circ}$ is the fluctuation in the circulating laser power. To determine this quantity, consider the expression for the circulating power [text above Eq. (B16) in KLMTV]:

$$W_{\rm circ} = \frac{\overline{E_{\rm int}^2}}{4\pi}\mathcal{S}c\,, \tag{2.16}$$

where $\mathcal{S}$ is the effective cross-sectional area of the beam, and $\overline{E_{\rm int}^2}$ is the time-averaged square of the internal electric field. In our case,

$$E_{\rm int} = \sqrt{\frac{4\pi\hbar\omega_0}{\mathcal{S}c}}\left\{\cos(\omega_0 t)\left[B_1 + \int_0^\infty (\tilde{b}_1 e^{-i\omega t} + \tilde{b}_1^\dagger e^{i\omega t})\frac{d\omega}{2\pi}\right] + \sin(\omega_0 t)\left[\int_0^\infty (\tilde{b}_2 e^{-i\omega t} + \tilde{b}_2^\dagger e^{i\omega t})\frac{d\omega}{2\pi}\right]\right\}. \tag{2.17}$$

See Eqs. (2.3), (2.4), and (2.11) with $\mathcal{A}$ replaced by $\mathcal{B}$. Note that the constant term B_2 vanishes since we are driving only the cosine quadrature. Substituting Eq. (2.17) into Eq. (2.16) will give a steady circulating power

$$W_{\rm circ} = \frac{1}{2}\hbar\omega_0 B_1^2 = \hbar\omega_0 I_1^2 \frac{T_{\rm i}}{8T_{\rm s}} \tag{2.18}$$

and a fluctuating piece

$$\delta W_{\rm circ}(t) = \hbar\omega_0 B_1 \int_0^\infty \tilde{b}_1(\omega) e^{-i\omega t}\frac{d\omega}{2\pi} + {\rm HC}\,, \tag{2.19}$$

where HC denotes the Hermitian conjugate of the previous term.

Now that we have an expression for $\delta W_{\rm circ}$, we return to the expression for the back-action force (2.15). That force, together with the gravitational waves, produces a relative acceleration of the cavity's two mirrors (each with mass m) given by

$$\frac{d^2x(t)}{dt^2} = \frac{1}{2}L\frac{d^2h(t)}{dt^2} + \frac{4\delta W_{\rm circ}(t)}{mc}\,, \tag{2.20}$$

where $h(t)$ is the gravitational-wave field [cf. Eq. (B19) in KLMTV]. Substituting Eq. (2.19) into

the above equation and taking the Fourier transform gives

$$\tilde{x} = \frac{1}{2}L\tilde{h} - \frac{4\hbar\omega_0 B_1 \tilde{b}_1}{mc\omega^2} \,. \tag{2.21}$$

Here B_1 is given by Eq. (2.9a), and $\tilde{b}_1$, as obtained by solving the junction conditions and simplifying with the conditions on the transmissivities (2.10), is given by

$$\tilde{b}_1 = \frac{-i\omega c\sqrt{T_o}\tilde{\ell}_1}{2L\mathcal{L}(\omega)} \,, \tag{2.22}$$

where

$$\mathcal{L}(\omega) = \Omega^2 - \omega^2 - i\omega\delta \,. \tag{2.23}$$

(Recall that $\Omega = c\sqrt{T_s}/L$ is the sloshing frequency, $\delta = cT_o/4L$ the extraction rate.)

2.4 Speed Meter in the Lossless Limit

2.4.1 Mathematical Analysis

For simplicity, in this section we will set $T_e = 0$ (end mirrors perfectly reflecting), since it is unimportant if T_e is much smaller than the other transmissivities. We will also neglect the noise coming in the main laser port ($\tilde{i}_{1,2}$). This noise will become dominant at sufficiently low frequencies (below $\sim$10 Hz for the interesting parameter regime), but those frequencies are not very relevant to LIGO since that is the regime in which seismic noise begins to dominate.

As a result of these assumptions, the only noise that remains is that which comes in through the output port ($\tilde{\ell}_{1,2}$). An interferometer in which this is the case and in which light absorption and scattering are unimportant ($R + T = 1$ for all mirrors, as we have assumed) is said to be "lossless." In Sec. 2.5, we shall relax these assumptions; i.e., we shall consider lossy interferometers. As before, we assume $T_o \gg T_s \gg T_i$. The interferometer output, as derived by the analysis of the previous section, is then

$$\tilde{k}_1 = -\frac{\mathcal{L}^*(\omega)}{\mathcal{L}(\omega)}\tilde{\ell}_1 \,, \tag{2.24a}$$

$$\tilde{k}_2 = \frac{-i\omega\omega_0 I_1\sqrt{T_o T_i}}{2L\sqrt{T_s}\mathcal{L}(\omega)}\tilde{x} - \frac{\mathcal{L}^*(\omega)}{\mathcal{L}(\omega)}\tilde{\ell}_2 \,, \tag{2.24b}$$

where the asterisk (in $\mathcal{L}^*(\omega)$) denotes the complex conjugate. Note that $\tilde{x}$ is given by Eq. (2.21) combined with Eqs. (2.9a) and (2.22), or equivalently, by

$$\tilde{x} = \frac{1}{2}L\tilde{h} + \tilde{x}_{\rm BA} \,, \tag{2.25}$$

where

$$\tilde{x}_{\rm BA} = \frac{i\hbar\omega_0 I_1\sqrt{T_{\rm o}T_{\rm i}}\tilde{\ell}_1}{m\omega L\sqrt{T_{\rm s}}\mathcal{L}(\omega)} \tag{2.26}$$

is the back-action noise. It is possible to express Eqs. (2.24) in a more concise form, similar to Eqs. (16) in KLMTV:

$$\tilde{k}_1 = \tilde{\ell}_1 e^{2i\psi}\,, \tag{2.27a}$$

$$\tilde{k}_2 = (\tilde{\ell}_2 - \kappa\tilde{\ell}_1)e^{2i\psi} + \sqrt{\kappa}\frac{\tilde{h}}{h^{\rm conv}_{SQL}}e^{i\psi}\,, \tag{2.27b}$$

where

$$\tan\psi = -\frac{\Omega^2-\omega^2}{\omega\delta}\,, \tag{2.28}$$

$$\kappa = \frac{\hbar\omega_0^2 I_1^2 T_{\rm o}T_{\rm i}}{2mL^2T_{\rm s}|\mathcal{L}(\omega)|^2}\,, \tag{2.29}$$

and

$$h^{\rm conv}_{SQL} = \sqrt{\frac{8\hbar}{m\omega^2L^2}}\,. \tag{2.30}$$

If, as in KLMTV, we regard Eqs. (2.27) as input-output relations for the interferometer, then κ is a dimensionless coupling constant, which couples the gravity wave signal $\tilde{h}$ into the output $\tilde{k}_2$, $\tilde{h}^{\rm conv}_{SQL}$ is the standard quantum limit for a conventional interferometer such as LIGO-I, and ψ is a phase put onto the signal and noise by the interferometer. Although there is much similarity between the above equations (2.27) and those of KLMTV, there is not a direct mapping because KLMTV analyzes a position meter, not a speed meter.

As a tool in optimizing the interferometer's performance, we perform homodyne detection on the outputs $\tilde{k}_1$ and $\tilde{k}_2$, using a constant (frequency-independent) homodyne angle Φ. In other words, we read out $\tilde{k}_\Phi = \tilde{k}_1\cos\Phi + \tilde{k}_2\sin\Phi$. If we insert Eqs. (2.24) and do some algebra, we get

$$\tilde{k}_\Phi = \frac{-i\omega\omega_0 I_1\sqrt{T_{\rm o}T_{\rm i}}}{2L\sqrt{T_{\rm s}}\mathcal{L}(\omega)}\sin\Phi[\tilde{x}(\omega)+\tilde{x}_m(\omega)]\,. \tag{2.31}$$

Here $\tilde{x}_m$, the measurement noise (actually shot noise), is given by

$$\tilde{x}_m = \frac{2L\sqrt{T_{\rm s}}\mathcal{L}^*(\omega)}{i\omega\omega_0 I_1\sqrt{T_{\rm o}T_{\rm i}}}[\tilde{\ell}_2 + \tilde{\ell}_1\cot\Phi]\,, \tag{2.32}$$

and $\tilde{x}$ is given by Eqs. (2.25) and (2.26). Notice that the first term in Eq. (2.31) contains $\tilde{x}$ only in the form $\omega\tilde{x}$; this is the velocity signal [actually, the sum of the velocity and higher odd time derivatives of position because of the $\mathcal{L}(\omega)$ in the denominator]. These equations, (2.31) and (2.32), are equivalent to Eqs. (29) and (30) of BGKT. In fact, the analysis of the single-test-mass, microwave

Table 2.1: Mapping of the parameters in the BGKT microwave-resonator speed meter paper to those in this paper.

Parameter	BGKT	Purdue
signal frequency	ω	ω
carrier frequency	ω_e	ω_0
optimal frequency	ω_0	$\omega_{\rm opt}$
mass of test body	m	m
characteristic length	d	L
sloshing frequency	Ω	$\Omega = c\sqrt{T_{\rm s}}/L$
test-mass displacement	$\tilde{x}(\omega)$	$\tilde{x}(\omega)$
signal extraction rate[a]	$\delta_e = 1/2\tau_e^*$	$\delta = cT_{\rm o}/4L$
impedance of resonators[b]	ρ	$\rho_{\rm o} = 2L/c\sqrt{T_{\rm o}}$ $\rho_{\rm i} = 2L/c\sqrt{T_{\rm i}}$
driving amplitude[c]	U_0	αI_1
amplitude in excited cavity[c]	$-q_0 = U_0/\Omega\rho$	$\alpha B_1 = \alpha I_1/\Omega\rho_{\rm i}$
noise into output port[c,d]	$\{U_{es},\ U_{ec}\}$	$-\alpha\{\tilde{\ell}_1,\ \tilde{\ell}_2\}$
sideband components[c,e]	$\{a_1, b_1, a_2, b_2\}$	$\alpha\{\tilde{b}_1, \tilde{b}_2, \tilde{f}_1, \tilde{f}_2\}$
output amplitude[c]	$\tilde{U}(\omega)$	$\alpha\tilde{k}_\Phi(\omega)$

[a] τ_e^* is the relaxation time of the excited resonator due to energy flowing out.

[b] In BGKT, both resonators have the same characteristic impedance, but in this interferometer, they are different. Consequently, caution must be used when transforming between the two models.

[c] There is a proportionality constant $\alpha = \sqrt{2\hbar\sqrt{T_{\rm o}}}$ which must be included to get the correct dimensionality when transforming BGKT's equations into Purdue's notation. For example, $U_0 \longleftrightarrow \alpha I_1$.

[d] Notice that the quadratures are reversed. This is due to a difference in the way the models were defined.

[e] Notice that in Purdue's notation the letter indicates the cavity and the numerical subscript indicates the quadrature, whereas in BGKT, the letter indicates the quadrature and the number indicates the resonator.

speed meter in that reference (Sec. 2.4.3) can be translated more or less directly into the analysis of our speed-meter interferometer with a suitable change of notation (see Table 2.1)[2].

We assume that ordinary vacuum enters the output port of the interferometer; i.e., $\tilde{\ell}_1$ and $\tilde{\ell}_2$ are quadrature amplitudes for ordinary vacuum. This means [Eq. (26) of KLMTV] that their spectral densities are unity and their cross-correlations are zero. By noting that the homodyne output (2.31) is proportional to

$$\frac{2}{L}(\tilde{x} + \tilde{x}_m) = \tilde{h} + \frac{2}{L}(\tilde{x}_{BA} + \tilde{x}_m) \tag{2.33}$$

and examining the dependence of $\tilde{x}_{BA}$ and $\tilde{x}_m$ on the input vacuum $\tilde{\ell}_1$ and $\tilde{\ell}_2$, we deduce the (single-sided) spectral density of the gravitational wave output noise $\tilde{h}$:

$$S_{h_n} = (h_{SQL}^{\rm speed})^2\xi^2\,, \tag{2.34}$$

where

$$h_{SQL}^{\rm speed} = \sqrt{\frac{16\hbar}{m\omega^2L^2}}\,, \tag{2.35}$$

[2] There is a slight difference in the way the models in this paper and in BGKT were defined. One result is that there are some sign and quadrature differences between them. For details, see Table I, particularly the "amplitude in excited cavity" and "noise into output port."

is the standard quantum limit (SQL) for our speed-meter interferometer,

$$\xi^2 = \frac{|\mathcal{L}(\omega)|^2}{2\Lambda^4 \sin^2\Phi} - \cot\Phi + \frac{\Lambda^4}{2|\mathcal{L}(\omega)|^2}\,, \tag{2.36}$$

is the fractional amount by which the SQL is beaten (in units of squared amplitude), and

$$\Lambda^4 = \frac{\hbar T_o T_i (\omega_0 I_1)^2}{2L^2 m T_s}\,. \tag{2.37}$$

Note that the quantity ξ^2 is the same (modulo a minus sign in the definition of Φ) as the quantity $\xi^2_{\rm WB}$ in BGKT [Eq. (40)].

We comment, in passing, on the SQLs that appear in the various papers: BGKT use double-sided spectral densities and measure the velocity of a single test body with mass μ. The corresponding standard quantum limit for position is

$$(S^{\text{one body}}_{x,SQL})_{\text{double-sided}} = \frac{\hbar}{\mu\omega^2} \tag{2.38}$$

[their Eq. (5) divided by $\mu^2\omega^4$ to convert from force to position and with μ denoted by m]. KLMTV and the present paper used single-sided spectral densities, i.e., we fold negative frequencies into positive, so our one-body SQL is

$$(S^{\text{one body}}_{x,SQL})_{\text{single-sided}} = \frac{2\hbar}{\mu\omega^2}\,. \tag{2.39}$$

For our speed meter, the quantity measured is the relative velocity of two mirrors, $x = x_1 - x_2$, for which the gravitational-wave signal is $\frac{1}{2}\tilde{h}L$ and the reduced mass is $\mu = m/2$, so our gravity-wave SQL spectral density is

$$(S^{\text{speed meter}}_{h,SQL})_{\text{single-sided}} \equiv (h^{\text{speed}}_{SQL})^2 = \left(\frac{2}{L}\right)^2 \frac{2\hbar}{(m/2)\omega^2} = \frac{16\hbar}{m\omega^2 L^2}\,. \tag{2.40}$$

For a conventional interferometer, as analyzed by KLMTV, the quantity measured is the relative position of four mirrors, $x = (x_1 - x_2) - (x_3 - x_4)$, for which the gravitational-wave signal is $2 \cdot \frac{1}{2}\tilde{h}L = \tilde{h}L$ and the reduced mass is $\mu = m/4$, so the gravity-wave SQL spectral density is

$$(S^{\text{conv}}_{h,SQL})_{\text{single-sided}} \equiv (h^{\text{conv}}_{SQL})^2 = \left(\frac{1}{L}\right)^2 \frac{2\hbar}{(m/4)\omega^2} = \frac{8\hbar}{m\omega^2 L^2}\,, \tag{2.41}$$

half as large as for our speed meter. If we were to build a speed meter consisting of two excited cavities (one in each arm) and two unexcited cavities (as in Fig. 4 of BGKT), then our speed meter SQL would be reduced by a factor of 2, to the same value as for a conventional interferometer.

Continuing with our analysis, we can express $|\mathcal{L}(\omega)|^2$ [Eq. (2.23)] as

$$|\mathcal{L}(\omega)|^2 = (\omega^2 - \omega_{\rm opt}^2)^2 + \delta^2(\omega_{\rm opt}^2 + \delta^2/4)\,, \tag{2.42}$$

where

$$\omega_{\rm opt} = \sqrt{\Omega^2 - \delta^2/2}\,, \tag{2.43}$$

as we shall see, is the interferometer's optimal frequency. These two expressions are identical to Eqs. (37) and (38) of BGKT. We shall optimize the homodyne angle Φ to minimize the noise at some specific frequency, ω_F. The result is

$$\cot\Phi = \frac{\Lambda^4}{|\mathcal{L}(\omega_F)|^2}\,. \tag{2.44}$$

Then, Eqs. (42)–(48) of BGKT apply exactly to the analysis here: $\xi^2(\omega)$ for this homodyne phase Φ (2.44) is

$$\xi^2(\omega) = \frac{|\mathcal{L}(\omega)|^2}{2\Lambda^4} + \frac{\Lambda^4(\omega^2 - \omega_F^2)^2(\omega^2 + \omega_F^2 - 2\omega_{\rm opt}^2)^2}{2|\mathcal{L}(\omega)|^2|\mathcal{L}(\omega_F)|^4}\,, \tag{2.45}$$

and its minimum is

$$\xi^2_{\rm min} = \xi^2(\omega_F) = \frac{(\omega_F^2 - \omega_{\rm opt}^2)^2 + \delta^2(\omega_{\rm opt}^2 + \delta^2/4)}{2\Lambda^4}\,. \tag{2.46}$$

The noise can be further minimized by setting the speed meter's optimal frequency to $\omega_{\rm opt} = \omega_F$ to get

$$\xi^2(\omega) = \frac{|\mathcal{L}(\omega)|^2}{2\Lambda^4} + \frac{\Lambda^4(\omega^2 - \omega_{\rm opt}^2)^4}{2|\mathcal{L}(\omega)|^2\delta^4(\omega_{\rm opt}^2 + \delta^2/4)^2}\,, \tag{2.47}$$

with

$$\xi^2_{\rm min} = \frac{\delta^2(\omega_{\rm opt}^2 + \delta^2/4)}{2\Lambda^4} = \frac{W_{\rm circ}^{\rm SQL}}{W_{\rm circ}}\,. \tag{2.48}$$

Here $W_{\rm circ}$ is the power circulating in the excited arm [3] [Eq. (2.18)] and

$$\begin{aligned} W_{\rm circ}^{\rm SQL} &= \frac{mL^2\delta^2(\omega_{\rm opt}^2 + \delta^2/4)}{8\omega_0 T_{\rm o}} \\ &= (840{\rm kW})\left(\frac{m}{40{\rm kg}}\right)\left(\frac{L}{4{\rm km}}\right)^2\left(\frac{0.07}{T_{\rm o}}\right)\left(\frac{\omega_{\rm opt}}{2\pi\times 100{\rm Hz}}\right)^4\left(\frac{1.78\times 10^{15}{\rm Hz}}{\omega_0}\right) \end{aligned} \tag{2.49}$$

is the circulating power required to reach the standard quantum limit at the optimal frequency $\omega_{\rm opt}$ (we have assumed $\delta = 2\omega_{\rm opt}$ to get the second line of the above equation; see Sec. 2.4.2). By pumping with a power $W_{\rm circ} > W_{\rm circ}^{\rm SQL}$, the speed meter can beat the SQL in the vicinity of the optimal frequency $\omega_{\rm opt}$ by the amount $\xi^2_{\rm min} = W_{\rm circ}^{\rm SQL}/W_{\rm circ}$.

If [following BGKT Eqs. (47) and (48)] we define the frequency band $\omega_1 < \omega < \omega_2$ of high

[3] Note that that Eq. (2.48) uses the power circulating in the excited cavity, $W_{\rm circ}$, whereas BGKT's quantity W in their Eq. (45) is equivalent to the power *transmitted* through the interferometer's input mirror. This quantity W is also the amount of power extracted with the signal at the output port ($W_{\rm exit}$ in Sec. 2.4.2 and 2.4.3).

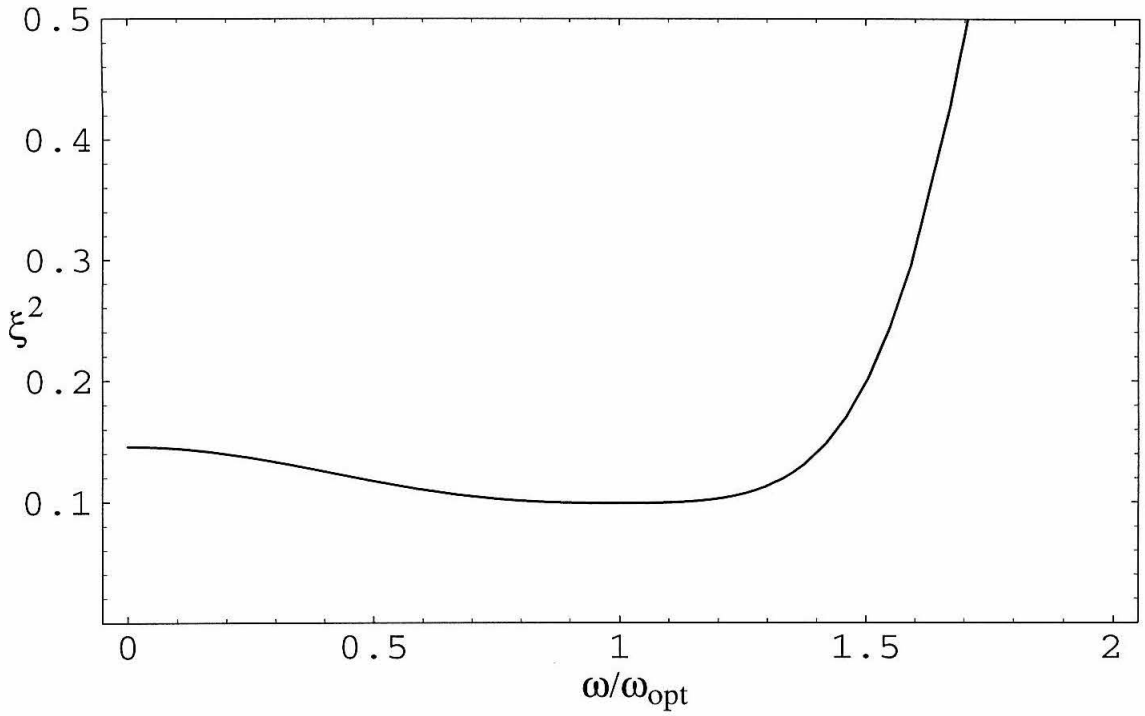

Figure 2.2: Plot of the squared amount by which the speed meter beats the standard quantum limit ($h^{\rm speed}_{SQL}$), as a function of frequency (normalized to the optimal frequency, $\omega_{\rm opt}$). For the parameter values $\xi^2_{\rm min} = 0.1$, $\delta = 2\omega_{\rm opt}$, and $\Lambda^4 = 40\omega^4_{\rm opt}$, this is identical to the speed meter curve in Fig. 3 of BGKT.

sensitivity to be those frequencies for which

$$\xi(\omega) \le \sqrt{2}\xi(\omega_{\rm opt})\,, \tag{2.50}$$

then Eqs. (2.47) and (2.48) imply that

$$\begin{aligned}\omega^2_{1,2} &= \omega^2_{\rm opt} \mp \frac{\delta^2(\omega^2_{\rm opt}+\delta^2/4)}{\sqrt[4]{\delta^4(\omega^2_{\rm opt}+\delta^2/4)^2+\Lambda^8}} \\ &= \omega^2_{\rm opt} \mp \frac{2\Lambda^2\xi^2_{\rm min}}{\sqrt[4]{4\xi^4_{\rm min}+1}}\,.\end{aligned} \tag{2.51}$$

Equations (2.51), (2.47), and (2.48) imply that the lossless speed meter can beat the force-measurement SQL by a large amount $\xi_{\rm min} \ll 1$ over a wide frequency band, $\omega_1 \ll \omega_2 \sim \sqrt{2}\omega_{\rm opt}$ by setting

$$\frac{\Lambda}{\omega_{\rm opt}} \sim \frac{\delta^2}{2\omega^2_{\rm opt}} \gtrsim 2\,. \tag{2.52}$$

A plot of ξ^2, optimized in this manner but for rather modest parameter values, is shown in Fig. 2.2.

Table 2.2: Interferometer parameters and their fiducial values.

Parameter	Symbol	Fiducial Value
carrier frequency	ω_0	$1.78 \times 10^{15}\text{s}^{-1}$
mirror mass	m	40 kg
arm length	L	4 km
sloshing mirror transmissivity	T_s	0.0002
input mirror transmissivity	T_i	2×10^{-5}
output mirror transmissivity	T_o	0.07
end mirror transmissivity	T_e	2×10^{-6}
SQL circulating power	W_circ^{SQL}	840 kW

2.4.2 Numerical Analysis

To get an idea of the magnitudes of the quantities involved in this interferometer, we can start by combining the wide-bandwith requirement (2.52) with the definitions $\delta = cT_\text{o}/4L$, $\Omega = c\sqrt{T_\text{s}}/L$, and $\omega_\text{opt}^2 = \Omega^2 - \delta^2/2$. From these, we find that the wide-bandwidth requirement $\delta^2 \gtrsim 4\omega_\text{opt}^2$ becomes $T_\text{o}^2 \gtrsim (64/3)T_\text{s}$. If, as in BGKT, we take $\delta = 2\omega_\text{opt} = 2\omega_F$ but set $\omega_\text{opt} = 2\pi \times 100\text{Hz}$ as in KLMTV, then that gives $T_\text{o} = 0.07$ and $T_\text{s} = 0.0002$. Notice this particular value of T_s does not satisfy the condition $\omega_\text{opt} \ll \Omega$, which was necessary to get a signal that is *only* proportional to the velocity of the test masses' motion. Instead, we have $\omega_\text{opt} \sim \Omega$, which implies that the signal consists of a linear combination of odd time derivatives of position, with substantial contributions coming from derivatives higher than the speed [see Eq. (2.31)].

If, in addition to $\delta = 2\omega_\text{opt} = 2\omega_F = 4\pi \times 100$ Hz, we choose $\xi_\text{min}^2 = 0.1$ (as in BGKT), then we find $W_\text{circ}^{SQL} \simeq 840\text{kW}$ from Eq. (2.49) and a circulating power of $W_\text{circ} \simeq 8.4\text{MW}$. The input-port transmissivity is not explicitly defined by the above requirements, but it is required, in our analysis, to be much smaller than $T_\text{s} = 0.0002$ or $T_\text{o} = 0.07$, i.e., $T_\text{i} \lesssim 2 \times 10^{-5}$. This then dictates an outrageously high input power of $\gtrsim$300 MW to get the needed circulating power. The power that exits through the signal port, along with the signal, is $W_\text{exit} = T_\text{o} W_\text{circ} \sim 0.5\text{MW}$. The resulting noise curve is shown in Fig. 2.3; the parameter values used are given in Table 2.2.

Recall that this analysis is for only one speed meter, which is equivalent to a single arm of the conventional LIGO design. If we were to add another speed meter (another pair of cavities) with the position of the excited and unexcited cavities reversed, interfering the output beams would increase the sensitivity by a factor of two, in much the same way as having two arms increases the sensitivity in the conventional LIGO design. In addition, doing this would reduce the interferometer's sensitivity to laser frequency fluctuations in the same way as having two arms in conventional LIGO designs.

2.4.3 Discussion of Lossless Speed Meter

In this section, we will look at variety of issues that should be understood and addressed in the process of developing a different, more practical, speed-meter design. One problem is the large

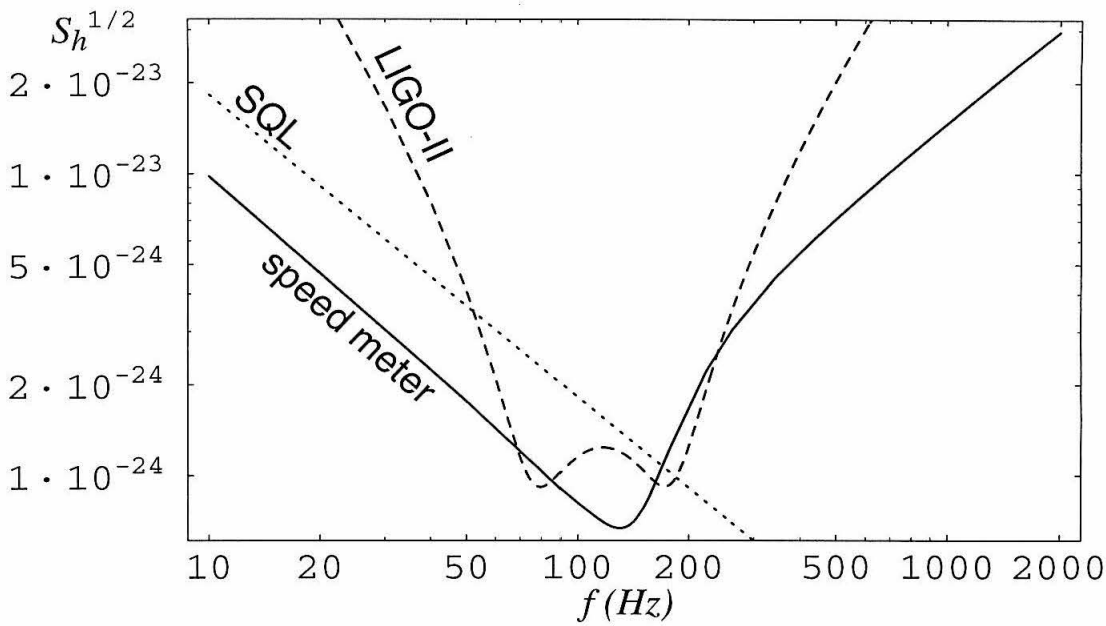

Figure 2.3: Lossless noise curve for a speed meter optimized at a frequency of 100 Hz. The transmissivities and power are given in Table 2.2. The dashed line represents the theoretical LIGO-II noise curve in which a signal-recycling mirror and optical noise correlations have been used to beat the SQL (and thermal noise has been made negligible), as described by Buonanno and Chen [33, 34]. The dotted line represents the SQL; we use $h^{\rm conv}_{SQL}$ because we are comparing to a position meter.

circulating power (~8.4 MW) required to achieve wide-band sensitivity a factor ~ 10 in noise power below the standard quantum limit. A second problem is how to get that light into the interferometer, as the present design requires an input power that is outrageously high. This is, at least partly, the result of the high reflectivity of the input mirror, which causes most of the input light to be reflected back towards the laser.

A third problem is the amount of power flowing through the interferometer: With a circulating power of ~8.4 MW, the power extracted with the signal is $W_{\rm exit} = T_{\rm o} W_{\rm circ} \sim 0.5$ MW. This same amount of power must be fed into the excited cavity to maintain a steady state. To reduce this power throughput, we could decrease $T_{\rm o}$ substantially; however, doing this will cause the wide-bandwidth requirement (2.52) to be violated, and consequently, the behavior of the speed meter will become more narrow-band. In fact, the effect of changing $T_{\rm o}$ is strong enough that if it is decreased by one order of magnitude, the speed meter will no longer beat the SQL except for a very narrow range of frequencies. This clearly is not a viable solution.

Another approach, in which this large throughput power might conceivably be tolerated, is to recycle it back into the interferometer. To do that, we must strip the signal off by using a beamsplitter to interfere the outputs from two speed-meter interferometers as in Fig. 4 of BGKT.

Using this "double" speed meter could also help increase the sensitivity, as described at the end of the previous section.

Turning to the issue of the high circulating power, it should first be noted that the circulating power required to reach the SQL, $W_{\rm circ}^{SQL} \sim 840$ kW is comparable to that for conventional interferometers [Eq. (132) of KLMTV gives $W_{\rm circ}^{SQL} \sim 840$ kW with $m = 40$ kg, instead of 30 kg]. A double speed meter, as described above, would have twice the sensitivity as a single speed meter at the same power. As mentioned in Sec. 2.2, the high powers needed to reach or beat the SQL are a common feature of many QND designs [28], for example the variational-output interferometer discussed in KLMTV.

A likely method of reducing the needed circulating power, without losing the wide-band performance of the speed meter, is to inject squeezed vacuum into the output port, as was originally proposed by Caves [11] for conventional interferometers and by KMLTV for their QND squeezed-input and squeezed-variational interferometers. In these cases, for realistic amounts of squeezing, the circulating power can be reduced by as much as an order of magnitude [11, 17]. Detailed analyses applying squeezed-vacuum techniques to speed meters have not yet been carried out, but if the effect is similar, it would have the beneficial side effect of reducing the needed input power by the same amount, which might be useful in a redesigned speed meter.

As for the outrageously high input power, the fact that so much of the light impinging on the input-port mirror is reflected back to the laser suggests an obvious solution would be adding a power-recycling mirror and/or increasing the transmissivity $T_{\rm i}$ of the input mirror. However, neither of these approaches addresses the fundamental problem: there is an empty cavity between the driving laser and the excited cavity. In a conventional LIGO-type interferometer, the laser drives a strongly excited Fabry-Perot cavity directly. In that case, Bose statistics dictate that photons will be "sucked" into the cavities, producing a strong amplification. Hence, there will be significantly more power stored in the arms of the interferometer than the driving laser is producing. Without losses,

$$\frac{\text{circulating power}}{\text{input power}} \sim \frac{8}{T_{\rm PR} T_{\rm IM}} \sim 10^5 \,, \tag{2.53}$$

where $T_{\rm PR} \sim 0.06$ is the transmissivity of the power-recycling mirror and $T_{\rm IM} \sim 0.005$ is that of the internal mirrors [31]. However, in this speed meter design, there is an empty cavity instead of a low power laser feeding into the highly excited cavity so Bose statistics do not help us. The result is the need for a driving laser that produces far more power than is stored in the arms of the speed meter:

$$\frac{\text{circulating power}}{\text{input power}} \sim \frac{T_{\rm i}}{4T_{\rm s}} \sim 10^{-3} \,. \tag{2.54}$$

One way to address this problem would be to allow a small amount of light to build up in the previously empty cavity. This would cause position information to contaminate the previously pure

speed meter behavior. However, this solution is not ideal because, as the amount of light in the "empty" cavity increases, the sensitivity degrades faster than the required input power decreases. To consider this more closely, we first need to remove the restriction (2.8) on the light L_1 fed into the output port, which forces the unexcited cavity [denoted by $F(\zeta)$ and $G(\eta)$ in Fig. 1] to be truly empty. Instead, we let L_1 be determined by the amount of power we want to have in the unexcited cavity. Secondly, since the unexcited cavity is no longer empty, we need to include the movement of the end mirror in that cavity, which we previously neglected. This requires revising Eqs. (2.13) to include $\tilde{x}$ terms (with back action) as in Eqs. (2.14). To calculate how much the needed input power decreases as a function of the ratio of the powers of the two cavities, we can solve for the carrier, as in Eqs. (2.9), and do some algebra to express the input amplitude I_1 as a function of the excited-cavity amplitude B_1 and the ratio of the amplitudes of the powers of the two cavities (F_1/B_1). After converting from amplitudes to powers, the relationship between the input powers is

$$\frac{W_{\rm input}(R)}{W_{\rm input}(R=0)} = \left[1 - \frac{T_{\rm i}\sqrt{R}}{2\sqrt{T_{\rm s}}}\right], \tag{2.55}$$

where R is the ratio of the powers in the two cavities. Since we require $T_{\rm i} \ll T_{\rm s} \ll 1$ and $R \ll 1$ to get speed-meter behavior, $W_{\rm input}$ cannot be reduced much at all.

Also of concern here is how much position information will be included in the output. To calculate the strength of the position signal, relative to the strength of the velocity signal, we can solve the revised equations (as described in the previous paragraph) for the sideband-light output. Then taking the ratio of the coefficients of the position $\tilde{x}$ term and the velocity $\tilde{x}$ term, we find

$$\left|\frac{\text{position}}{\text{velocity}}\right| \sim \frac{c\sqrt{T_{\rm s}}}{\omega L}\sqrt{R} = \frac{\Omega}{\omega}\sqrt{R} \sim \sqrt{R}\,. \tag{2.56}$$

Since the spectral density involves the square of the amplitudes used to calculate the above expression (2.56), S_{h_n} and ξ^2 will scale with R. This indicates that even a modest amount of power in the "empty" cavity will introduce a significant amount of position information into the output signal. The effect of this, for a few values of R, can be seen in Fig. 2.4.

In fact, it appears that this problem of outrageously high input power is the fatal flaw of this particular speed-meter design. Yanbei Chen [32] has conceived a class of alternative speed-meter designs that may solve this problem. Chen and the author are carrying out an analysis and optimization of them; we shall report the details in a future paper.

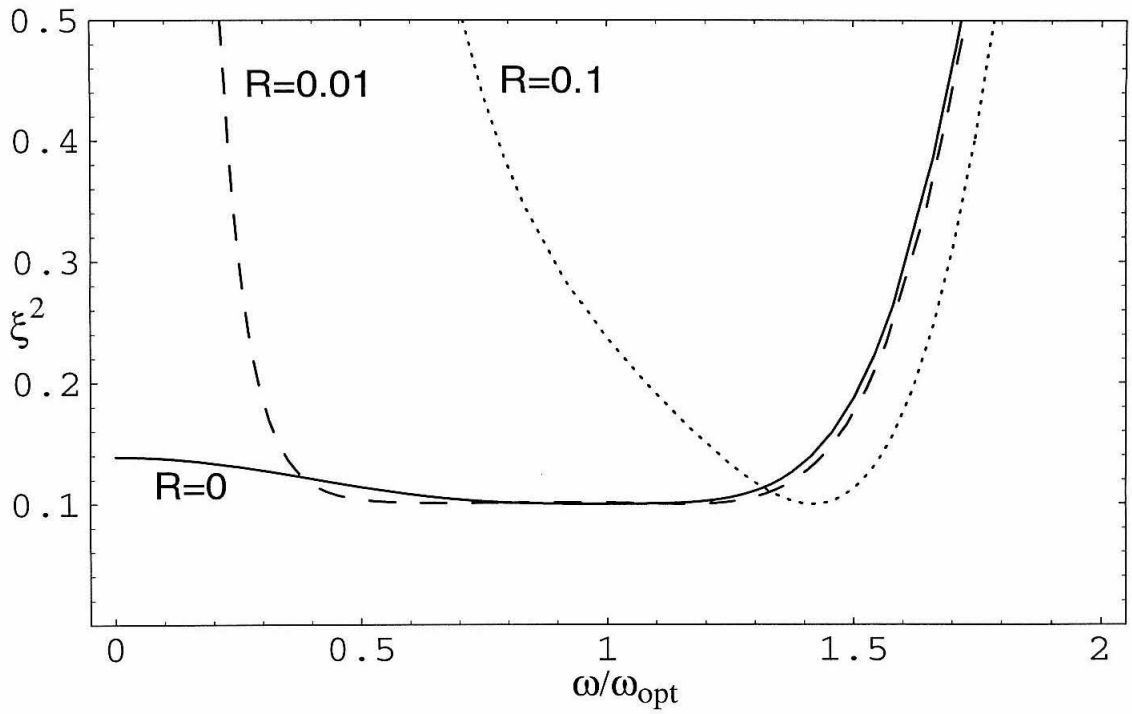

Figure 2.4: Plot of ξ^2 for the lossless speed meter optimized at a frequency of 100 Hz, with varying amounts of power in the "empty" cavity. The $R = 0$ curve is the same as that in Fig. 2.2. Transmissivities are $T_s = 0.0002$, $T_o = 0.07$, $T_i = 2 \times 10^{-5}$, $T_e = 0$, and the circulating power is 8.4 MW.

2.5 Sensitivity of Speed Meter with Losses

In order to understand the issue of optical losses and dissipation in this type of interferometer, we shall return to the full equations presented in Sec. 2.3. In that case, the output of the system is:

$$\tilde{k}_1 = -\frac{\mathcal{L}^*(\omega)}{\mathcal{L}(\omega)}\tilde{\ell}_1 + \frac{c^2\sqrt{T_s T_o T_i}}{2L^2\mathcal{L}(\omega)}\tilde{i}_1 - \frac{i\omega c\sqrt{T_o T_e}}{2L\mathcal{L}(\omega)}\tilde{m}_1 + \frac{c^2\sqrt{T_s T_o T_e}}{2L^2\mathcal{L}(\omega)}\tilde{n}_1\,, \tag{2.57a}$$

$$\tilde{k}_2 = \frac{-i\omega\omega_0 I_1\sqrt{T_o T_i}}{2L\sqrt{T_s}\mathcal{L}(\omega)}\tilde{x} - \frac{\mathcal{L}^*(\omega)}{\mathcal{L}(\omega)}\tilde{\ell}_2 + \frac{c^2\sqrt{T_s T_o T_i}}{2L^2\mathcal{L}(\omega)}\tilde{i}_2 - \frac{i\omega c\sqrt{T_o T_e}}{2L\mathcal{L}(\omega)}\tilde{m}_2 + \frac{c^2\sqrt{T_s T_o T_e}}{2L^2\mathcal{L}(\omega)}\tilde{n}_2\,, \tag{2.57b}$$

where

$$\tilde{x} = \frac{1}{2}L\tilde{h} + \frac{\hbar\omega_0 I_1}{m\omega^2 L^2\mathcal{L}(\omega)}\left[\frac{i\omega L\sqrt{T_o T_i}}{\sqrt{T_s}}\tilde{\ell}_1 - cT_i\tilde{i}_1 + \frac{i\omega L\sqrt{T_i T_e}}{\sqrt{T_s}}\tilde{m}_1 - c\sqrt{T_i T_e}\tilde{n}_1\right]. \tag{2.58}$$

As before, we can express these in a more concise way:

$$\tilde{k}_1 = \tilde{\ell}_1 e^{2i\psi} - (\tilde{i}_1\kappa_i + \tilde{n}_1\kappa_n)e^{i\theta} + \tilde{m}_1\kappa_m e^{i\psi}\,, \tag{2.59a}$$

$$\tilde{k}_2 = \Big(\tilde{\ell}_2 - \kappa\tilde{\ell}_1 - \kappa\frac{\sqrt{T_e}}{\sqrt{T_o}}\tilde{m}_1\Big)e^{2i\psi} - (\tilde{i}_2\kappa_i + \tilde{n}_2\kappa_n)e^{i\theta} + \Big(\frac{\sqrt{\kappa}}{h^{\rm conv}_{SQL}}\tilde{h} + \kappa_m\tilde{m}_2\Big)e^{i\psi} + \Big(\tilde{i}_1\sqrt{T_i} + \frac{\sqrt{T_e}}{\sqrt{T_o}}\tilde{n}_1\Big)\frac{\Omega}{\omega}\kappa e^{i\phi}\,, \tag{2.59b}$$

where, in addition to the definitions given by Eqs. (2.4.1),

$$\tan\theta = -\cot\psi\,, \tag{2.60}$$

and

$$\kappa_i = \sqrt{\frac{c^4 T_s T_o T_i}{4L^4|\mathcal{L}(\omega)|^2}}\,, \tag{2.61a}$$

$$\kappa_m = \sqrt{\frac{c^2 T_o T_e \omega^2}{4L^2|\mathcal{L}(\omega)|^2}}\,, \tag{2.61b}$$

$$\kappa_n = \sqrt{\frac{c^4 T_s T_o T_e}{4L^4|\mathcal{L}(\omega)|^2}}\,. \tag{2.61c}$$

Once again, we do homodyne detection and calculate the spectral density of the noise. (It should be noted that, in the lossy case, there are enough differences between the optical speed meter and the BGKT microwave speed meter to obscure the mapping. Consequently, we will not be able to present as close a comparison in this section as we did in the lossless case.) The fractional amount by which the SQL is beaten is

$$\xi^2 = \frac{|\mathcal{L}'(\omega)|^2}{2\Lambda^4\sin^2\Phi} - \cot\Phi + \frac{\Lambda^4}{2|\mathcal{L}(\omega)|^2}\,, \tag{2.62}$$

where

$$|\mathcal{L}'(\omega)|^2 = (\omega^2 - \omega'^2_{\rm opt})^2 + \delta\delta^*[\omega'^2_{\rm opt} + \frac{\delta\delta'}{4\delta^*}(\delta^* + \delta_e + \delta_i)]\,, \tag{2.63}$$

with

$$\delta_i = cT_i/L\,, \tag{2.64}$$

$$\delta_e = cT_e/L\,, \tag{2.65}$$

$$\delta' = \delta + \delta_e\,, \tag{2.66}$$

$$\delta^* = \delta + 2\delta_e + \delta_i\,, \tag{2.67}$$

and

$$\omega'_{\rm opt} = \sqrt{\Omega^2 - \delta\delta'/2}\,. \tag{2.68}$$

Optimizing the homodyne angle at frequency ω_F gives

$$\cot\Phi = \frac{\Lambda^4}{|\mathcal{L}'(\omega_F)|^2}\,. \tag{2.69}$$

The resulting ξ^2 is

$$\xi^2 = \frac{|\mathcal{L}'(\omega)|^2}{2\Lambda^4} - \frac{\Lambda^4}{|\mathcal{L}'(\omega_F)|^2} + \frac{\Lambda^4|\mathcal{L}'(\omega)|^2}{2|\mathcal{L}'(\omega_F)|^2} + \frac{\Lambda^4}{2|\mathcal{L}(\omega)|^2}\,. \tag{2.70}$$

Setting $\omega = \omega'_{\rm opt} = \omega_F$ gives

$$\begin{aligned}\xi^2(\omega'_{\rm opt}) &= \frac{\delta^2\delta'(\delta_e+\delta_i)/4 + \delta\delta^*(\omega'^2_{\rm opt} + \delta\delta'/4)}{2\Lambda^4} - \frac{\Lambda^4}{2[\delta^2\delta'(\delta_e+\delta_i)/4 + \delta\delta^*(\omega'^2_{\rm opt} + \delta\delta'/4)]} \\ &\quad + \frac{\Lambda^4}{2[(\omega'^2_{\rm opt} - \omega^2_{\rm opt})^2 + \delta^2(\omega^2_{\rm opt} + \delta^2/4)]}\,.\end{aligned} \tag{2.71}$$

Cf. Eq. (2.48). Note that, as in BGKT, the sensitivity in the lossy case does not continue to grow indefinitely with the growth of the parameter Λ.

Despite the presence of the additional terms included to account for losses, the speed meter curve is largely unchanged if we maintain our assumptions about the relative sizes of the transmissivities (2.10). In fact, the only losses that contribute significantly are those associated with $\tilde{i}_1$ (i.e., noise entering the bright port along with the laser light). This term causes the speed meter to become less sensitive at frequencies $\ll \omega_{\rm opt}$, as seen in Fig. 2.5. Since that is roughly the frequency at which seismic noise becomes dominant, the effect of more limited sensitivity in that range is not important.

As it turns out, the equations in this section are valid into the regime where $T_{\rm e} \simeq T_{\rm i} \simeq T_{\rm s}$. In that case, the $\tilde{n}_1$ term will be the same size as the $\tilde{i}_1$ term, and together, they become dominant at frequencies $\lesssim \omega_{\rm opt}$, while the rest of the loss terms continue to be insignificant for this parameter regime. Presumably, the sensitivity degradation by $\tilde{n}_1$ and $\tilde{i}_1$ is the result of vacuum fluctuations entering into the empty cavity and contaminating the "sloshing" light. This behavior is shown in Fig. 2.5. As can be seen from that plot, the interferometer loses wideband sensitivity when operating in this regime.

2.6 Conclusions

We have analyzed the speed-meter interferometer proposed by BGKT and have shown that it does, indeed, measure test-mass speed (and time derivatives of speed) rather than test-mass position. We have also shown that it is capable of beating the SQL over a broad range of frequencies. However, the very high circulating and input powers it requires render this design impractical for use in LIGO-III.

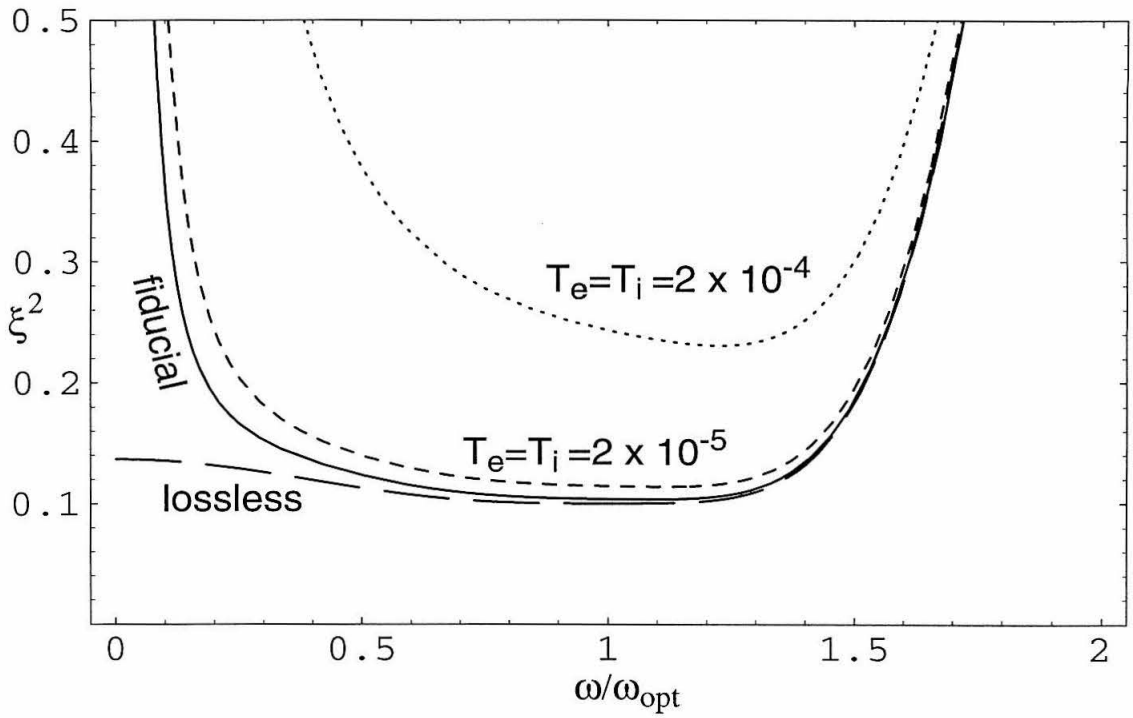

Figure 2.5: Plot of ξ^2 for the speed meter with losses. The solid curve uses the transmissivities given in Table 2.2. The lossless curve has $T_e = 0$, as in Fig. 2.2. The other two curves differ from the fiducial-value curve only by the specified transmissivities.

It is possible, however, that there are variations of this design that will be more feasible.

There are three separate but related problems related to the laser power involved in this speed meter. One is the amount of circulating power (~8.4 MW) required to beat the SQL substantially (by a factor 10 in noise power) over a wide range of frequencies. Another is the amount of power coming out of the interferometer with the signal (~0.5 MW). Both of these are serious problems, but there are conceivable solutions to them. The third and most severe problem is the fact that the excited cavity is being fed through an empty cavity. This dramatically increases the amount of input power needed to achieve a given circulating power, to the point where the input is significantly greater than the circulating power.

Motivated by what we have learned in this analysis, Yanbei Chen and the author are developing and exploring alternative designs for speed-meter interferometers that may solve the above problems and actually be practical.

2.7 Bibliography

[1] A. Abramovici et al., Science **256**, 325 (1992).

[2] B. C. Barish and R. Weiss, Physics Today **52**, 44 (1999).

[3] B. Caron et al., Class. Quantum Grav. **14**, 1461 (1997).

[4] H. Lück and the GEO600 Team. Class. Quantum Grav. **14**, 1471 (1997).

[5] E. Gustafson, D. Shoemaker, K. Strain, and R. Weiss, *LSC White Paper on Detector Research and Development*, LIGO document T990080-00-D (1999); available along with other relevant information at http://www.ligo.caltech.edu/~ligo2/ .

[6] Although there as yet are no detailed papers on EURO (or LIGO-III), they are much discussed within the gravitational-wave community and at conferences on long-range plans for gravitational-wave detection; see, for example, the presentation by A. Rüdiger at http://www.ligo.caltech/~veronica/Aspen2001/ .

[7] K. Kuroda et al., *Large-scale Cryogenic Gravitational-wave Telescope*, Int. J. Mod. Phys. D **8**, 577 (1999); available at http://www.icrr.u-tokyo.ac.jp/gr/LCGT.pdf .

[8] C. M. Caves, Phys. Rev. Lett. **45**, 75 (1980).

[9] W. G. Unruh, in *Quantum Optics, Experimental Gravitation, and Measurement Theory*, eds. P. Meystre and M. O. Scully (Plenum, 1982), p. 647.

[10] M. T. Jaekel and S. Reynaud, Europhys. Lett. **13**, 301 (1990).

[11] C. M. Caves, Phys. Rev. D **23**, 1693 (1981).

[12] S. P. Vyatchanin and A. B. Matsko, JETP **77**, 218 (1993).

[13] S. P. Vyatchanin and E. A. Zubova, Phys. Lett. A **201**, 269 (1995).

[14] S. P. Vyatchanin and A. B. Matsko, JETP **82**, 1007 (1996).

[15] S. P. Vyatchanin and A. B. Matsko, JETP **83**, 690 (1996).

[16] S. P. Vyatchanin, Phys. Lett. A **239**, 201 (1998).

[17] H. J. Kimble, Yu. Levin, A. B. Matsko, K. S. Thorne, and S. P. Vyatchanin, Phys. Rev. D **65**, 022002 (2001).

[18] V. B. Braginsky and F. Ya. Khalily, Phys. Lett. A **218**, 167 (1996).

[19] V. B. Braginsky, M. L. Gorodetsky, and F. Ya. Khalili, Phys. Lett. A **232**, 340 (1997).

[20] V. B. Braginsky, M. L. Gorodetsky, and F. Ya. Khalili, Phys. Lett. A **246**, 485 (1998).

[21] A. Buonanno and Y. Chen, Phys. Rev. D **65**, 042001 (2002).

[22] V. B. Braginsky and F. Ya. Khalili, Phys. Lett. A **257**, 241 (1999).

[23] F. Ya. Khalili, gr-qc/0107084.

[24] C. M. Caves, K. S. Thorne, R. W. P. Drever, V. D. Sandberg, and M. Zimmermann, Rev. Mod. Phys. **52**, 341 (1980).

[25] C. M. Caves, in *Quantum Optics, Experimental Gravitation, and Measurement Theory*, eds. P. Meystre and M. O. Scully (Plenum, 1982), p. 567.

[26] V. B. Braginsky and F. Ya. Khalili, Phys. Lett. A **147**, 251 (1990).

[27] V. B. Braginsky, M. L. Gorodetsky, F. Ya. Khalili, and K. S. Thorne, Phys. Rev. D **61**, 044002 (2000); gr-qc/9906108.

[28] V. B. Braginsky, M. L. Gorodetsky, F. Ya. Khalili and K. S. Thorne, "Energetic Quantum Limit in Large-Scale Interferometers," in *Gravitational Waves*, Proceedings of the Third Edoardo Amaldi Conference, AIP Conference Proceedings Vol. 523, ed. Sydney Meshkov (American Institute of Physics, 2000) pp. 180–192; gr-qc/9907057.

[29] C. M. Caves and B. L. Schumaker, Phys. Rev. A **31**, 3068 (1985).

[30] B. L. Schumaker and C. M. Caves, Phys. Rev. A **31**, 3093 (1985).

[31] P. Fritschel, ed., *Advanced LIGO Systems Design*, LIGO document T010075-00-D (2001); see also http://www.ligo.caltech.edu/~ligo2/ .

[32] Y. Chen (private communication).

[33] A. Buonanno and Y. Chen, Class. Quantum Grav. **18**, L95 (2001).

[34] A. Buonanno and Y. Chen, Phys. Rev. D **64**, 042006 (2001).

Chapter 3

Practical Speed-Meter Designs for QND Gravitational-Wave Interferometers

To be submitted to *Physical Review D*; written in collaboration with Yanbei Chen.

3.1 Summary

In the quest to develop viable designs for third-generation optical interferometric gravitational-wave detectors (e.g., LIGO-III and EURO), one strategy is to monitor the relative momentum or speed of the test-mass mirrors, rather than monitoring their relative position. The previous chapter analyzed a straightforward but impractical design for a *speed-meter interferometer* that accomplishes this. This chapter describes some practical variants of speed-meter interferometers. Like the original interferometric speed meter, these designs *in principle* can beat the gravitational-wave standard quantum limit (SQL) by an arbitrarily large amount, over an arbitrarily wide range of frequencies. These variants essentially consist of a Michelson interferometer plus an extra "sloshing" cavity that sends the signal back into the interferometer with opposite phase shift, thereby cancelling the position information and leaving a net phase shift proportional to the relative velocity. *In practice*, the sensitivity of these variants will be limited by the maximum light power $W_{\rm circ}$ circulating in the arm cavities that the mirrors can support and by the leakage of vacuum into the optical train at dissipation points. In the absence of dissipation and with squeezed vacuum (power squeeze factor $e^{-2R} \simeq 0.1$) inserted into the output port so as to keep the circulating power down, the SQL can be beat by $h/h_{\rm SQL} \sim \sqrt{W_{\rm circ}^{SQL} e^{-2R}/W_{\rm circ}}$ at all frequencies below some chosen $f_{\rm opt} \simeq 100$ Hz. Here $W_{\rm circ}^{SQL} \simeq 800{\rm kW}(f_{\rm opt}/100{\rm Hz})^3$ is the power required to reach the SQL in the absence of squeezing. [However, as the power increases in this expression, the speed meter becomes more narrow band; additional power and re-optimization of some parameters are required to maintain the wide band. See Sec. 3.4.2.] Estimates are given of the amount by which vacuum leakage at dissipation points will debilitate this sensitivity (see Fig. 3.12); these losses are 10% or less over most of the frequency range of interest ($f \gtrsim 10$ Hz). The sensitivity can be improved, particularly at high freqencies, by

using frequency-dependent homodyne detection, which unfortunately requires two 4-kilometer-long filter cavities (see Fig. 3.4).

3.2 Introduction

This paper is part of the effort to explore theoretically various ideas for a third-generation interferometric gravitational-wave detector. The goal of such detectors is to beat, by a factor of 5 or more, the *standard quantum limit* (SQL)—a limit that constrains interferometers [1] such as LIGO-I which have conventional optical topology [2, 3], but does not constrain more sophisticated "quantum nondemolition" (QND) interferometers [4, 5].

The concepts currently being explored for third-generation detectors fall into two categories: *external readout* and *intracavity readout*. In interferometer designs with external readout topologies, light exiting the interferometer is monitored for phase shifts, which indicate the motion of the test masses. Examples include conventional interferometers and their variants (such as LIGO-I [2, 3], LIGO-II [6], and those discussed in Ref. [7]), as well as the speed-meter interferometers discussed here and in a previous paper [8]. In intracavity readout topologies, the gravitational-wave force is fed via light pressure onto a tiny internal mass, whose displacement is monitored with a local position transducer. Examples include the optical bar, symphotonic state, and optical lever schemes discussed by Braginsky, Khalili, and Gorodetsky [9–11]. These intracavity readout interferometers may be able to function at much lower light powers than external readout interferometers of comparable sensitivity because the QND readout is performed via the local position transducer (perhaps microwave-technology based), instead of via the interferometer's light; however, the designs are not yet fully developed.

At present, the most complete analysis of candidate designs for third-generation external-readout detectors has been carried out by Kimble, Levin, Matsko, Thorne, and Vyatchanin [7] (KLMTV). They examined three potential designs for interferometers that could beat the SQL: a squeezed-input interferometer, which makes use of squeezed vacuum being injected into the dark port; a variational-output scheme in which frequency-dependent homodyne detection was used; and a squeezed-variational interferometer that combines the features of both. (Because the KLMTV designs measure the relative positions of the test masses, we shall refer to them as *position meters*, particularly when we want to distinguish them from the speed meters that, for example, use variational-output techniques.) Although at least some of the KLMTV position-meter designs have remarkable performance in the lossless limit, all of them are highly susceptible to losses.

In addition, we note that the KLMTV position meters each require four kilometer-scale cavities (two arm cavities + two filter cavities). The speed meters described in this paper require at least three kilometer-scale cavities [two arm cavities + one "sloshing" cavity (described below)]. If we use

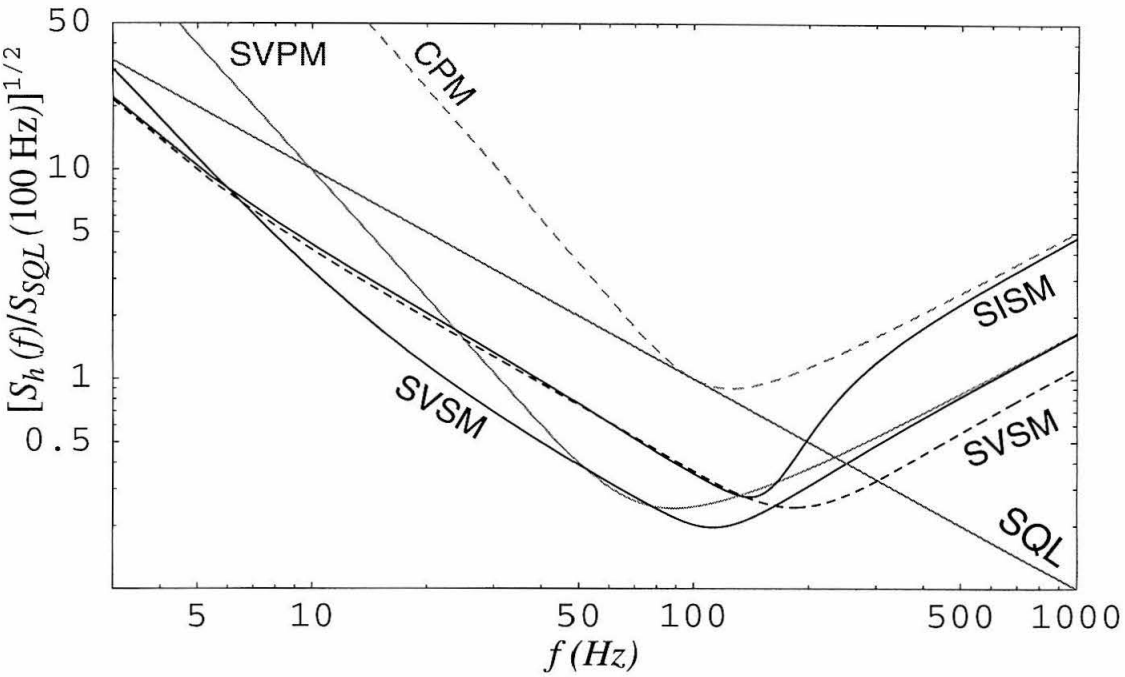

Figure 3.1: Comparison of noise curves (with losses) of several interferometer configurations. Each of these curves has been optimized in a way that is meant to illustrate their relative advantages and disadvantages. The conventional position meter (CPM) [7] has $W_{\rm circ} = 820$ kW and bandwidth $\gamma = cT/4L = 2\pi \times 100$ Hz. The squeezed-input speed meter (SISM)—optmized to agree with the conventional position meter at high frequencies—has power squeeze factor $e^{-2R} = 0.1$, optimal frequency $\omega_{\rm opt} = 2\pi \times 105$ Hz, extraction rate $\delta = 2\omega_{\rm opt}$, and sloshing frequency $\Omega = \sqrt{3}\omega_{\rm opt}$. The squeezed-variational position meter (SVPM) [7] has the same parameters as the conventional position meter, with power squeeze factor $e^{-2R} = 0.1$. There are two squeezed-variational speed-meter curves (SVSM). One (black dashes) uses the same parameters as the squeezed-input speed meter. The other (solid curve) has been optimized to compare more directly with the squeezed-variational position meter; it has $\Omega = 2\pi \times 95$ Hz and $\delta = 2\pi \times 100$ Hz (note that our δ is equivalent to the bandwidth γ used to describe the interferometers in Ref. [7]).

a variational-output technique, as KLMTV did, the resulting interferometer will have five kilometer-scale cavities (two arm cavities + one sloshing cavity + two filter cavities). This is shown in Fig. 3.4 below.

The speed meter described in this paper can achieve a performance significantly better than a conventional position meter, as shown in Fig. 3.1. (By "conventional," we mean "without any QND techniques." An example is LIGO-I.) The squeezed-input speed meter (SISM) noise curve shown in that Fig. 3.1 beats the SQL by a factor of $\sqrt{10}$ in amplitude and has *fixed-angle* squeezed vacuum injected into the dark port [this allows the interferometer to operate at a lower circulating power than would otherwise be necessary to achieve that level of sensitivity, as described by Eq. (3.3) below]. The squeezed-variational position meter (SVPM), which requires *frequency-dependent* squeezed vacuum and homodyne detection, is more sensitive than the squeezed-input speed meter over much of the

frequency range of interest, but the speed meter has the advantage at low frequencies. It should also be noted that the squeezed-variational position meter requires four kilometer-scale cavities (as described in the previous paragraph), whereas the squeezed-input speed meter requires three.

If frequency-dependent homodyne detection is added to the squeezed-input speed meter, the resulting squeezed-variational speed meter (SVSM) can be optimized to beat the squeezed-variational position meter over the entire frequency range. Figure 3.1 contains two squeezed-variational speed meter curves; one is optimized to match the squeezed-input speed meter curve at low frequencies, and the other is optimized for comparison with the squeezed-variational postion-meter curve (resulting in less sensitivity at high frequencies).

The original idea for a speed meter, as a device for measuring the momentum of a single test mass, was conceived by Braginsky and Khalili [12] and was further developed by Braginsky, Gorodetsky, Khalili, and Thorne [13] (BGKT). In their appendix, BGKT sketched a design for an interferometric gravity wave speed meter and speculated that it would be able to beat the SQL. This was verified in Ref. [8] (which appears as Chapter 2 of this thesis), where it was demonstrated that such a device could *in principle* beat the SQL by an arbitrary amount over a wide range of frequencies. However, the design presented in that paper, which we shall call the *two-cavity speed-meter* design, had three significant problems: it required (i) a high circulating power ($\sim$ 8 MW to beat the SQL by a factor of 10 in noise power at 100 Hz and below), (ii) a large amount of power coming out of the interferometer with the signal ($\sim$ 0.5 MW), and (iii) an exorbitantly high input laser power ($\gtrsim$ 300 MW). The present paper describes an alternate class of speed meters that effectively eliminate the latter two problems, and techniques for reducing the needed circulating power are discussed. These improvements bring interferometric speed meters into the realm of practicality.

A simple version of the *three-cavity speed-meter* design to be discussed in this paper is shown in Fig. 3.2. In (an idealized theorist's version of) this speed meter, the input laser light [with electric field denoted $I(\zeta)$ in Fig. 3.2] passes through a power-recycling mirror into a standard Michelson interferometer. The relative phase shifts of the two arms are adjusted so that all of the input light returns to the input port, leaving the other port dark [i.e., the interferometer is operating in the symmetric mode so $D(\eta) = 0$ in Fig. 3.2]. In effect, we have a resonant cavity shaped like $\perp$. When the end mirrors move, they will put a phase shift on the light, causing some light to enter the antisymmetric mode (shaped like $\vdash$) and come out the dark port. So far, this is the same as conventional interferometer designs (but without the optical cavities in the two interferometer arms).

Next, we feed the light coming out of the dark port [$D(\eta)$] into a sloshing cavity [labeled $K(\eta)$ and $L(\zeta)$ in Fig. 3.2]. The light carrying the position information sloshes back into the "antisymmetric cavity" with a phase shift of 180°, cancelling the position information in that cavity and leaving only a phase shift proportional to the relative velocity of the test masses[1]. The sloshing frequency

[1]The net signal is proportional to the relative velocities of the test masses, assuming that the frequencies ω of the

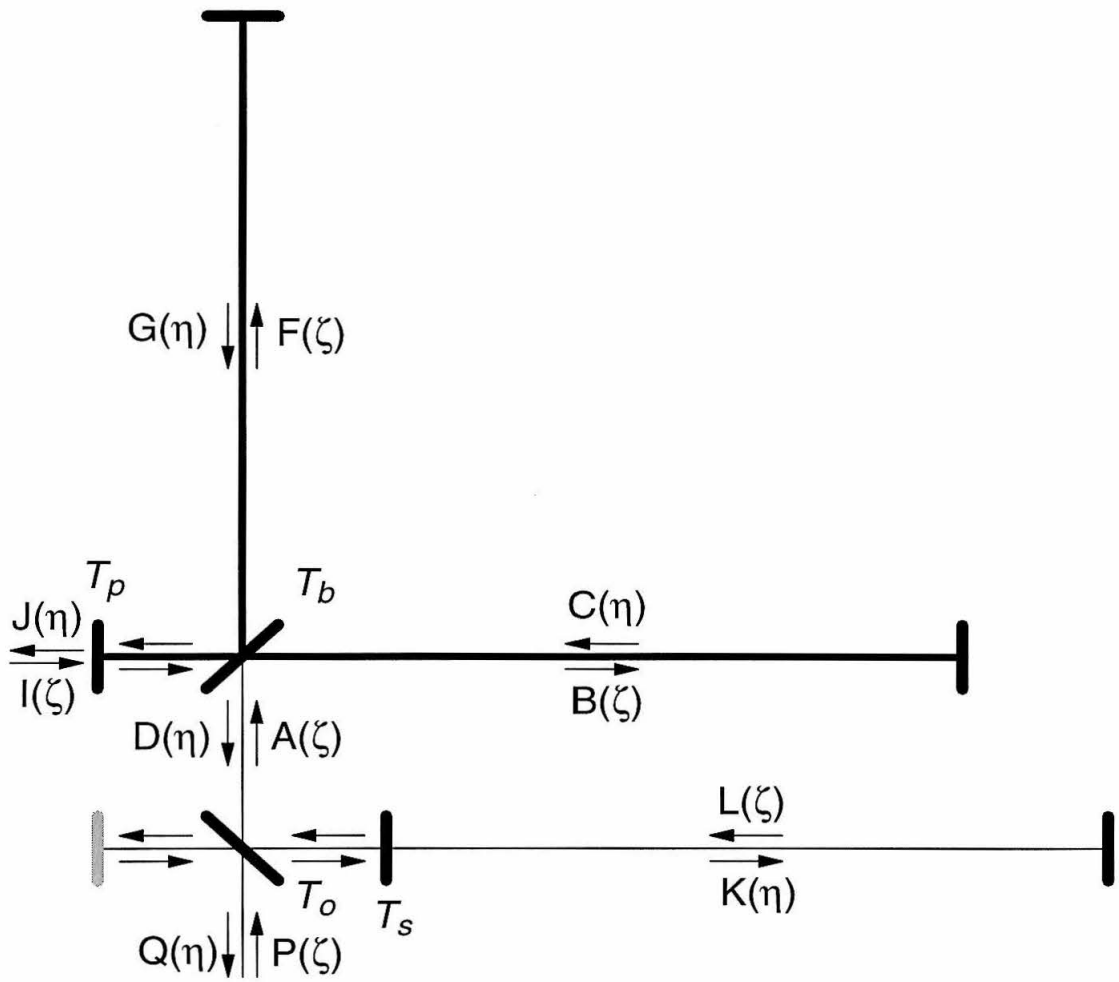

Figure 3.2: Simple version of three-cavity design for speed-meter interferometer. The main laser input port is denoted by $I(\zeta)$, where $\zeta = t - z/c$. The signal is extracted at the bottom mirror [denoted $Q(\eta)$, where $\eta = t + z/c$]. The difference between the one- and two-port versions is the mirror shown in gray.

is

$$\Omega = \frac{c\sqrt{T_s}}{2L}, \tag{3.1}$$

where T_s is the power transmissivity of the sloshing mirror, L is the common length of all three cavities, and c is the speed of light. We read the velocity signal $[Q(\eta)]$ out at a extraction mirror (with transmissivity T_o), which gives a signal-light extraction rate of

$$\delta = \frac{cT_o}{L}. \tag{3.2}$$

We have used the extraction mirror to put the sloshing cavity parallel to one of the arms of the Michelson part of the interferometer, allowing this interferometer to fit into the existing LIGO facilities. The presence of the extraction mirror essentially opens two ports to our system. We can use both outputs, or we can add an additional mirror to close one port (the gray mirror in Fig. 3.2). We will focus on the latter case in this paper.

The sensitivity h of this interferometer, compared to the SQL, can be expressed as[2]

$$\frac{h}{h_{SQL}} \sim \sqrt{\frac{W_{\rm circ}^{SQL}}{e^{2R}W_{\rm circ}}} \simeq \sqrt{\frac{800\ {\rm kW}}{e^{2R}W_{\rm circ}}}, \tag{3.3}$$

where $W_{\rm circ}$ is the power circulating in the arms, $W_{\rm circ}^{SQL} \simeq 800{\rm kW}(f_{\rm opt}/100{\rm Hz})^3$ is the power required to reach the SQL in the absence of squeezing (for the arms of length $L = 4$ km and test masses with mass $m = 40$ kg), and e^{2R} is the power squeeze factor[3]. With no squeezed vacuum, the squeeze factor is $e^{2R} = 1$, so the circulating power $W_{\rm circ}$ must be 8 MW in order to beat the SQL at $f_{\rm opt} \simeq 100$ Hz by a factor of $\sqrt{10}$ in sensitivity. With a squeeze factor of $e^{2R} = 10$, we can achieve the same performance with $W_{\rm circ} \simeq 800$ kW, which is the same as LIGO-II is expected to be.

This performance (in the lossless limit) is the same as that of the two-cavity (Chapter 2) speed meter for the same circulating power, but the three-cavity design has an overwhelming advantage in terms of required input power. However, there is one significant problem with this design that we must address: the uncomfortably large amount of laser power, equal to $W_{\rm circ}$, flowing through the beam splitter. Even with the use of squeezed vacuum, this power will be too high. Fortunately, there is a method, based on the work of Mizuno [15], that will let us solve this problem:

We add three mirrors into our speed meter (labeled $T_{\rm i}$ in Fig. 3.3); we shall call this the *practical*

test masses' motion are $\omega \ll \Omega =$ (sloshing frequency). However, the optimal regime of operation for the speed meter is $\omega \sim \Omega$. As a result, the output signal contains a sum over odd time derivatives of position [see the discussion in Sec. 3.4.1]. Therefore, the speed meter monitors not just the relative speed of the test masses, but a mixture of all odd time derivatives of the relative positions of the test masses.

[2]It should be noted that, as the power increases in Eq. (3.3), the speed-meter performance becomes more narrow band. Additional power and a re-optimization of some of the speed meter's parameters are required to maintain the same bandwidth at higher sensitivities. See Sec. 3.4.2 for details.

[3]For an explanation of squeezed vacuum and squeeze factors, see, for example, KLMTV and references cited therein. In particular, their work was based on that of Caves [14] and Unruh [4]. Also, KLMTV state that a likely achievable value for the squeeze factor (in the LIGO-III time frame) is $e^{2R} \simeq 10$, so we use that value in our discussion.

three-cavity speed meter. Two of the additional mirrors are placed in the excited arms of the interferometer to create resonating Fabry-Perot cavities in each arm (as for conventional interferometers such as LIGO-I). The third mirror is added between the beam splitter and the extraction mirror, in such a way that light with the carrier frequency resonates in the subcavity formed by this mirror and the internal mirrors.

As claimed by Mizuno [15] and tested experimentally by Freise et al. [16] and Mason [17], when the transmissivity of the third mirror decreases from 1, the storage time of sideband fields in the arm cavity due to the presence of the internal mirrors will decrease. This phenomenon is called Resonant Sideband Extraction (RSE); consequently, the third mirror is called the RSE mirror. One special case, which is of great interest to us, occurs when the RSE mirror has the same transmissivity as the internal mirrors. In this case, the effect of the internal mirrors on the gravitational-wave sidebands should be exactly cancelled out by the RSE mirror. The three new mirrors then have just one effect: they reduce the carrier power passing through the beam splitter—and they can do so by a large factor.

Indeed, we have confirmed that this is true for our speed meter, as long as the distances between the three additional mirrors (the length of the "RSE cavity") are small (a few meters), so that the phase shifts added to the slightly off-resonance sidebands by the RSE cavity are negligible. We can then adjust the transmissivities of the power-recycling mirror and of the three internal mirrors to reduce the amount of carrier power passing through the beam splitter to a more reasonable level.

With this design, the high circulating power is confined to the Fabry-Perot arm cavities, as in conventional LIGO designs. There is some question as to the level of power that mirrors will be able to tolerate in the LIGO-III time frame. Assuming that several megawatts is not acceptable, we shall show that the circulating power can be reduced by injecting fixed-angle squeezed vacuum into the dark port, as indicated by Eq. (3.3).

Going a step farther, we shall show that if, in addition to injected squeezed vacuum, we also use frequency-dependent (FD) homodyne detection, the sensitivity of the speed meter is dramatically improved at high frequencies (above $f_{\rm opt} \simeq 100$ Hz); this is shown in Fig. 3.1. The disadvantage of this is that FD homodyne detection requires two filter cavities of the same length as the arm cavities (4 km for LIGO), as shown in Fig. 3.4.

Our analysis of the losses in these scenarios indicates that our speed meters with squeezed vacuum and/or variational-output are much less sensistive to losses than a position meter using those techniques (as analyzed by KLMTV). Losses for the various speed meters we discuss here are generally quite low and are due primarily to the losses in the optical elements (as opposed to mode-mismatching effects). Without squeezed vacuum, the losses in sensitivity are less than 10% in the range $50 - 105$ Hz, lower at higher frequencies, but higher at low frequencies. Injecting fixed-angle squeezed vacuum into the dark port allows this speed meter to operate at a lower power [see Eq. 3.3],

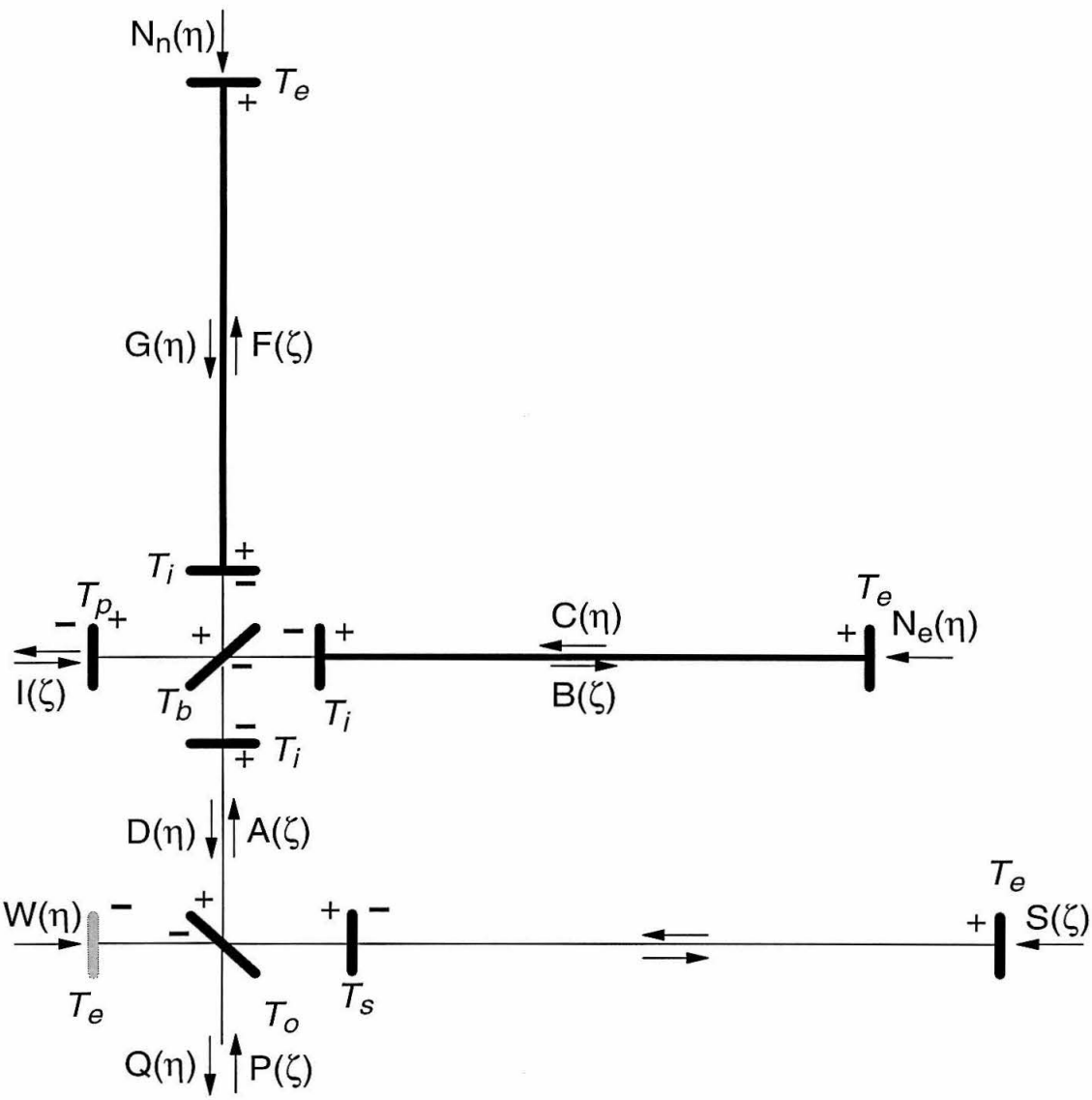

Figure 3.3: Schematic diagram showing the practical version of the three-cavity speed-meter design, which reduces the power flowing through the beam splitter. Three additional mirrors, with transmissivity T_i, are placed around the beam splitter. The "+" and "−" signs near the mirrors indicate the sign of the reflectivities in the junction conditions for each location. The mirror shown in gray closes the second port of the interferometer.

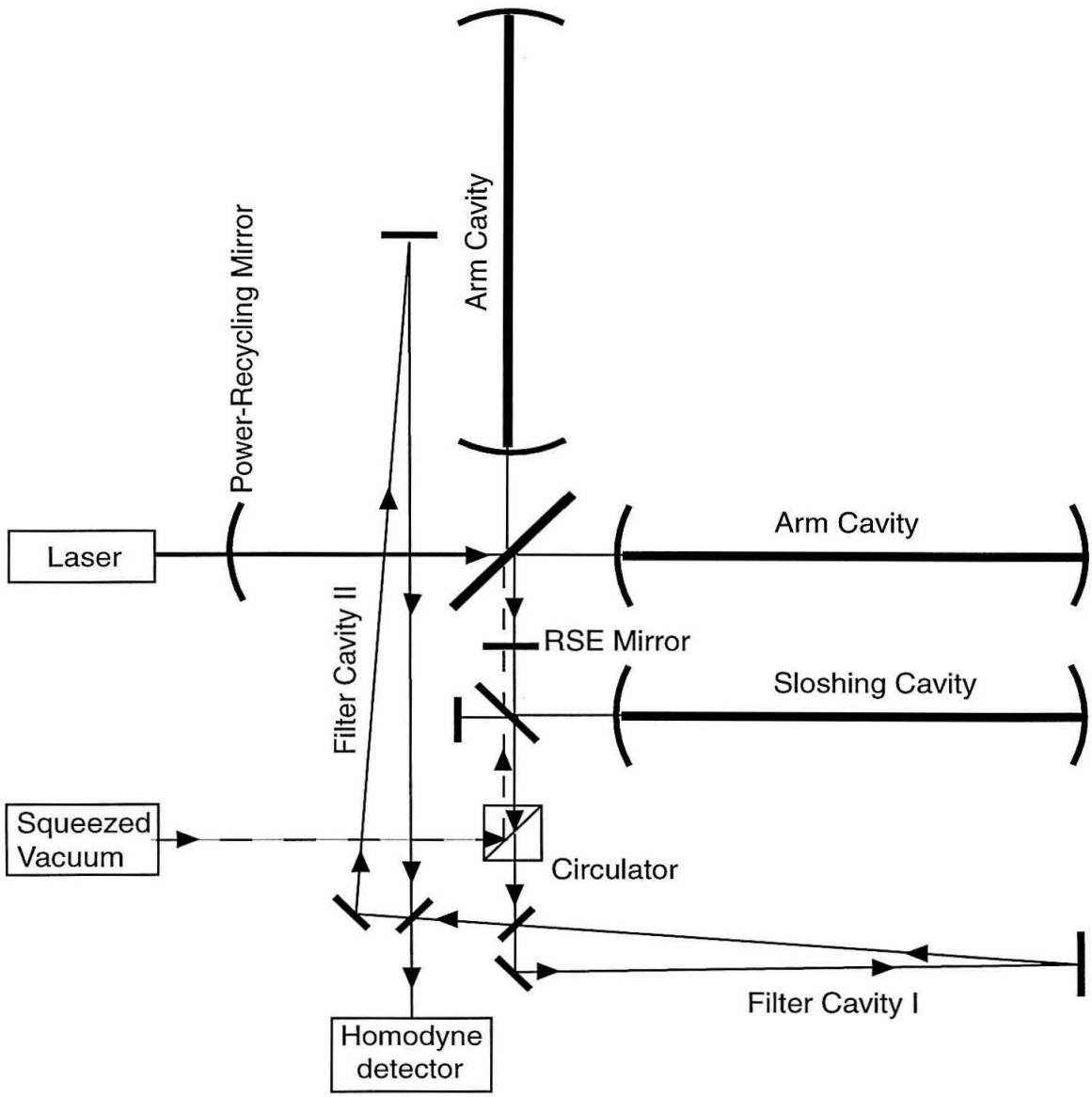

Figure 3.4: Schematic diagram showing the practical three-cavity speed-meter design with squeezed vacuum injected at the dark port and two filter cavities on the output. Note that the circulator is a four-port optical device that separates the injected (squeezed) input and the interferometer's output.

thereby reducing the dominant losses (which are dependent on the circulating power because they come from vacuum fluctations contributing to the back-action). In this case, the losses are less than 4% in the range $25 - 150$ Hz. As before, they are lower at high frequencies, but they increase at low frequencies. Using FD homodyne detection does not change the losses significantly.

This paper is organized as follows: In Sec. 3.3 we give a brief description of the mathematical method that we use to analyze the interferometer. In Sec. 3.4.1, we present the results in the lossless case, followed in Sec. 3.4.2 by a discussion of optimization methods. In Sec. 3.4.3, we discuss some of the advantages and disadvantages of this design, including the reasons it requires a large circulating power. Then in Sec. 3.5, we show how the circulating power can be reduced by injecting squeezed vacuum through the dark port of the interferometer and how the use of frequency-dependent homodyne detection can improve the performance at high frequencies. In Section 3.6, we discuss the effect of losses on our speed meter with the various modifications made in Sec. 3.5, and we compare our interferometer configurations with those of KLMTV. Finally, we summarize our results in Sec. 3.7.

3.3 Mathematical Description of the Interferometer

The interferometers in this paper are analyzed using the techniques described in Sec. 2.3. These methods are based on the formalism developed by Caves and Schumaker [18, 19] and used by KLMTV to examine more conventional interferometer designs. For completeness, we will summarize the main points here.

The electric field propagating in each direction down each segment of the interferometer is expressed in the form

$$E_{\text{field}}(\zeta) = \sqrt{\frac{4\pi\hbar\omega_0}{\mathcal{S}c}}A(\zeta)\,. \tag{3.4}$$

Here $A(\zeta)$ is the amplitude (which is denoted by other letters—$B(\zeta)$, $P(\zeta)$, etc.—in other parts of the interferometer; see Fig. 3.2), $\zeta = t - z/c$, ω_0 is the carrier frequency, $\hbar$ is the reduced Planck's constant, and $\mathcal{S}$ is the effective cross-sectional area of the light beam; see Eq. (8) of KLMTV. For light propagating in the negative z direction, $\zeta = t - z/c$ is replaced by $\eta = t + z/c$. We decompose the amplitude into cosine and sine quadratures,

$$A(\zeta) = \mathcal{A}_1(\zeta)\cos\omega_0\zeta + \mathcal{A}_2(\zeta)\sin\omega_0\zeta\,, \tag{3.5}$$

where the subscript 1 always refers to the cosine quadrature, and 2 to sine. Both arms and the sloshing cavity have length $L = 4$ km, whereas all of the other lengths z_i are short compared to L. We choose the cavity lengths to be exact half multiples of the carrier wavelength so $e^{i2\omega_0 L/c} = 1$ and $e^{i2\omega_0 z_i/c} = 1$. There will be phase shifts put onto the sideband light in all of these cavities, but

only the phase shifts due to the long cavities are significant.

The aforementioned sidebands are put onto the carrier by the mirror motions and by vacuum fluctuations. We express the quadrature amplitudes for the carrier plus the side bands in the form

$$\mathcal{A}_j(\zeta) = A_j(\zeta) + \int_0^\infty [\tilde{a}_j(\omega)e^{-i\omega\zeta} + \tilde{a}_j^\dagger(\omega)e^{i\omega\zeta}]\frac{d\omega}{2\pi}\,. \tag{3.6}$$

Here $A_j(\zeta)$ is the carrier amplitude, $\tilde{a}_j(\omega)$ is the field amplitude (a quantum mechanical operator) for the sideband at sideband frequency ω (absolute frequency $\omega_0 \pm \omega$) in the j quadrature, and $\tilde{a}_j^\dagger(\omega)$ is the Hermitian adjoint of $\tilde{a}_j(\omega)$; cf. Eqs. (6)–(8) of KLMTV, where commutation relations and the connection to creation and annihilation operators are discussed. In other portions of the interferometer (Fig. 3.2), $\mathcal{A}_j(\zeta)$ is replaced by, e.g., $\mathcal{C}_j(\zeta)$; $A_j(\zeta)$, by $C_j(\zeta)$; $\tilde{a}_j(\omega)$, by $\tilde{c}_j(\omega)$, etc.

Since each mirror has a power transmissivity and complementary reflectivity satisfying the equation $T + R = 1$, we can write out the junction conditions for each mirror in the system, for both the carrier quadratures and the sidebands [see particularly Eqs. (2.5) and (2.12)–(2.14)]. We shall denote the power transmissivities for the sloshing mirror as T_s, for the extraction (output) mirror as T_o, the power-recycling mirror as T_p, for the beam-splitter as $T_\mathrm{b} = 0.5$, for the internal mirrors as T_i, and for the end mirrors as T_e; see Figs. 3.2 and 3.3.

The resulting equations can be solved simultaneously to get expressions for the carrier and sidebands in each segment of the interferometer. Since those expressions may be quite complicated, we use the following assumptions to simplify our results. First, we assume that only the cosine quadrature is being driven (so that the carrier sine quadrature terms are all zero). Second, we assume that the transmissivities obey

$$1 \gg T_\mathrm{o} \gg T_\mathrm{s} \gg T_\mathrm{e} \quad \text{and} \quad 1 \gg \{T_\mathrm{p}, T_\mathrm{i}\} \gg T_\mathrm{e}\,. \tag{3.7}$$

The motivations for these assumptions are that (i) they lead to speed-meter behavior; (ii) as with any interferometer, the best performance is achieved by making the end-mirror transmissivities T_e as small as possible; and (iii) good performance requires a light extraction rate comparable to the sloshing rate, $\delta \sim \Omega$ [cf. the first paragraph of Sec. 2.4.2], which with Eqs. (3.1) and (3.2) implies $T_\mathrm{o} \sim \sqrt{T_\mathrm{s}}$ so $T_\mathrm{o} \gg T_\mathrm{s}$. Throughout the paper, we will be using these assumptions, together with $\omega L/c \ll 1$, to simplify our expressions.

3.4 Speed Meter in the Lossless Limit

For simplicity, in this section we will set $T_\mathrm{e} = 0$ (end mirrors perfectly reflecting). We will also neglect the (vacuum-fluctuation) noise coming in the main laser port ($\tilde{i}_{1,2}$) since that noise largely exits back toward the laser and produces negligible noise on the signal light exiting the output port.

As a result of these assumptions, the only (vacuum-fluctuation) noise that remains is that which comes in through the output port ($\tilde{p}_{1,2}$). An interferometer in which this is the case and in which light absorption and scattering are unimportant ($R + T = 1$ for all mirrors, as we have assumed) is said to be "lossless." In Sec. 3.6, we shall relax these assumptions; i.e., we shall consider lossy interferometers.

It should be noted that the results and discussion in this section and in Sec. 3.5 apply to both the simple and practical versions of the three-cavity speed meter (Figs. 3.2 and 3.3). The two versions are completely equivalent (in the lossless limit).

3.4.1 Mathematical Analysis

The lossless interferometer output for the speed meters in Fig. 3.2 and 3.3, as derived by the analysis sketched in the previous section, is then

$$\tilde{q}_1 = -\frac{\mathcal{L}^*(\omega)}{\mathcal{L}(\omega)}\tilde{p}_1 , \tag{3.8a}$$

$$\tilde{q}_2 = \frac{2i\omega\sqrt{\omega_0 \delta W_{\rm circ}}}{\sqrt{\hbar c L}\mathcal{L}(\omega)}\tilde{x} - \frac{\mathcal{L}^*(\omega)}{\mathcal{L}(\omega)}\tilde{p}_2 . \tag{3.8b}$$

Here $\tilde{p}_j(\omega)$ is the side-band field operator [analog of $\tilde{a}_j(\omega)$ in Eq. (3.6)] associated with the dark-port input $P(\zeta)$, and $\tilde{q}_j(\omega)$ associated with the output $Q(\eta)$; see Fig. 3.2. Also, in Eqs. (3.8), $\mathcal{L}(\omega)$ is a c-number given by

$$\mathcal{L}(\omega) = \Omega^2 - \omega^2 - i\omega\delta \tag{3.9}$$

[recalling that $\Omega = c\sqrt{T_{\rm s}}/2L$ is the sloshing frequency, $\delta = cT_{\rm o}/L$ the extraction rate], the asterisk in $\mathcal{L}^*(\omega)$ denotes the complex conjugate, $\tilde{x}(\omega)$ is the Fourier transform of the relative displacement of the four test masses—i.e., the Fourier transform of the difference in lengths of the interferometer's two arm cavities—and $W_{\rm circ}$ is the circulating power in the each of the interferometer's two arms. Note that the circulating power (derived as in Sec. 2.3.2) is related to the carrier amplitude B_1 in the arms by[4]

$$W_{\rm circ} = \frac{1}{2}\hbar\omega_0 B_1^2 = \frac{4\hbar\omega_0 I_1^2}{T_{\rm i}T_{\rm p}} , \tag{3.10}$$

where I_1 is the input laser amplitude (in the cosine quadrature). Readers who wish to derive the input–output relations (3.8) for themselves may find useful guidance in Appendix B of KLMTV [7] and in Secs. 2.3 and 2.4, which give detailed derivations for other interferometer designs.

Notice that the first term in Eq. (3.8b) contains $\tilde{x}$ only in the form $\omega\tilde{x}$; this is the velocity signal

[4]Equation (3.10) refers specifically to the practical version of the three-arm interferometer (Fig. 3.3). The simple (Fig. 3.2) version would be

$$W_{\rm circ} = \frac{1}{2}\hbar\omega_0 B_1^2 = \frac{\hbar\omega_0 I_1^2}{T_{\rm p}} .$$

[actually, the sum of the velocity and higher odd time derivatives of position because of the $\mathcal{L}(\omega)$ in the denominator]. The test masses' relative displacement $\tilde{x}(\omega)$ is given by

$$\tilde{x} = \tilde{x}_e - \tilde{x}_n = L\tilde{h} - \frac{8i\sqrt{\hbar\omega_0\delta W_{\rm circ}}}{m\omega\sqrt{cL}\mathcal{L}(\omega)}\tilde{p}_1 \,, \tag{3.11}$$

where $\tilde{x}_e$ is the Fourier transform of the relative displacement of the mirrors of the "east" arm and $\tilde{x}_n$ is the same for the "north" arm. The last term is the back-action produced by fluctuating radiation pressure (derived as in Sec. 2.3.2).

It is possible to express Eqs. (3.8) in a more concise form, similar to Eqs. (16) in KLMTV:

$$\tilde{q}_1 = \Delta\tilde{p}_1 = \tilde{p}_1 e^{2i\psi} \,, \tag{3.12a}$$

$$\tilde{q}_2 = \Delta\tilde{p}_2 + \sqrt{2\kappa}\frac{\tilde{h}}{h_{SQL}}e^{i\psi} \,, \quad \Delta\tilde{p}_2 = (\tilde{p}_2 - \kappa\tilde{p}_1)e^{2i\psi} \,. \tag{3.12b}$$

Here

$$\tan\psi = -\frac{\Omega^2 - \omega^2}{\omega\delta} \tag{3.13}$$

is a phase shift put onto the light by the interferometer,

$$\kappa = \frac{16\omega_0\delta W_{\rm circ}}{mcL|\mathcal{L}(\omega)|^2} \tag{3.14}$$

is a dimensionless coupling constant that couples the gravity wave signal $\tilde{h}$ into the output $\tilde{q}_2$, and

$$h_{SQL} = \sqrt{\frac{8\hbar}{m\omega^2 L^2}} \tag{3.15}$$

is the standard quantum limit for a conventional interferometer such as LIGO-I or VIRGO [1].

In Fig. 3.5, we plot the coupling constant κ as a function of frequency for several values of δ. As the graph shows, κ can be roughly constant for a rather broad frequency band $\omega \lesssim \Omega$, when δ is chosen to be $\sim \Omega$ (as it will be when the interferometer is optimized). Combining this with the fact that $h_{SQL} \propto 1/\omega$, we infer from Eqs. (3.12) that the output *signal* at frequencies $\omega \lesssim \Omega$ is proportional to $\omega\tilde{h}$, or equivalently $\omega\tilde{x}$, which is the relative speed of the test masses (as mentioned above).

The terms $\Delta\tilde{p}_1$ and $\Delta\tilde{p}_2$ in Eqs. (3.8) represent *quantum noise* (shot noise, radiation-pressure noise, and their correlations). We shall demonstrate below that, in the frequency band $\omega \lesssim \Omega$ where the interferometer samples only the speed, there is no back-action (radiation-pressure) noise. This might not be obvious from Eqs. (3.12), especially because they have an identical form (except for the frequency dependence of κ) as the input-output relations of a conventional interferometer, where the term proportional to $\mathcal{K}$ (their version of κ) *is* the radiation-pressure noise. Indeed, if one measures

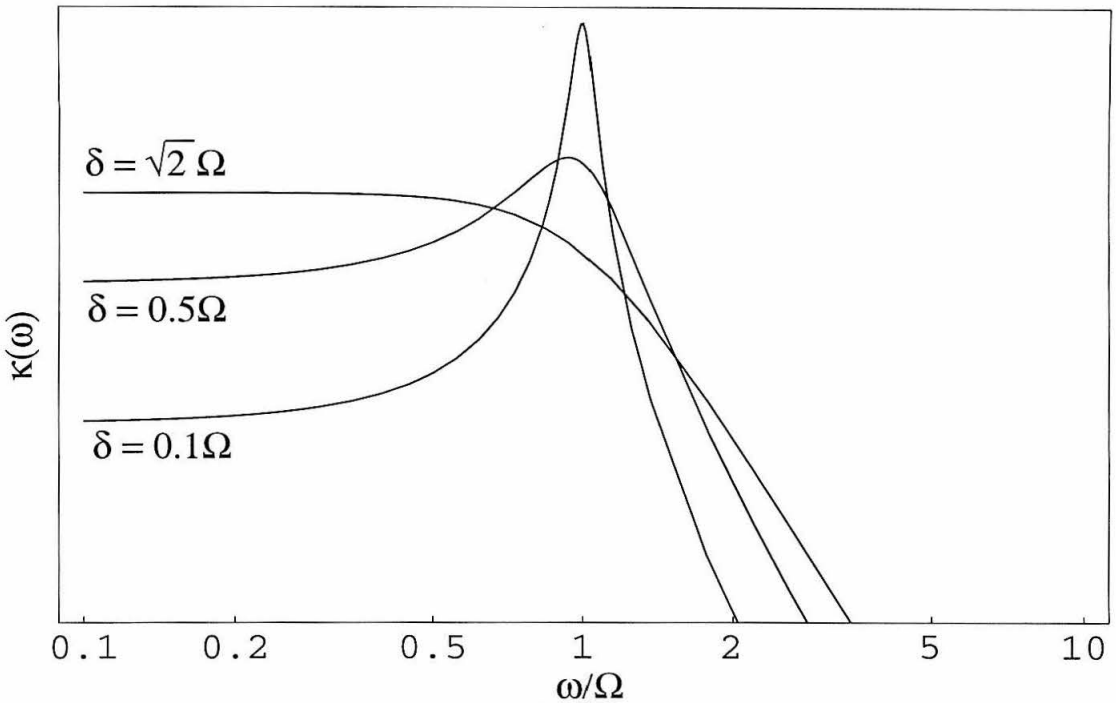

Figure 3.5: The coupling constant $\kappa(\omega)$ in arbitrary (logrithmic) units with ω measured in units of Ω. The three curves correspond to the same light power (such that $\kappa_{\max} = 5$ for the middle curve), but $\delta = 0.1\Omega$, $\delta = 0.5\Omega$, and $\delta = \sqrt{2}\Omega$.

the "sine" quadrature of the output, $\tilde{q}_2$, as is done in a conventional interferometer, this speed meter turns out to be SQL limited, as are conventional interferometers.

Fortunately, the fact that κ is constant (and equal to κ_0) over a broad frequency band will allow the aforementioned cancellation of the back-action, resulting in a QND measurement of speed. To see this, suppose that, instead of measuring the output phase quadrature $\tilde{q}_2$, we use homodyne detection to measure a generic, frequency-independent quadrature of the output:

$$\tilde{q}_\Phi = \Delta\tilde{p}_1 \cos\Phi + (\Delta\tilde{p}_2 + \sqrt{2\kappa}\frac{h}{h_{SQL}}e^{i\psi})\sin\Phi\,, \tag{3.16}$$

where Φ is a fixed homodyne angle. Then from Eqs. (3.8), we infer that the noise in the signal, expressed in GW strain units h, is

$$h_n = \frac{h_{SQL}}{\sqrt{2\kappa}}e^{i\psi}[\tilde{p}_1(\cot\Phi - \kappa) + \tilde{p}_2]\,. \tag{3.17}$$

By making $\cot\Phi = \kappa_0 \equiv$ (constant value of κ at $\omega \lesssim \Omega$), the radiation pressure noise in h_n will be cancelled in the broad band where $\kappa = \kappa_0$, thereby making this a QND interferometer.

We assume for now that ordinary vacuum enters the output port of the interferometer; i.e., $\tilde{p}_1$ and

$\tilde{p}_2$ are quadrature amplitudes for ordinary vacuum (we will inject squeezed vacuum in Sec. 3.5.1). This means [Eq. (26) of KLMTV] that their (single-sided) spectral densities are unity and their cross-correlations are zero, which, when combined with Eq. (3.17), implies a spectral density of

$$S_{h_n} = (h_{SQL})^2 \xi^2 \,. \tag{3.18}$$

Here

$$\xi^2 \equiv \frac{(\cot\Phi - \kappa)^2 + 1}{2\kappa} \tag{3.19}$$

is the fractional amount by which the SQL is beaten (in units of squared amplitude). This expression for ξ^2 is the same as that for the speed meters in Eq. (2.36) and BGKT [Eq. (40)], indicating the theoretical equivalency of these designs. In those papers, an optimization is given for the interferometer. Instead of just using the results of that optimization, we shall carry out a more comprehensive study of it[5].

3.4.2 Optimization

The possible choices of speed meter parameters can be investigated intuitively by examining the behavior of κ. To aid us in our exploration, we choose (as in BGKT and Chapter 2) to express $|\mathcal{L}(\omega)|^2$ [Eq. (3.9)] as

$$|\mathcal{L}(\omega)|^2 = (\omega^2 - \omega_{\rm opt}^2)^2 + \delta^2(\omega_{\rm opt}^2 + \delta^2/4)\,, \tag{3.20}$$

where

$$\omega_{\rm opt} = \sqrt{\Omega^2 - \delta^2/2}\,, \tag{3.21}$$

is the interferometer's "optimal frequency," i.e., the frequency at which $|\mathcal{L}(\omega)|$ reaches its minimum. Combining with Eq. (3.14), we obtain

$$\kappa = \frac{\Omega_{\rm I}^3\,\delta}{(\omega^2 - \omega_{\rm opt}^2)^2 + \delta^2(\omega_{\rm opt}^2 + \delta^2/4)}\,, \tag{3.22}$$

where

$$\Omega_{\rm I}^3 \equiv \frac{16\omega_0 W_{\rm circ}}{mLc} \tag{3.23}$$

[5]It should be noted that the expressions given in Sec. 3.4.1 are accurate to 6% or better over the frequency range of interest. To achieve 1% accuracy, we expand to the next-highest order. The result can be expressed as a re-definition of the sloshing frequency

$$\Omega^2 \to \Omega'^2 = \Omega^2 - \delta\delta_{\rm s}/2\,,$$

where $\delta_{\rm s} = cT_{\rm s}/2L$. Then κ retains the same functional form:

$$\kappa \to \kappa' = \frac{16\omega_0\delta W_{\rm circ}}{mcL((\Omega'^2 - \omega^2) + \omega^2\delta^2)}\,.$$

As a result, the optimization described in Sec. 3.4.2 applies equally well to κ' and Ω' as to the original κ and Ω.

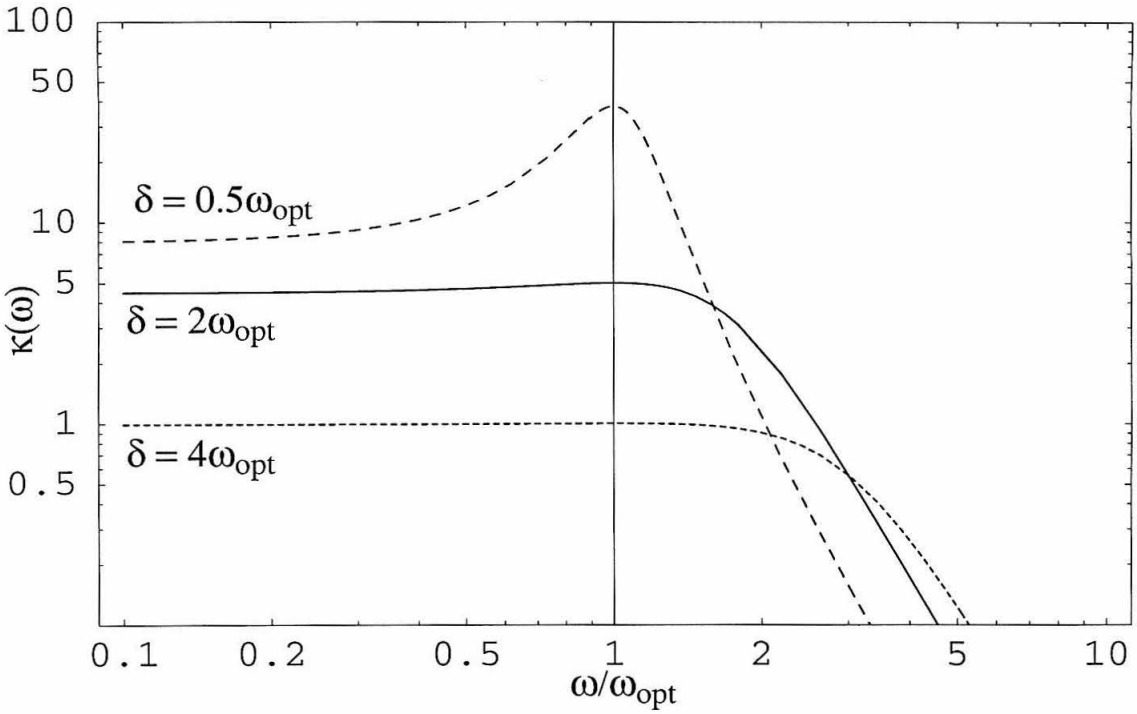

Figure 3.6: The coupling constant $\kappa(\omega)$ with ω measured in units of $\omega_{\rm opt}$. The solid curve is determined by setting $\delta = 2\omega_{\rm opt}$ and $\kappa_{\rm max} = 5$ (this value of $\kappa_{\rm max}$ comes from specifying that we want to beat the SQL by a factor of 10; see Fig. 3.7). If, in addition, we set $\omega_{\rm opt} = 2\pi \times 100$ Hz, then all the parameters have been specified (due to the various relationships between them) and are equal to the values given in Table 3.1. If we maintain the same power but change δ, then the only parameter of Table 3.1 that is affected is $T_{\rm o}$. Examples of such a change are shown for $\delta = 0.5\omega_{\rm opt}$ and $\delta = 4\omega_{\rm opt}$. Note that these two choices of δ are more extreme than would be desirable in practice, but they are shown here to illustrate more clearly the effect on κ of changing the ratio between δ and $\omega_{\rm opt}$.

is a frequency scale related to the circulating power. At $\omega_{\rm opt}$, κ reaches its maximum (see Fig. 3.6)

$$\kappa_{\rm max} = \frac{\Omega_{\rm I}^3}{\delta(\omega_{\rm opt}^2 + \delta^2/4)} \,. \tag{3.24}$$

By setting

$$\cot\Phi = \kappa_{\rm max} \,, \tag{3.25}$$

we get the maximum amount by which a speed meter can beat the SQL

$$\xi_{\rm min}^2 = \frac{1}{2\kappa_{\rm max}} = \frac{\delta(\omega_{\rm opt}^2 + \delta^2/4)}{2\Omega_{\rm I}^3} \,. \tag{3.26}$$

As ω differs from $\omega_{\rm opt}$ in either direction, κ decreases from $\kappa_{\rm max}$. This causes the noise to increase since (i) the term $(\cot\Phi - \kappa)^2$ in the numerator of ξ^2 [Eq. (3.19)] increases and (ii) the denominator

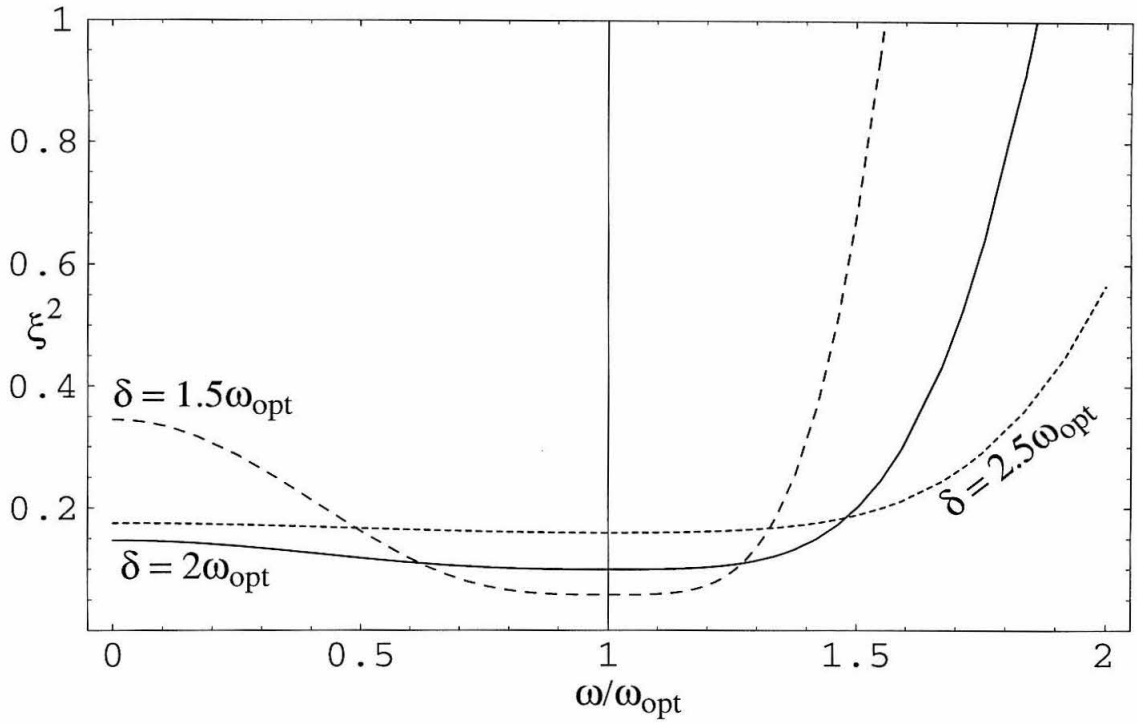

Figure 3.7: The squared amount by which the speed meter beats the SQL with a given circulating power, which is determined by setting (for the solid curve) $\xi^2_{\rm min} = 0.1$ and the condition (3.29). Note that the requirement on $\xi^2_{\rm min}$ sets the power relative to the SQL power $W^{SQL}_{\rm circ}$, the value of which is dependent on $\omega_{\rm opt}$. (For $\omega_{\rm opt} = 100$ Hz, we have $W_{\rm circ} = 8$ MW.) If we hold the power fixed and change δ to $1.5\omega_{\rm opt}$ and $2.5\omega_{\rm opt}$, we get the other two curves.

of ξ^2 decreases. In order to have broadband performance, we should make the peak of $\kappa(\omega)$ as flat as possible. As we can see from both Eq. (3.22) and Fig. 3.6, the shape of the peak can be adjusted by changing δ: for the same optical power, a larger δ means a wider peak but a smaller maximum. Therefore, changing δ is one method of balancing sensitivity against bandwidth. Some examples are shown in Figs. 3.6, 3.7, and 3.8, where $\kappa(\omega)$, $\xi^2(\omega)$, and $S_h(\omega)$, respectively, are plotted for configurations with the same $\omega_{\rm opt}$ and optical power $W_{\rm circ}$, but with several values of δ.

To be more quantitative, a simple analytic form for $\xi^2(\omega)$ can be obtained by inserting Eqs. (3.22), (3.24), and (3.26) into Eq. (3.19) to get

$$\xi^2(\omega) = \left[1 + \Delta + \frac{1}{4\xi^4_{\rm min}} \frac{\Delta^2}{(1+\Delta)}\right] \xi^2_{\rm min} \,. \tag{3.27}$$

Here

$$\Delta \equiv \frac{\left(\omega^2 - \omega^2_{\rm opt}\right)^2}{\delta^2(\omega^2_{\rm opt} + \delta^2/4)} \tag{3.28}$$

is a dimensionless offset from the optimal frequency $\omega_{\rm opt}$. From Eq. (3.28), it is evident that Δ, and

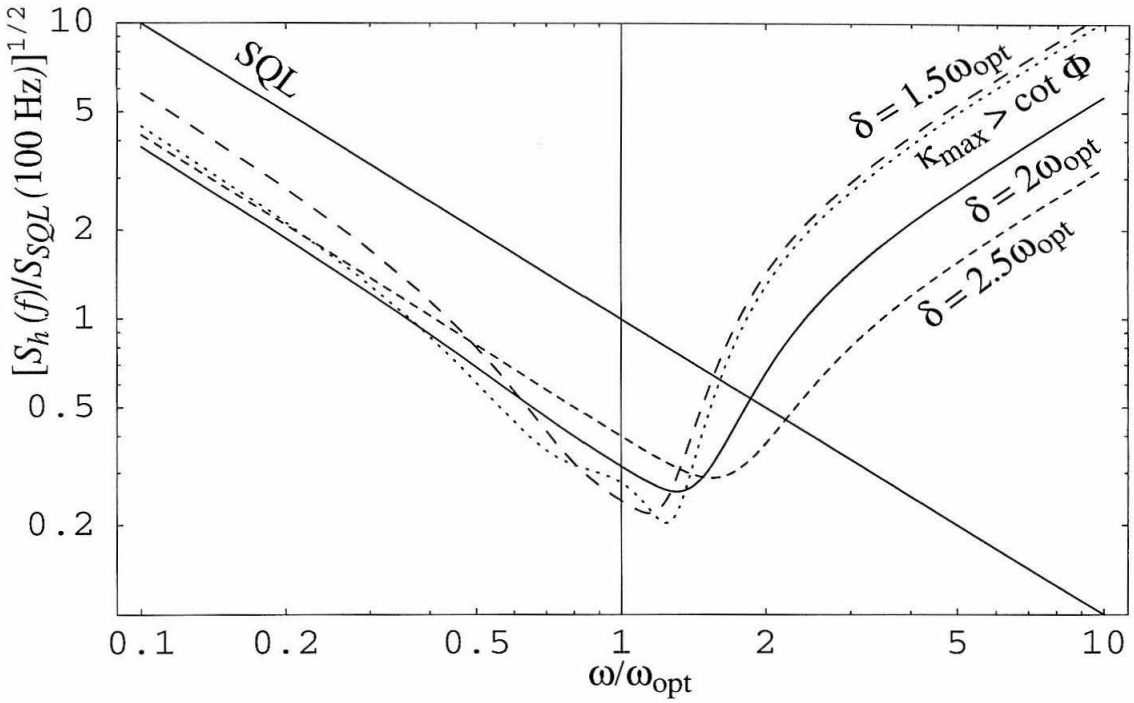

Figure 3.8: Noise curves corresponding to the ξ^2 curves in Fig. 3.7, the caption of which describes the parameters used here as well. The dotted line is an example of a noise curve for which κ is not quite flat and $\cot\Phi$ was chosen to be slightly smaller than κ_{max} (see the end of Sec. 3.4.2 for details.)

thus ξ^2, are the same for $\omega = 0$ and $\omega = \sqrt{2}\omega_{opt}$ [see also Eq. (47) of BGKT or Eq. (2.50)]. For definiteness, let us impose that

$$\xi^2(0) = \xi^2(\sqrt{2}\omega_{opt}) = \frac{3}{2}\xi^2_{min} \tag{3.29}$$

as is done by BGKT. For $\xi^2_{min} = 0.1$, this gives $\delta = 1.977\omega_{opt} \approx 2\omega_{opt}$ (as assumed in BGKT and Chapter 2). Plugging these numbers into Eq. (3.26) and combining with Eq. (3.23) gives

$$\begin{aligned} W_{circ}(\delta = 2\omega_{opt}) &= \frac{mLc\,\omega^3_{opt}}{8\omega_0\xi^2_{min}} \\ &\simeq 8.4\,\mathrm{MW}\left(\frac{\omega_{opt}}{2\pi\times 100\,\mathrm{Hz}}\right)^3\left(\frac{m}{40\,\mathrm{kg}}\right) \\ &\quad\times\left(\frac{L}{4000\,\mathrm{km}}\right)\left(\frac{1.78\times 10^{15}\,\mathrm{Hz}}{\omega_0}\right)\left(\frac{0.1}{\xi^2_{min}}\right). \end{aligned} \tag{3.30}$$

Therefore, when ω_{opt} is chosen at $2\pi \times 100\,\mathrm{Hz}$, this speed meter (with $\delta = 2\omega_{opt}$) requires $W_{circ} \simeq 8.4\,\mathrm{MW}$ to beat the SQL by a factor of 10 in power ($\xi^2_{min} = 0.1$). [Note that, keeping $\delta = 2\omega_{opt}$, the speed meter reaches the SQL with $W^{SQL}_{circ} = 840\,\mathrm{kW}$, comparable to the value given by KLMTV Eq. (132) for conventional interferometers with 40-kilogram test masses.] The ξ^2 and S_h curves for

this configuration are plotted as solid lines in Fig. 3.7 and 3.8, respectively.

Please note that Eq. (3.30) should be applied with caution because significantly changing $\xi^2_{\rm min}$ in the above equation (without changing the ratio between δ and $\omega_{\rm opt}$) will change the wide-band performance of the interferometer, since there is some "hidden" power dependence in Eq. (3.29). To determine the behavior of the speed meter with significantly higher power or lower $\xi^2_{\rm min}$ *while maintaining the same wideband performance*, we must re-apply the requirement (3.29) to determine the appropriate ratio between δ and $\omega_{\rm opt}$. For example, solving Eqs. (3.26) and (3.29) simultaneously for $\xi^2_{\rm min}$ and δ, with chosen values $W_{\rm circ} = 20$ MW and $\omega_{\rm opt} = 2\pi \times 100$ Hz, gives $\delta = 2.334\omega_{\rm opt}$ and $\xi^{-2}_{\rm min} \simeq 17$. Keeping this in mind, a general expression for the circulating power is

$$\begin{aligned} W_{\rm circ} &= \frac{mLc(\omega_{\rm opt}^2 + \delta^2/4)\delta}{32\omega_0\,\xi^2_{\rm min}} \\ &= \frac{209\,{\rm kW}}{\xi^2_{\rm min}}\left[\frac{(\omega_{\rm opt}^2 + \delta^2/4)\delta}{(2\pi \times 100\,{\rm Hz})^3}\right]\left(\frac{m}{40\,{\rm kg}}\right)\left(\frac{L}{4000\,{\rm km}}\right)\left(\frac{1.78\times 10^{15}\,{\rm Hz}}{\omega_0}\right), \end{aligned} \tag{3.31}$$

where the relationship between δ and $\omega_{\rm opt}$ determines whether the noise curve is deep but narrow or wide but shallow [with the requirement (3.29) giving the latter].

So far, we have only changed δ to modify the performance of the speed meter. Another method is to change $\omega_{\rm opt}$. In this case, the shape of the noise curve changes very little, but the minima occur at different frequencies, causing the interferometer to have either broader bandwidth or higher sensitivity (relative to the SQL). This is shown in Fig. 3.9. Maintaining condition (3.29) with $\omega_{\rm opt}$ chosen at $2\pi \times 150$ Hz, we get a broader but shallower curve (short dashes); this configuration beats the SQL by a factor of $\xi^{-2}_{\rm min} \sim 4.7$, up to $f \sim 240$ Hz. With $\omega_{\rm opt} = 2\pi \times 75$ Hz, we get a narrower but deeper curve (long dashes), which beats the SQL by a factor of $\xi^{-2}_{\rm min} \sim 17$, up to $f \sim 100$ Hz. The power was kept fixed at $W_{\rm circ} = 8.2$ MW.

One more potential optimization method is to choose a κ with a peak that is not quite flat and then choose a $\cot\Phi$ that is slightly smaller than $\kappa_{\rm max}$. This will give a wider bandwidth on either side of $\omega_{\rm opt}$, at the price of decreased sensitivity at the region near $\omega_{\rm opt}$ (see dotted line in Fig. 3.8).

For simplicity, we will choose a typical (but somewhat arbitrary) set of parameters for the lossless interferometer of Fig. 3.2. These values, given in Table 3.1, will be used (except as otherwise noted) for subsequent plots and calculations comparing this speed-meter design to other configurations.

3.4.3 Discussion of Three-Cavity Speed-Meter Design

In this section, we discuss how the three-cavity speed-meter design compares to the two-cavity design presented in Chapter 2, focusing on the three major problems of that design: it required (i) a high circulating power, (ii) a large amount of power coming out of the interferometer with the signal, and (iii) an exorbitantly high input laser power.

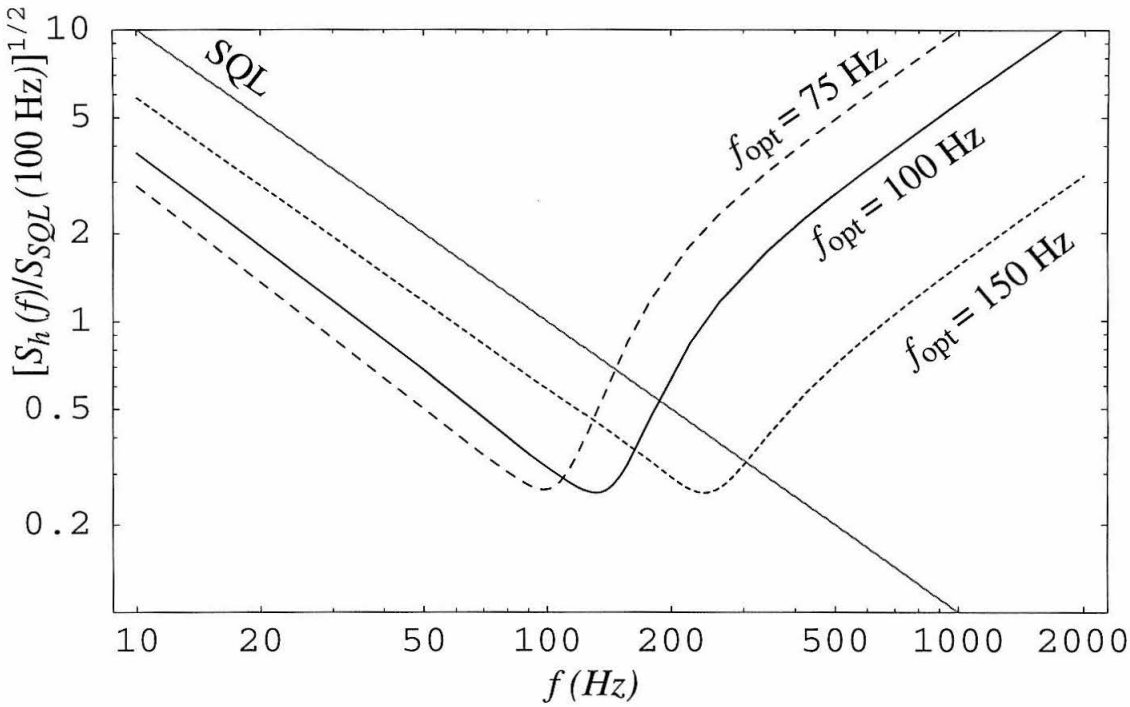

Figure 3.9: Noise curves for varying optimal frequencies. The solid curve has $f_{\rm opt} = 100$ Hz and is identical to the solid curve of Fig. 3.8. Maintaining the same power and the condition imposed by Eq. (3.29), we show two examples of noise curves with other optimal frequencies, specifically $f_{\rm opt} = 75$ Hz and $f_{\rm opt} = 150$ Hz.

With the three-cavity speed meter, we are able to replicate the performance of the two-cavity design in Chapter 2, but without the exorbitantly high input power. The reason why our three-cavity speed meter does not need a high input power is the same as for conventional interferometers: in both cases, the excited cavities are fed directly by the laser. According to Bose statistics, carrier photons will be "sucked" into the cavities, producing a strong amplification. This was not the case in the two-cavity speed meter of Chapter 2. There, an essentially empty cavity stood between the input and the excited cavity, thereby thwarting Bose statistics and resulting in a required input laser power much greater than the power that was circulating in the excited cavity (see Chapter 2 for more details). In this chapter, we have returned to a case where the laser is driving an excited cavity directly, thereby allowing the input laser power to be small relative to the circulating power.

Because the cavity from which we are reading out the signal does not contain large amounts of carrier light (by contrast with the two-cavity design), this three-cavity speed meter does not have large amounts of power exiting the interferometer with the velocity signal, unlike the two-cavity design. By making use of the different modes of the Michelson interferometer, we have solved the problem of the exorbitantly high input power and the problem of the amount of light that comes out of the interferometer.

Table 3.1: Three-arm speed-meter interferometer parameters and their fiducial values, as used throughout except where other parameters are specified.

Parameter	Symbol	Fiducial Value
carrier frequency	ω_0	$1.78 \times 10^{15}\mathrm{s}^{-1}$
mirror mass	m	40 kg
arm length	L	4 km
sloshing mirror transmissivity	T_s	0.0008
output mirror transmissivity	T_o	0.017
end mirror transmissivity	T_e	2×10^{-5}
internal and RSE mirror transmissivity	T_i	0.005
optimal frequency	ω_opt	$2\pi \times 100$ Hz
sloshing frequency	Ω	$2\pi \times 170$ Hz
extraction rate (half-bandwidth)	δ	$2\pi \times 200$ Hz
SQL circulating power	W_circ^{SQL}	820 kW

The problem of the high circulating power W_circ, unfortunately, is not solved by the three-cavity design. This is actually a common characteristic of "external-readout" interferometer designs capable of beating the SQL. The reason for this high power is the energetic quantum limit (EQL), which was first derived for gravitational-wave interferometers by Braginsky, Gorodetsky, Khalili and Thorne [20]. The EQL arises from the phase-energy uncertainty principle

$$\Delta E \Delta\phi \geq \frac{\hbar\omega_0}{2}\,, \tag{3.32}$$

where E is the stored energy in the interferometer and ϕ is the phase of the light. The uncertainty ΔE of the stored light energy during the measurement process must be large enough to allow a small uncertainty $\Delta\phi$ in the stored light's optical phase, in which the GW signal is contained. For an interferometer with coherent light (so $\Delta E = \hbar\omega_0\sqrt{E/\hbar\omega_0}$), the EQL dictates that the energy stored in the arms must be larger than

$$E_\xi \sim \frac{mL^2\omega^2\Delta\omega}{4\omega_0\xi^2} \tag{3.33}$$

in order to beat the SQL by a factor of ξ near frequency ω with a bandwidth $\Delta\omega$ (Eq. (1) of Ref. [11] and Eq. (29) of Ref. [20]). In a broadband configuration with $\Delta\omega \sim \omega$, we have

$$E_\xi \sim \frac{mL^2\omega^3}{4\omega_0\xi^2}\,. \tag{3.34}$$

For comparison, in the broadband regime of the speed meter, we have, from Eq. (3.26),

$$\xi^2_\mathrm{min} = \frac{mL^2\delta(\omega_\mathrm{opt}^2 + \delta^2/4)}{4\,E\omega_0} \sim \frac{mL^2\omega_\mathrm{opt}^3}{4\,E\omega_0}\,, \tag{3.35}$$

where the stored energy is $E = 2W_\mathrm{circ}L/c$. Comparison between Eqs. (3.34) and (3.35) confirms

that our speed meter is EQL limited.

As a consequence of the EQL, designs with coherent light will all require a similarly high circulating power in order to achieve a similar sensitivity. Moreover, given the sharp dependence $E \propto \omega^3$, this circulating power problem will become much more severe when one wants to improve sensitivities at high frequencies.

Nevertheless, the EQL in the form (3.33) above only applies to coherent light. Using nonclassical light will enable the interferometer to circumvent it substantially. One possible method was invented by Braginsky, Gorodetsky, and Khalili [10] using a special optical topology and intracavity signal extraction. A more conventional solution for our external-readout interferometer is to inject squeezed light into the dark port, as we shall discuss in Sec. 3.5.1 (and as was also discussed in the original paper [20] on the EQL).

3.5 Squeezed Vacuum and FD Homodyne Dectection

In this section, we discuss two modifications to the three-cavity speed-meter design analyzed in Sec. 3.4.1. This discussion applies to both the simple and practical versions, shown in Figs. 3.2 and 3.3; the modifications are shown in Fig. 3.4. The first modification is to inject squeezed vacuum (with fixed squeeze angle) into the output port of the speed meter, as shown in Fig. 3.4. This will reduce the amount of power circulating in the interferometer. The second modification, also shown in Fig. 3.4, is the introduction of two filter cavities on the output, which allow us to perform *frequency-dependent* homodyne detection (described in KLMTV) that will dramatically improve the performance of the speed meter at frequencies $f \gtrsim f_{\rm opt}$.

3.5.1 Injection of Squeezed Vacuum into Dark Port

Because the amount of circulating power required by our speed meter remains uncomfortably large, it is desirable to reduce it by injecting squeezed vacuum into the dark port. The idea of using squeezed light in gravitational-wave interferometers was first conceived by Caves [14] and further developed by Unruh [4] and KLMTV. We shall start in this section with a straightforward scheme that will decrease the effective circulating power without otherwise changing the speed meter performance.

As discussed in Sec. IV B and Appendix A of KLMTV, a squeezed input state is related to the vacuum input state (assumed in Sec. 3.4.1) by a unitary squeeze operator $S(R,\lambda)$ [see Eqs. (41) and (A5) of KLMTV]

$$|\text{in}\rangle = S(R,\lambda)|0\rangle\,. \tag{3.36}$$

Here R is the squeeze amplitude and λ is the squeeze angle, both of which in principle can depend on sideband frequency. However, the squeezed light generated using nonlinear crystals [21, 22] has

frequency-independent R and λ in our frequency band of interest, i.e., $f < 10\,\mathrm{kHz}$ [23]; and in this section, we shall assume frequency independence.

The effect of input squeezing is most easily understood in terms of the following unitary transformation,

$$|\mathrm{in}\rangle \rightarrow S^\dagger(R,\lambda)|\mathrm{in}\rangle = |0\rangle \tag{3.37a}$$

$$\tilde{p}_j \rightarrow S^\dagger(R,\lambda)\tilde{p}_j S(R,\lambda)\,, \tag{3.37b}$$

$$\tilde{q}_j \rightarrow S^\dagger(R,\lambda)\tilde{q}_j S(R,\lambda)\,, \tag{3.37c}$$

where $j = 1, 2$. This brings the input state back to vacuum and transforms the input quadratures into linear combinations of themselves, in a rotate-squeeze-rotate way [Eq. (A8) of KLMTV, in matrix form]:

$$\begin{aligned}\begin{pmatrix}\tilde{p}_1\\ \tilde{p}_2\end{pmatrix} \rightarrow \begin{pmatrix}\tilde{p}_{1s}\\ \tilde{p}_{2s}\end{pmatrix} &= S^\dagger(R,\lambda)\begin{pmatrix}\tilde{p}_1\\ \tilde{p}_2\end{pmatrix} S(R,\lambda)\\ &= \begin{pmatrix}\cos\lambda & -\sin\lambda\\ \sin\lambda & \cos\lambda\end{pmatrix}\begin{pmatrix}e^{-R} & 0\\ 0 & e^{R}\end{pmatrix}\begin{pmatrix}\cos\lambda & \sin\lambda\\ -\sin\lambda & \cos\lambda\end{pmatrix}\begin{pmatrix}\tilde{p}_1\\ \tilde{p}_2\end{pmatrix}.\end{aligned} \tag{3.38}$$

In particular, the GW noise can be calculated by using the squeezed noise operator [Eq. (29) of KLMTV]

$$h_{ns} = S^\dagger(R,\lambda)h_n S(R,\lambda)\,, \tag{3.39}$$

and the vacuum state.

A special case—the case that we want—occurs when $R =$ constant and $\lambda = \pi/2$. Then there is no rotation between the quadratures but only a frequency-independent squeezing or stretching,

$$\tilde{p}_1 \rightarrow \tilde{p}_{1s} = e^R\tilde{p}_1\,, \tag{3.40a}$$

$$\tilde{p}_2 \rightarrow \tilde{p}_{2s} = e^{-R}\tilde{p}_2\,. \tag{3.40b}$$

Consequently, Eqs. (3.12) for the output quadratures $\tilde{q}_{1,2s} = S^\dagger(R,\pi/2)\tilde{q}_{1,2}S(R,\pi/2)$ are transformed into

$$\tilde{q}_{1s} = e^R\tilde{p}_1 e^{2i\psi} \tag{3.41a}$$

$$\tilde{q}_{2s} = e^{-R}\left[\left(\tilde{p}_2 - \kappa e^{2R}\tilde{p}_1\right)e^{2i\psi} + \sqrt{\kappa e^{2R}}\frac{\tilde{h}}{h_{SQL}}e^{i\psi}\right]. \tag{3.41b}$$

The corresponding noise can be put into the same form as Eq. (3.17),

$$h_{ns} = \frac{h_{SQL}}{\sqrt{\kappa_{\rm eff}}} e^{i\psi} \left[\tilde{p}_1(\cot\Phi_{\rm eff} - \kappa_{\rm eff}) + \tilde{p}_2\right] , \tag{3.42}$$

with

$$\cot\Phi_{\rm eff} \equiv e^{2R}\cot\Phi , \quad \kappa_{\rm eff} \equiv e^{2R}\kappa . \tag{3.43}$$

Since κ is proportional to the circulating power [see Eqs. (3.14)], gaining a factor e^{2R} in κ is equivalent to gaining this factor in $W_{\rm circ}$.

In other words, by injecting squeezed vacuum with squeeze factor e^{2R} and squeeze angle $\lambda = \pi/2$ into the interferometer's dark port, we can achieve precisely the same interferometer performance as in Sec. 3.4.1, but with a circulating light power that is lower by $W_{\rm circ,SISM} = e^{-2R} W_{\rm circ,OSM}$. (Here "SISM" means "squeezed-input speed meter" and "OSM" means "ordinary speed meter." Since squeeze factors $e^{-2R} \sim 0.1$ are likely to be available in the time frame of LIGO-III [7], this squeezed-input speed meter can function with $W_{\rm circ,SISM} \simeq 0.1 W_{\rm circ,OSM}$.

3.5.2 Frequency-Dependent Homodyne Detection

One can take further advantage of squeezed light by using frequency-dependent (FD) homodyne detection at the interferometer output [24–28]. As KLMTV have shown, FD homodyne detection can be achieved by sending the output light through one or more optical filters (as in Fig. 3.4) and then performing ordinary homodyne detection. If its implemention is feasible, FD homodyne detection will dramatically improve the speed meter's sensitivity at high frequencies (above $f_{\rm opt} = 100$ Hz). Note that the KLMTV design that used FD homodyne detection was called a "variational-output" interferometer; consequently, we shall use the term "variational-output speed meter" to refer to our speed meter with FD homodyne detection. Continuing the analogy, when we have both squeezed-input and FD homodyne detection, we will use the term "squeezed-variational speed meter." The following discussion is analogous to Secs. IV and V of KLMTV.

For a generic frequency-dependent[6] squeeze angle $\lambda(\omega)$ and homodyne detection phase $\Phi(\omega)$, we have, for the squeezed noise operator [Eqs. (3.39) and (3.38)],

$$\begin{aligned} h_{ns} \;=\; -\frac{h_{SQL}}{\sqrt{\kappa}} e^{i\psi} \sqrt{1+\tilde{\kappa}^2} \Big(& \tilde{p}_1 \left\{ \cosh R \cos\tilde{\Psi} - \sinh R \cos\left[\tilde{\Psi} - 2(\tilde{\Psi}+\lambda)\right] \right\} \\ & -\tilde{p}_2 \left\{ \cosh R \sin\tilde{\Psi} - \sinh R \sin\left[\tilde{\Psi} - 2(\tilde{\Psi}+\lambda)\right] \right\} \Big) , \end{aligned} \tag{3.44}$$

where

$$\cot\tilde{\Psi} \equiv \tilde{\kappa} \equiv \kappa - \cot\Phi . \tag{3.45}$$

[6] For generality of the equations, we allow the squeeze angle and the the homodyne phase both to be frequency dependent, but the squeeze angle will be fixed (frequency independent) later in the argument [specifically, in Eq. (3.48)].

The corresponding noise spectral density [computed by using the ordinary vacuum spectral densities, $S_{\bar{p}_1} = S_{\bar{p}_2} = 1$ and $S_{\bar{p}_1\bar{p}_2} = 0$, in Eq. (3.44)] is

$$S_h = \frac{(h_{SQL})^2}{\kappa}(1+\tilde{\kappa}^2)\left\{e^{-2R} + \sinh 2R[1 - \cos 2(\tilde{\Psi}+\lambda)]\right\}. \tag{3.46}$$

Note that these expressions are analogous to KLMTV Eqs. (69)–(71) for a squeezed-variational interferometer (but the frequency dependence of their $\mathcal{K}$ is different from that for our κ). From Eq. (3.46), S_h can be no smaller than the case when

$$\tilde{\kappa} = 0\,, \quad \cos 2(\tilde{\Psi}+\lambda) = 1\,. \tag{3.47}$$

The optimization conditions (3.47) are satisfied when

$$\cot\Phi = \kappa\,, \quad \lambda = \pi/2\,, \tag{3.48}$$

which corresponds to frequency-dependent homodyne detection on the (frequency-independent) squeezed-input speed meter discussed in the previous section.

As it turns out, the condition $\cot\Phi = \kappa$ can readily be achieved by the family of two-cavity optical filters invented by KLMTV and discussed in their Sec. V and Appendix C. We summarize and generalize their main results in our Appendix A. The two filter cavities are both Fabry-Perot cavities with (ideally) only one transmitting mirror. They are characterized by their bandwidths, δ_J, (where $J = \mathrm{I}, \mathrm{II}$ denote the two cavities) and by their resonant frequencies, $\omega_0 + \xi_J\delta_J$ (the ones nearest ω_0). The output light from the squeezed-input speed meter is sent through the two filters, and then a homodyne detection with frequency-independent phase θ is performed on it.

For the squeezed-variational speed meter (shown in Fig. 3.4) with the parameters in Table 3.1, plus $\xi^2_{\min} = 0.1$, $\delta = 2\omega_{\rm opt}$, $\Lambda^4 = 4\,\omega^4_{\rm opt}$, and $e^{-2R} = 0.1$, we have

$$\kappa = \frac{4\,\omega^4_{\rm opt}}{(\omega^2 - \omega^2_{\rm opt})^2 + 8\,\omega^4_{\rm opt}} \tag{3.49}$$

and the required filter and detection configuration is $\xi_{\rm I} = 1.7355$, $\delta_{\rm I} = 2\pi \times 91.57\,\mathrm{Hz}$, $\xi_{\rm II} = -1.1133$, $\delta_{\rm II} = 2\pi \times 114.3\,\mathrm{Hz}$, and $\theta = \pi/2$. [These values are reached by solving Eqs. (C4) of KLMTV, or by using the simpler method described in Appendix A of this paper.] The resulting performance is plotted in Fig. 3.10. Note the substantial improvement at $\omega \gtrsim \omega_{\rm opt}$.

In the case of position-meter interferometers with optical filters (the interferometers analyzed by KLMTV), the optical losses due to the filter cavities contribute significantly to the noise spectral density and drastically reduce the ability to beat the SQL. It turns out that the squeezed-variational speed meter is less sensitive to such losses, as we shall see in Sec. 3.6.

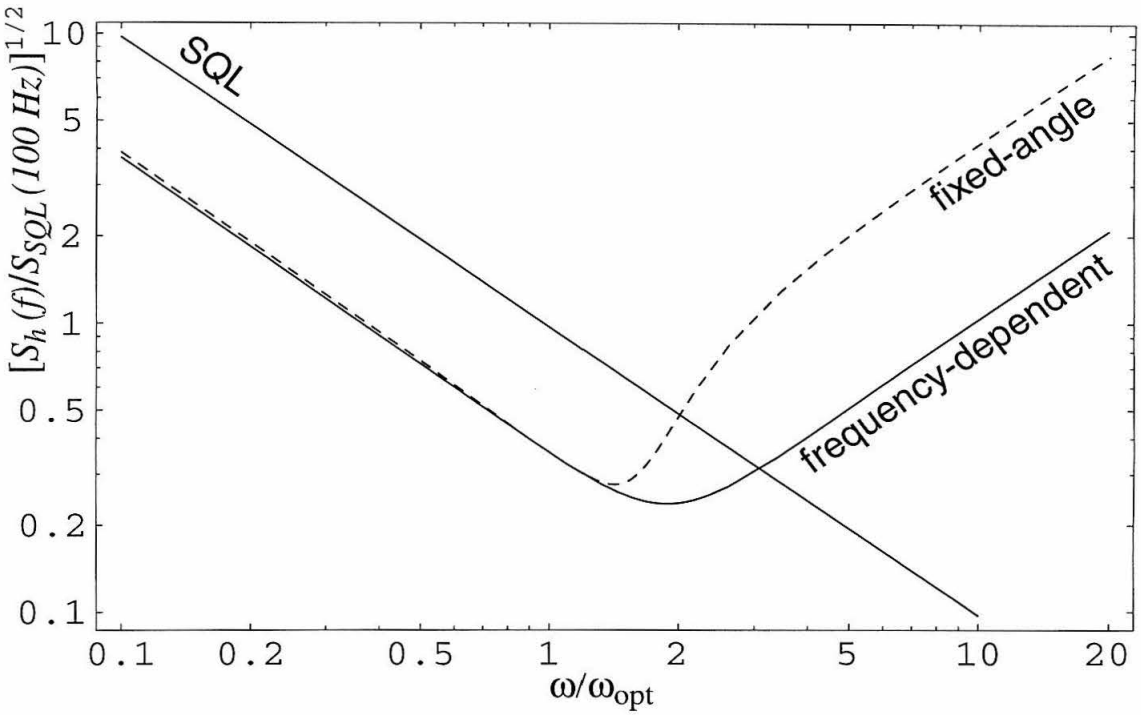

Figure 3.10: Comparison of typical noise curves for frequency-dependent and fixed-angle homodyne detection. The FD homodyne angle $\Phi(\omega)$ is that of Eqs. (3.48) and (3.49); the fixed homodyne angle Φ is that of Eq. (3.43); the circulating power is e^{-2R} times that of Table 3.1; and all other parameters are identical for the two interferometers and are given in Table 3.1.

3.6 Optical Losses

In order to understand the issue of optical losses in this speed meter, we shall start by addressing its *internal* losses. These include scattering and absorption at each optical element, finite transmissivities of the end mirrors, and imperfections of the mode-matching between cavities. The effect of *external* losses (i.e., losses in the detection system and any filter cavities) will be discussed separately. Note that the analysis in this section includes the internal and RSE mirrors, so it applies primarily to the speed meter designs in Figs. 3.3 and 3.4.

3.6.1 Internal losses

In this subsection, we will consider only noise resulting from losses associated with optical elements inside the interferometer. These occur

- in the optical elements: arm cavities, sloshing cavity, extraction mirror, port-closing mirror, beam splitter, RSE mirror;

- due to mode-mismatching[7]; and
- due to the imperfect matching of the transmissivities of the RSE and internal mirrors[8].

Since the optical losses will dominate, we focus only on that type of loss here. The loss at each optical element will decrease the amplitude of the sideband light (which carries the gravitational-wave information) and will simultaneously introduce additional vacuum fluctuations into the optical train. Schematically, for some sideband $\tilde{a}(\omega)$, the loss is described by

$$\tilde{a}(\omega) \to \sqrt{1-\mathcal{E}(\omega)}\,\tilde{a}(\omega) + \sqrt{\mathcal{E}(\omega)}\,\tilde{n}(\omega)\,, \tag{3.50}$$

where $\mathcal{E}$ is the (power) loss coefficient, and $\tilde{n}(\omega)$ is the vacuum field entering the optical train at the loss point.

It should be noted that there are various methods of grouping these losses together in order to simplify calculations. For example, we combine all of the losses occurring in the arm (or sloshing) cavities, into one loss coefficient of $\mathcal{L} \sim 20 \times 10^{-6}$ [according to KLMTV Eq. (93)]. Then we assume that the end mirrors have transmissivity $T_{\rm e} = 2 \times 10^{-5}$, thereby absorbing all of the arm losses into one term [see KLMTV Eq. (B5) and preceding discussion].

Assuming that the noise entering at the end mirrors of the arm cavities is denoted $\tilde{n}_{e1,2}$ and $\tilde{n}_{n1,2}$ for the east and north arms respectively, at the end mirror of the sloshing cavity $\tilde{s}_{1,2}$, at the port-closing mirror $\tilde{w}_{1,2}$, and at the RSE mirror $\tilde{m}_{n1,2}$ and $\tilde{m}_{s1,2}$ [representing the losses described in the previous paragraph; see Appendix B.3 for details], the output of the lossy three-cavity speed-meter system (Fig. 3.3; the simplified and practical versions are no longer equivalent, since there will be additional losses due to the presence of the internal and RSE mirrors) is

$$\begin{aligned}
\tilde{q}_1 \;=\; & -\frac{\mathcal{L}^*(\omega)}{\mathcal{L}(\omega)}\tilde{p}_1 + \frac{i\omega\sqrt{\delta\delta_{\rm e}}}{\mathcal{L}(\omega)}(\tilde{n}_{e1} - \tilde{n}_{n1}) + \frac{\Omega\sqrt{2\delta\delta_{\rm e}}}{\mathcal{L}(\omega)}\tilde{s}_1 - \frac{\sqrt{T_{\rm e}}(\Omega^2 - \omega^2 + i\omega\delta_{\rm s})}{\mathcal{L}(\omega)}\tilde{w}_1 \\
& - \frac{i\omega\sqrt{2\delta\delta_\epsilon}}{\mathcal{L}(\omega)}\tilde{m}_{s1} + \frac{\omega\sqrt{2L\delta\delta_\epsilon}(\omega - i\delta_{\rm i})}{\sqrt{c\delta_{\rm i}}\mathcal{L}(\omega)}\tilde{m}_{n1}\,, \qquad (3.51a) \\
\tilde{q}_2 \;=\; & \frac{2i\omega\sqrt{\omega_0 T_{\rm o} W^*_{\rm circ}}}{L\sqrt{\hbar}\mathcal{L}(\omega)}\tilde{x} - \frac{\mathcal{L}^*(\omega)}{\mathcal{L}(\omega)}\tilde{p}_2 + \frac{\Omega\sqrt{2\delta\delta_{\rm e}}}{\mathcal{L}(\omega)}\tilde{s}_2 + \frac{i\omega\sqrt{\delta\delta_{\rm e}}}{\mathcal{L}(\omega)}(\tilde{n}_{e2} - \tilde{n}_{n2}) \\
& - \frac{\sqrt{T_{\rm e}}(\Omega^2 - \omega^2 + i\omega\delta_{\rm s})}{\mathcal{L}(\omega)}\tilde{w}_2 - \frac{i\omega\sqrt{2\delta\delta_\epsilon}}{\mathcal{L}(\omega)}\tilde{m}_{s2} + \frac{\omega\sqrt{2L\delta\delta_\epsilon}(\omega - i\delta_{\rm i})}{\sqrt{c\delta_{\rm i}}\mathcal{L}(\omega)}\tilde{m}_{n2}\,, \qquad (3.51b)
\end{aligned}$$

[7] According to our simple analysis in Appendix C, this effect will be insignificant in comparison with the losses in the optical elements, so we shall ignore it.

[8] This effect is negligibly small so we shall ignore it; see Appendix D for details.

where

$$\tilde{x} = L\tilde{h} - \frac{4\sqrt{2\hbar\omega_0 W^*_{\rm circ}}}{mc\omega^2\mathcal{L}(\omega)}\left[\frac{i\omega\sqrt{2c\delta}}{\sqrt{L}}\tilde{p}_1 + \frac{i\omega\sqrt{c\delta_\epsilon}}{\sqrt{L}}\tilde{m}_{s1} - \frac{\sqrt{\delta_\epsilon}[\Omega^2 - i\omega(\delta+\delta_{\rm i})]}{\sqrt{\delta_{\rm i}}}\tilde{m}_{n1}\right.$$
$$\left. - \frac{\Omega\sqrt{c\delta_{\rm e}}}{\sqrt{L}}\tilde{s}_1 + i\omega\sqrt{\delta\delta_{\rm e}}\tilde{w}_1 - \frac{i\omega\sqrt{c\delta_{\rm e}}}{\sqrt{2L}}(\tilde{n}_{e1} - \tilde{n}_{n1})\right] \tag{3.52}$$

with

$$\begin{aligned} \delta_{\rm e} &= cT_{\rm e}/2L\,, \quad \delta_{\rm s} = cT_{\rm s}/2L\,, \\ \delta_{\rm i} &= cT_{\rm i}/4L\,, \quad \delta_\epsilon = c\mathcal{E}/2L\,. \end{aligned} \tag{3.53}$$

Note that the expression for the circulating power now has the form

$$W^*_{\rm circ} = \frac{1}{2}\hbar\omega_0 B_1^2 = \frac{4\hbar\omega_0 T_{\rm i}T_{\rm p}I_1^2}{(T_{\rm i}T_{\rm p} + 4T_{\rm e})^2} \tag{3.54}$$

[cf. Eq. (3.10)].

Equations (3.51) are approximate expressions [accurate to about 6%, as were Eqs. (3.8); see Footnote 5], where the assumptions (3.7) regarding the relative sizes of the transmissivities were used to simplify from the exact expressions. Alternatively, they can be derived analytically by keeping the leading order of the small quantities $\omega L/c \sim \sqrt{T_{\rm s}} \sim T_{\rm o} \sim T_{\rm i}$, plus the various loss factors; see Sec. VI of KLMTV and Sec. 2.5 of this thesis for details of the derivations for other inteferometer designs. In addition to confirming the approximate formulas, such a derivation can also clarify the origins of various noise terms and their connections to one another.

3.6.2 Internal and External Losses in Compact Form

In order to simplify the above Eqs. (3.51) and (3.52), we define κ^* in identically the same way as we defined κ [Eq. (3.14) or (3.22)] but with $W_{\rm circ} \to W^*_{\rm circ}$. Let $\mathcal{E}^{\rm S}_{\mathcal{N}}$ and $\mathcal{E}^{\rm R}_{\mathcal{N}}$ represent the shot and radiation-pressure noises for the various parts of the interferometer, specified by $\mathcal{N}$. In Table 3.2, expressions for $\mathcal{E}^{\rm S}_{\mathcal{N}}$ and $\mathcal{E}^{\rm R}_{\mathcal{N}}$ are given for $\mathcal{N}$ = AES (arm cavities, extraction mirror, and sloshing cavity combined), close (port-closing mirror), $\rm RSE_{in}$ (RSE cavity in the north direction, or going "in" to the arms), and $\rm RSE_{out}$ (RSE cavity in the south direction, or going "out" of the arms). The various $\varepsilon_{\mathcal{N}}$ represent the characteristic (and frequency-independent) fractional losses for each of these terms; values are given in Table 3.3. Note that, by definition, $\mathcal{E}^{\rm S}_{\mathcal{N}}$ are required to be real, while $\mathcal{E}^{\rm R}_{\mathcal{N}}$ may have imaginary parts. For more information, including physical explanations of each of these terms, see Appendix B.

It is simple at this point to include the losses associated with optical elements external to the

Table 3.2: Loss factors $\mathcal{E}^{\mathrm{S}}_{\mathcal{N}}$ due to shot noise and $\mathcal{E}^{\mathrm{R}}_{\mathcal{N}}$ due to radiation pressure for each type of loss source in the interferometer.

Source	$\mathcal{N}$	$\mathcal{E}^{\mathrm{S}}_{\mathcal{N}}$ (shot noise)	$\mathcal{E}^{\mathrm{R}}_{\mathcal{N}}$ (radiation pressure noise)
arm cavities, extract. mirror, sloshing cavity	AES	$\sqrt{\frac{\varepsilon_{\mathrm{AES}}}{T_{\mathrm{o}}}}\frac{\omega\delta}{\lvert\mathcal{L}(\omega)\rvert}$	$-\frac{e^{i\psi}}{2}\sqrt{\frac{\varepsilon_{\mathrm{AES}}}{T_{\mathrm{o}}}}$
port-closing mirror	close	$\sqrt{\varepsilon_{\mathrm{close}}}\frac{\Omega^2-\omega^2}{\lvert\mathcal{L}(\omega)\rvert}$	$-\frac{ie^{i\psi}}{2}\sqrt{\varepsilon_{\mathrm{close}}}$
RSE cavity "in" to arms	$\mathrm{RSE_{in}}$	$\sqrt{\frac{\varepsilon_{\mathrm{RSE}}T_{\mathrm{i}}}{4T_{\mathrm{o}}}\left(1+\frac{\omega^2}{\delta_{\mathrm{i}}^2}\right)}\frac{\omega\delta}{\lvert\mathcal{L}(\omega)\rvert}$	$e^{i\psi-i\beta_{\mathrm{i}}}\sqrt{\frac{\varepsilon_{\mathrm{RSE}}T_{\mathrm{o}}}{T_{\mathrm{i}}}}\frac{\omega(\delta_{\mathrm{i}}+\delta)+i\Omega^2}{\omega\delta}$
RSE cavity "out" to slosh	$\mathrm{RSE_{out}}$	$\sqrt{\frac{\varepsilon_{\mathrm{RSE}}T_{\mathrm{i}}}{4T_{\mathrm{o}}}\left(1+\frac{\omega^2}{\delta_{\mathrm{i}}^2}\right)}\frac{\omega\delta}{\lvert\mathcal{L}(\omega)\rvert}$	$e^{i\psi+i\beta_{\mathrm{i}}}\sqrt{\frac{\varepsilon_{\mathrm{RSE}}T_{\mathrm{o}}}{T_{\mathrm{i}}}}\frac{\omega(\delta_{\mathrm{i}}-\delta)-i\Omega^2}{\omega\delta}$
local oscillator, photodiode, and circulator	OPC	$\sqrt{\varepsilon_{\mathrm{OPC}}}$	0
filter cavities	F	$\sqrt{\varepsilon_{\mathrm{F}}}$	0

interferometer. These include losses are associated with

- the local oscillator used for homodyne detection,
- the inefficiency of the photodiode,
- the circulator by which the squeezed vacuum is injected, and
- the external filter cavities used for the variational-output scheme.

These can be addressed in the same manner as the losses inside the speed meter. We need only include two more terms in the summation, $\mathcal{N} = \mathrm{OPC}$ for the local oscillator, photodiode, and circulator and $\mathcal{N} = \mathrm{F}$ for the filters. Again, these terms are shown in Tables 3.2 and 3.3 and described in more detail in Appendix B.

Using these $\mathcal{E}^{\mathrm{S}}_{\mathcal{N}}$ and $\mathcal{E}^{\mathrm{R}}_{\mathcal{N}}$, we can rewrite the input-output relation (3.51) in the same form as Eq. (3.12) as follows:

$$\begin{pmatrix} \tilde{q}_1 \\ \tilde{q}_2 \end{pmatrix} = e^{2i\psi}\begin{pmatrix} 1 & 0 \\ -\kappa^* & 1 \end{pmatrix}\begin{pmatrix} \tilde{p}_1 \\ \tilde{p}_2 \end{pmatrix} + \sum_{\mathcal{N}} e^{2i\alpha_{\mathcal{N}}}\begin{pmatrix} \mathcal{E}^{S}_{\mathcal{N}} & 0 \\ -\kappa^*\mathcal{E}^{\mathrm{R}}_{\mathcal{N}} & \mathcal{E}^{S}_{\mathcal{N}} \end{pmatrix}\begin{pmatrix} n_{\mathcal{N}1} \\ n_{\mathcal{N}2} \end{pmatrix} + \sqrt{2\kappa^*}\frac{h}{h_{SQL}}e^{i\psi}\begin{pmatrix} 0 \\ 1 \end{pmatrix}, \tag{3.55}$$

where the $\alpha_{\mathcal{N}}$ are uninteresting phases that do not affect the noise.

Table 3.3: Fiducial values for the fractional losses occuring in various parts of the interferometer. These losses and their values are discussed in more detail in Appendix B.

Loss source	Symbol	Value
arm cavity	$\varepsilon_{\mathrm{arm}}$	2×10^{-5}
sloshing cavity	$\varepsilon_{\mathrm{slosh}}$	2×10^{-5}
extraction mirror	$\varepsilon_{\mathrm{ext}}$	2×10^{-5}
RSE cavity	$\varepsilon_{\mathrm{RSE}}$	2×10^{-5}
port-closing mirror	$\varepsilon_{\mathrm{close}}$	2×10^{-5}
local oscillator	$\varepsilon_{\mathrm{lo}}$	0.001
photodiode	$\varepsilon_{\mathrm{pd}}$	0.001
circulator	$\varepsilon_{\mathrm{circ}}$	0.001
mode-mismatch into filters	$\varepsilon_{\mathrm{mm}}$	0.001
Combined loss source terms		
arms, extraction mirror, and sloshing cavity[a]	$\varepsilon_{\mathrm{AES}}$	6×10^{-5}
local oscillator, photodiode, and circulator	$\varepsilon_{\mathrm{OPC}}$	0.003
filter cavities (with mode mismatch)	ε_{F}	0.005

[a]This loss does have some weak frequency dependence, shown in Eq. (B.8), which will cause it to increase slightly at very low frequencies.

The relative magnitudes of the loss terms are shown in Fig. 3.11. From the plot, we can see that there are several loss terms—specifically, the shot noise from the AES, OPC, and filter cavities (if any)—that are of comparable magnitude at high frequencies and dominate there. The AES radiation-pressure term dominates at low frequencies, and the RSE radiation-pressure terms are also significant. Since the largest noise sources at low frequencies are radiation-pressure terms, they will be dependent on the circulating power. Consequently, those terms will become smaller when the circulating power is reduced, as when squeezed vacuum is injected into the dark port. This will be demonstrated in Fig. 3.12 below.

To compute the spectral noise density, we suppose the output at homodyne angle Φ is measured, giving

$$S_{h_n}(\omega) = \frac{(h_{SQL})^2}{2\kappa^*} \left\{ \left[(\cot\Phi - \kappa^*)^2 + 1 \right] + \sum_{\mathcal{N}} \left[|\mathcal{E}^{\mathrm{S}}_{\mathcal{N}} \cot\Phi - \mathcal{E}^{\mathrm{R}}_{\mathcal{N}} \kappa^*|^2 + (\mathcal{E}^{\mathrm{S}}_{\mathcal{N}})^2 \right] \right\}, \tag{3.56}$$

where we have assumed all of the vacuum fluctuation spectral densities are unity and the cross-correlations are zero; this is the same technique that we used to derive Eqs. (3.18) and (3.46) and that was used in Chapter 2 and KLMTV. Given the complicated behaviors of $\mathcal{E}^{\mathrm{S}}_{\mathcal{N}}$ and $\mathcal{E}^{\mathrm{R}}_{\mathcal{N}}$, including these loss terms in the optimization of the homodyne phase $\Phi(\omega)$ is unlikely to be helpful. Therefore, we will use $\cot\Phi = \kappa^*_{\mathrm{max}}$, as in the lossless case. This gives us a total noise with losses:

$$S_{h_n}(\omega) = \frac{(h_{SQL})^2}{2\kappa^*} \left\{ \left[(\kappa^*_{\mathrm{max}} - \kappa^*)^2 + 1 \right] + \sum_{\mathcal{N}} \left[|\mathcal{E}^{\mathrm{S}}_{\mathcal{N}} \kappa^*_{\mathrm{max}} - \mathcal{E}^{\mathrm{R}}_{\mathcal{N}} \kappa^*|^2 + (\mathcal{E}^{\mathrm{S}}_{\mathcal{N}})^2 \right] \right\}. \tag{3.57}$$

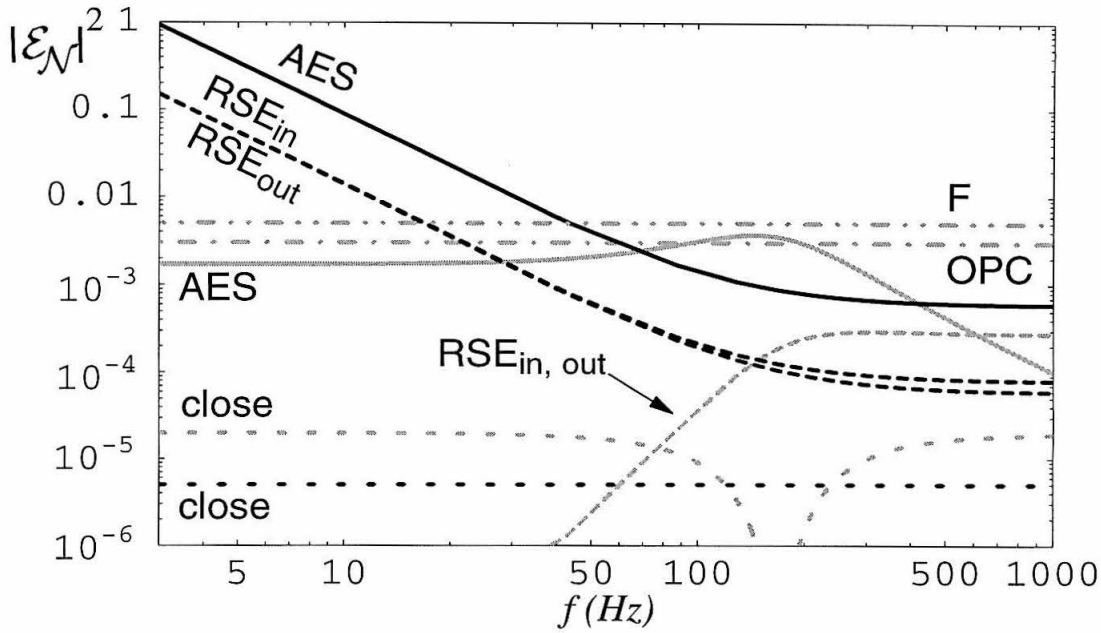

Figure 3.11: Moduli-squared of the loss factors shown in Table 3.2. In general, the black curves are the radiation-pressure noise and the gray curves are the shot noise. The parameters used for this plot are given in Tables 3.1 and 3.3.

When we inject squeezed vacuum into the dark port, we get output operators

$$\begin{pmatrix} \tilde{q}_{1s} \\ \tilde{q}_{2s} \end{pmatrix} = e^{2i\psi} \begin{pmatrix} 1 & 0 \\ -\kappa^* & 1 \end{pmatrix} \begin{pmatrix} e^{R}\tilde{p}_1 \\ e^{-R}\tilde{p}_2 \end{pmatrix} + \sum_{\mathcal{N}} e^{2i\alpha_{\mathcal{N}}} \begin{pmatrix} \mathcal{E}^S_{\mathcal{N}} & 0 \\ -\kappa^* \mathcal{E}^R_{\mathcal{N}} & \mathcal{E}^S_{\mathcal{N}} \end{pmatrix} \begin{pmatrix} n_{\mathcal{N}1} \\ n_{\mathcal{N}2} \end{pmatrix} + \sqrt{2\kappa^*} \frac{h}{h_{SQL}} e^{i\psi} \begin{pmatrix} 0 \\ 1 \end{pmatrix} \tag{3.58}$$

that can be regarded as acting on the ordinary vacuum states of the input. Once again assuming that the vacuum fluctuation spectral densities are unity and the cross-correlations are zero, the squeezed-input noise spectral density with homodyne detection at phase Φ is

$$S_{h_{ns}}(\omega) = \frac{(h_{SQL})^2}{2\kappa^*} \left\{ \left[(\cot\Phi - \kappa^*)^2 e^{2R} + e^{-2R} \right] + \sum_{\mathcal{N}} \left[|\mathcal{E}^{\rm S}_{\mathcal{N}} \cot\Phi - \mathcal{E}^{\rm R}_{\mathcal{N}} \kappa^*|^2 + (\mathcal{E}^{\rm S}_{\mathcal{N}})^2 \right] \right\} . \tag{3.59}$$

3.6.3 Performance of Lossy Speed Meters and Comparisons with Other Configurations

Examples of lossy speed meter noise curves with and without squeezed vacuum [Eqs. (3.57) and (3.59)] are shown in Fig. 3.12. Note that, as mentioned before, the losses are less significant when

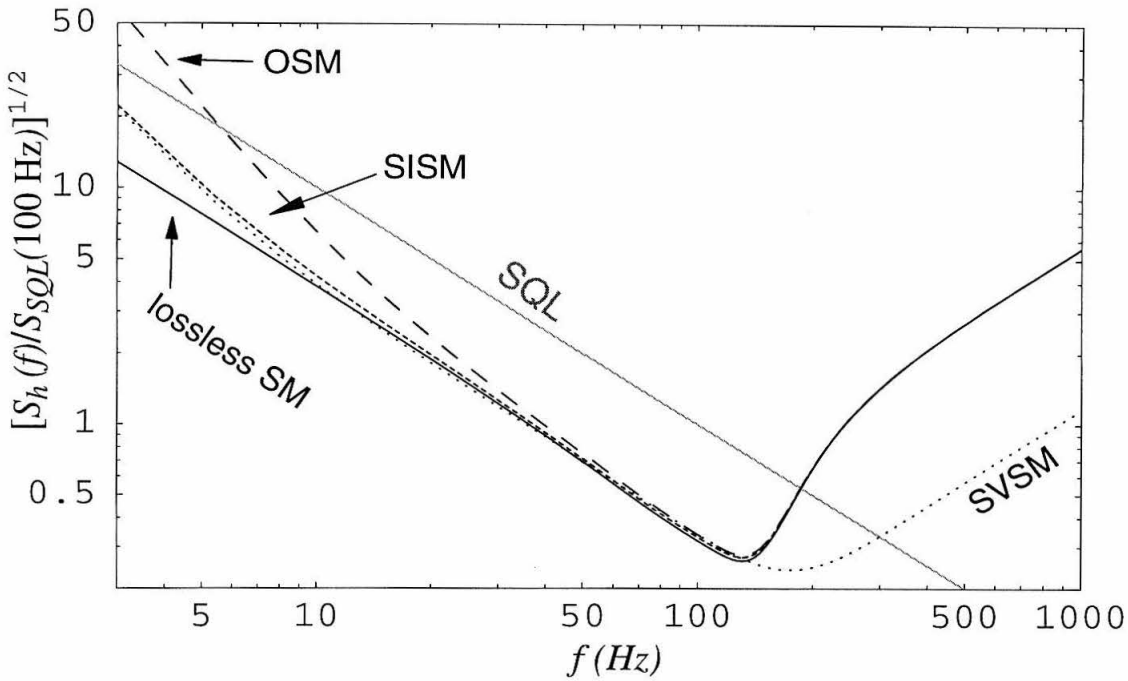

Figure 3.12: Noise curves showing the effects of losses. Noise curves for lossy versions of the ordinary (OSM), squeezed-input (SISM), and squeezed-variational (SVSM) speed meters are shown, along with a curve of the lossless ordinary speed meter for comparison. All speed meter curves here have the same parameters: $\delta = 2\omega_{\rm opt}$, $\Omega = \sqrt{3}\omega_{\rm opt}$, $\omega_{\rm opt} = 2\pi \times 100$ Hz, and $T_{\rm i} = 0.005$. The rest of the parameters are given in Tables 3.1 and 3.3.

squeezed vacuum is used to reduce the circulating power, since the radiation-pressure noise coming from the losses is reduced. In the ordinary speed meter (no squeezed vacuum), the losses increase $\sqrt{S_{h_n}}$ by $5-9\%$ in the band $50-105$ Hz. The losses have little effect above this range, but below it, noise increases significantly, mostly due to the radiation-pressure noises shown in Fig. 3.11. For the squeezed-input speed meter (power squeeze-factor $e^{-2R} = 0.1$), the losses increase $\sqrt{S_{h_n}}$ by $3-4\%$ in the band $25-150$ Hz. Again, the losses have little effect above this range. At low frequencies, however, the losses get quite large: 11% at 10 Hz, 32% at 5 Hz, and 73% at 3 Hz. Losses in the squeezed-variational speed meter are much the same as in the squeezed-input speed meter. The slight difference at low frequencies is due to the fact that the lossless squeezed-variational speed meter is slightly better in that regime than the ordinary or squeezed-input speed meter.

The noise curves of squeezed-input speed meters (with ordinary homodyne detection) compared with the SQL are shown in Fig. 3.13, along with the noise of a conventional position meter with the same optical power. These speed meters beat the SQL in a broad frequency band, despite the losses. In particular, the noise curve for the speed meter with $W_{\rm circ} = 800\,\mathrm{kW}$ (and $f_{\rm opt} = 107\,\mathrm{Hz}$) matches the curve of the conventional position meter at high frequencies, while it beats the SQL

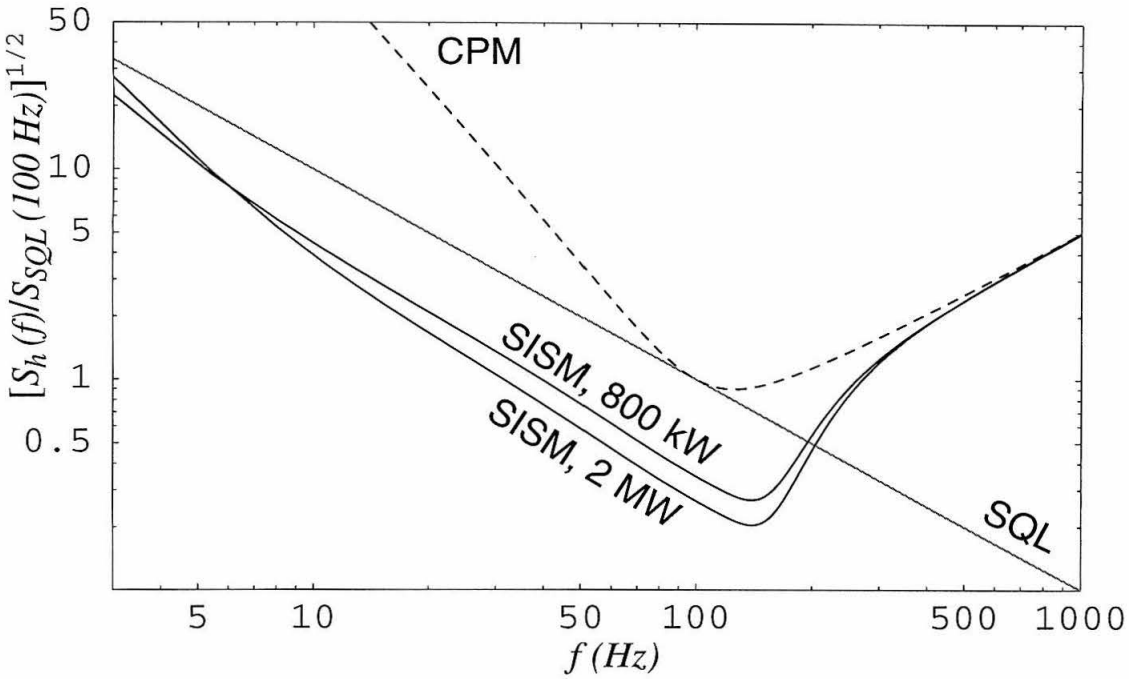

Figure 3.13: Comparison of noise curves of a conventional position meter (CPM) and squeezed-input speed meters (SISM) with circulating powers $W_{\rm circ} = 820$ kW and $W_{\rm circ} = 2$ MW. The speed meters have $f_{\rm opt} = 107$ Hz, with Ω and δ determined by Eq. (3.29). Other parameters used are those in Tables 3.1 and 3.3 with $T_{\rm i} = 0.005$ and $e^{-2R} = 0.1$.

by a factor of ~ 8 (in power) below ~ 150 Hz. In terms of the signal-to-noise ratio for neutron star binaries, for example, this configuration improves upon the conventional design by a factor of 3.6 in signal-to-noise ratio, which corresponds to a factor of 43 increase in event rate. If it is possible to have a higher circulating power, say $W_{\rm circ} = 2$ MW, the squeezed-input speed meter would be able to beat the SQL by a factor of ~ 14, corresponding to a factor of 4.6 in signal-to-noise and 97 in event rate. (Such a noise curve is shown in Fig. 3.13).

The broadband behaviors of the speed meters with losses are particularly interesting. We start by looking at the expression for the noise spectral density, Eq. (3.59). An ideal (lossless) speed meter in the broadband configuration beats the SQL from 0 Hz up to $\omega \sim \omega_{\rm opt}$, by roughly a constant factor, because κ is roughly constant in this band. *This is the essential feature of the speed meter*; see Sec. 3.4. Focusing on this region, we have, approximately (for squeezed-input speed meters that are lossy):

$$S_{h_{ns}}(\omega) \approx \frac{h_{SQL}^2}{2\kappa_{\rm max}^*}\left[e^{-2R} + \sum_{\mathcal{N}} |\mathcal{E}_{\mathcal{N}}^S|^2 + \kappa_{\rm max}^{*2} \sum_{\mathcal{N}} |\mathcal{E}_{\mathcal{N}}^{\rm S} - \mathcal{E}_{\mathcal{N}}^{\rm R}|^2\right] . \tag{3.60}$$

Qualitatively, we can see that if the losses are not severe or if $\kappa_{\rm max}^*$ is relatively small (such that the later two terms in the above equation are small compared to the power squeeze factor e^{-2R}), the

losses do not contribute significantly to the total noise. If, in addition, the dominant loss factors are (almost) frequency independent, then the noise due to losses gives a rather constant contribution, as shown by curves in Fig. 3.12. In particular, the large bandwidth is preserved. (There is a slight exception to this statement in the absence of squeezed input. Without squeezed input, the circulating power is higher, causing $\kappa^*_{\rm max}$ to be 10 times larger than the other cases. Consequently, the frequency dependence of $\mathcal{E}^{\rm R}_{\rm AES}$ to appear in the output.)

As $\kappa_{\rm max}$ increases, the noise from the losses may become dominant. In fact, when one minimizes the noise spectral density with respect to $\kappa^*_{\rm max}$, one obtains the following loss-dominated result:

$$S_h^{\rm L}(\omega) \approx h_{SQL}^2 \sqrt{\left(\sum_{\mathcal{N}} |\mathcal{E}^{\rm S}_{\mathcal{N}} - \mathcal{E}^{\rm R}_{\mathcal{N}}|^2\right)\left(e^{-2R} + \sum_{\mathcal{N}} |\mathcal{E}^{\rm S}_{\mathcal{N}}|^2\right)}, \tag{3.61}$$

which is achieved if and only if

$$\kappa^*_{\rm max} = \kappa^{\rm L} \equiv \sqrt{\frac{e^{-2R} + \sum_{\mathcal{N}} |\mathcal{E}^{\rm S}_{\mathcal{N}}|^2}{\sum_{\mathcal{N}} |\mathcal{E}^{\rm S}_{\mathcal{N}} - \mathcal{E}^{\rm R}_{\mathcal{N}}|^2}}\,. \tag{3.62}$$

This $\kappa^{\rm L}$ is rather constant and is comparable in magnitude to the values of $\kappa^*(\omega)$ of our speed meters, suggesting that the speed meters can become loss-limited over a broad band of frequencies. Contrast this with the KLMTV position meters, where $\mathcal{K}_*(\omega)$ grows as ω^{-2} at low frequencies; see Fig. 3.14. *This is a fundmental property of displacement meters.* As a result, a position meter optimized at some frequency $f_{\rm opt}$ may be able to reach its "loss limit" (the equivalent of $S_h^{\rm L}$) at that frequency $f_{\rm opt}$, but doing so will result in a sharp growth of noise at freqencies below $f_{\rm opt}$. In contrast, a speed meter similarly optimized is able to stay at the noise level of its loss limit $S_h^{\rm L}$ over a wide band of frequencies below $f_{\rm opt}$; see Fig. 3.15. While it is unfortunate that losses limit the performance of interferometers, the speed meter is at least able to retain a wide-band sensitivity even in the presence of a loss-limit.

To give a specific example of this loss-limit phenomenon, we first notice that, with the same circulating power, the conventional position-meter $\mathcal{K}_*$ and our (squeezed-variational) speed-meter κ agree[9] if $\delta = \gamma$ (where γ is the bandwidth of the arm cavities, as defined in KLMTV) and if we consider high frequencies ($\omega \gtrsim \{\gamma, \Omega\}$). Figure 3.14 shows an example of this [with $W_{\rm circ} = 820\,{\rm kW}$, $\gamma = \delta = 2\pi \times 100\,{\rm Hz}$, $\Omega = 2\pi \times 173\,{\rm Hz}$]. The noise curves of the two interferometers are shown in Fig. 3.15.

As expected, the two noise curves in Fig. 3.15 agree at very high frequencies. At intermediate frequencies, the speed meter's κ^* is larger than the position meter's $\mathcal{K}_*$, and thus the speed meter has better sensitivity than the position meter. As the frequency decreases, the speed meter reaches its loss limit first and stays at that limit for a wide range of frequencies. The position meter, however,

[9] In fact, $\mathcal{K}_*$ can be obtained from the speed meter κ^* by putting $\Omega \to 0$ and $\delta \to \gamma$.

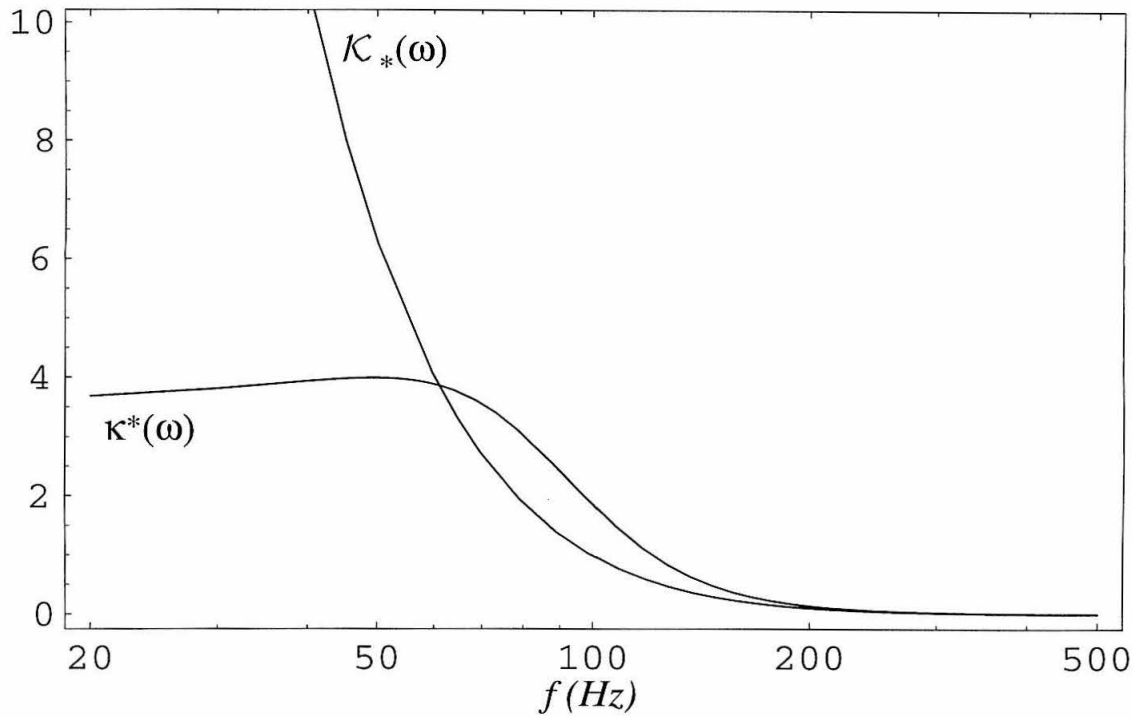

Figure 3.14: Comparison of the squeezed-variational speed meter's κ^* with the equivalent coupling constant $\mathcal{K}_*$ (as defined by KLMTV) for the squeezed-variational position meter. Parameters are $W_{\rm circ} = 820\,{\rm kW}$, $\gamma = \delta = 2\pi \times 100\,{\rm Hz}$, $\Omega = 2\pi \times 173\,{\rm Hz}$.

only touches its loss limit and then increases rapidly.

3.7 Conclusions

We have described and analyzed a speed-meter interferometer that has the same performance as the two-cavity design analyzed in Chapter 2, but it does so without the substantial amount of power flowing through the system or the exorbitantly high input laser power required by the two-cavity speed meter. It was also shown that the injection of squeezed vacuum with $e^{-2R} = 0.1$ into the dark port of the interferometer will reduce the needed circulating power by an order of magnitude, bringing it into a range that is comparable to the expected circulating power of LIGO-II, if one wishes to beat the SQL by a factor of $\sqrt{10}$ in amplitude. Additional improvements to the sensitivity, particularly at high frequencies, can be achieved through the use of frequency-dependent homodyne detection.

In addition, it was shown that this type of speed-meter interferometer is not nearly as susceptible to losses as those presented in KLMTV. Its robust performance is due, in part, to the functional form the coupling factor κ, which is roughly constant at low frequencies. This helps to maintain the speed meters' wideband performance, even in the presence of losses. Losses for the various

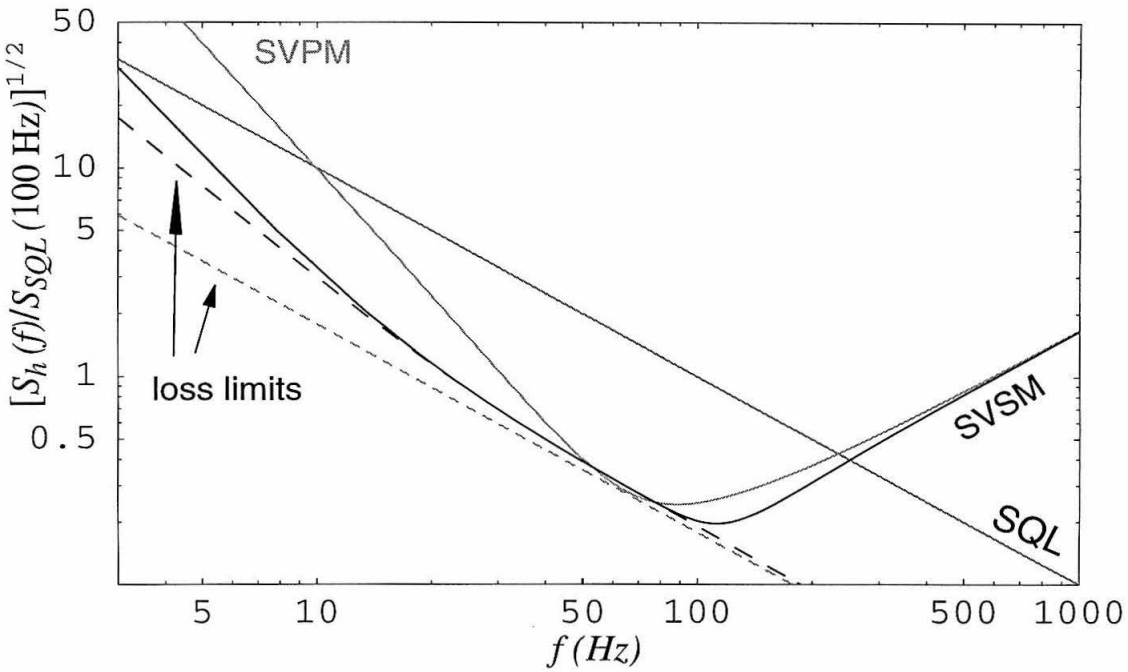

Figure 3.15: Comparison of noise curves for a squeezed-variational position meter (SVPM; analyzed in KLMTV) and for a squeezed-variational speed meter (SVSM; analyzed in this paper). Parameters used are those in Tables 3.1 and 3.3 with $T_{\rm i} = 0.005$ and $e^{-2R} = 0.1$. Also shown are the loss limits described in Sec. 3.6.3.

speed meters we discuss here are generally quite low. The dominant sources of loss-induced noise at low frequencies ($f \lesssim f_{\rm opt}$) are the radiation-pressure noise from losses in the arm, extraction, and sloshing cavities. Because this type of noise is dependent on the circulating power, it can be reduced by reducing the power by means of squeezed input.

3.8 Bibliography

[1] C. M. Caves, Phys. Rev. Lett. **45**, 75 (1980).

[2] A. Abramovici et al., Science **256**, 325 (1992).

[3] B. C. Barish and R. Weiss, Physics Today **52**, 44 (1999).

[4] W. G. Unruh, in *Quantum Optics, Experimental Gravitation, and Measurement Theory*, eds. P. Meystre and M. O. Scully (Plenum, 1982), p. 647.

[5] M. T. Jaekel and S. Reynaud, Europhys. Lett. **13**, 301 (1990).

[6] E. Gustafson, D. Shoemaker, K. Strain, and R. Weiss, *LSC White Paper on Detector Research and Development*, LIGO document T990080-00-D (1999); available along with other relevant information at http://www.ligo.caltech.edu/~ligo2/ .

[7] H. J. Kimble, Yu. Levin, A. B. Matsko, K. S. Thorne, and S. P. Vyatchanin, Phys. Rev. D **65**, 022002 (2001); cited in text as KLMTV.

[8] P. M. Purdue, Phys. Rev. D, in press; gr-qc/0111042; appears as Chapter 2 of this thesis.

[9] V. B. Braginsky and F. Ya. Khalily, Phys. Lett. A **218**, 167 (1996); V. B. Braginsky, M. L. Gorodetsky, and F. Ya. Khalili, Phys. Lett. A **232**, 340 (1997).

[10] V. B. Braginsky, M. L. Gorodetsky, and F. Ya. Khalili, Phys. Lett. A **246**, 485 (1998); quant-ph/9806081.

[11] F. Ya. Khalili, qr-qc/0203002.

[12] V. B. Braginsky and F. Ya. Khalili, Phys. Lett. A **147**, 251 (1990).

[13] V. B. Braginsky, M. L. Gorodetsky, F. Ya. Khalili, and K. S. Thorne, Phys. Rev. D **61**, 044002 (2000); cited in text as BGKT.

[14] C. M. Caves, Phys. Rev. D **23**, 1693 (1981).

[15] J. Mizuno, Ph.D. thesis, Max Planck Institute für Quantenoptik, 1995.

[16] A. Freise, G. Heinzel, K. A. Strain, J. Mizuno, K. D. Skeldon, H. Lück, B. Wilke, R. Schilling, A. Rüdiger, W. Wingler and K. Danzmann, Phys. Lett. A **277**, 135 (2000)

[17] J. Mason, Ph.D. thesis, California Institute of Technology, 2001; also available as LIGO document P010010-00-R at www.ligo.caltech.edu/docs/P/P010010-00.pdf .

[18] C. M. Caves and B. L. Schumaker, Phys. Rev. A **31**, 3068 (1985).

[19] B. L. Schumaker and C. M. Caves, Phys. Rev. A **31**, 3093 (1985).

[20] V. B. Braginsky, M. L. Gorodetsky, F. Ya. Khalili and K. S. Thorne, "Energetic Quantum Limit in Large-Scale Interferometers," in *Gravitational Waves*, Proceedings of the Third Edoardo Amaldi Conference, AIP Conference Proceedings Vol. 523, ed. Sydney Meshkov (American Institute of Physics, 2000) pp. 180–192; gr-qc/9907057.

[21] M. Xiao, L.-A. Wu and H. J. Kimble, Phys. Rev. Lett. **59** 278 (1987).

[22] P. Grangier, R. E. Slusher, B. Yurke and A. La Porta, Phys. Rev. Lett. **59**, 2153 (1987).

[23] K. S. Thorne (private communication).

[24] S. P. Vyatchanin and A. B. Matsko, JETP **77**, 218 (1993).

[25] S. P. Vyatchanin and E. A. Zubova, Phys. Lett. A **203**, 269 (1995).

[26] S. P. Vyatchanin and A. B. Matsko, JETP **82**, 1007 (1996).

[27] S. P. Vyatchanin and A. B. Matsko, JETP **83**, 690 (1996).

[28] S. P. Vyatchanin, Phys. Lett. A **239**, 201 (1998).

Chapter 4

The Gauge Invariance of General Relativistic Tidal Heating

Published as P. Purdue, *Physical Review D* **60**, 104054 (1999).

4.1 Summary

When a self-gravitating body (e.g., a neutron star or black hole) interacts with an external tidal field (e.g., that of a binary companion), the interaction can do work on the body, changing its mass-energy. The details of this "tidal heating" are analyzed using the Landau-Lifshitz pseudotensor and the local asymptotic rest frame of the body. It is shown that the work done on the body is gauge-invariant, while the body-tidal-field interaction energy contained within the body's local asymptotic rest frame is gauge dependent. This is analogous to Newtonian theory, where the interaction energy is shown to depend on how one localizes gravitational energy, but the work done on the body is independent of that localization.

4.2 Introduction

This is one in a series of papers that develops perturbative mathematical and physical tools for studying the interaction of an isolated gravitating body with a complicated "external universe" in the slow-motion limit. By "slow-motion limit" we mean that the shortest timescale τ for changes of the body's multipole moments and/or changes of the universe's tidal gravitational field is long compared to the body's size R: $R/\tau \ll 1$, where we have set the speed of light equal to unity.

In addition to this slow-motion requirement, we also require that the body be isolated from other objects in the external universe, in the sense that both the radius of curvature $\mathcal{R}$ of the external universe in the body's vicinity, and the lengthscale $\mathcal{L}$ on which the universe's curvature changes there, are long compared to the body's size: $R/\mathcal{R} \ll 1$ and $R/\mathcal{L} \ll 1$.

The slow-motion, isolated-body formalism, to which this paper is a technical addendum, is, in

essence, a perturbative expansion in powers of the small parameters R/τ, $R/\mathcal{R}$ and $R/\mathcal{L}$. For a detailed discussion of the structure of this expansion and its realm of validity, see Thorne and Hartle [1]. As they discuss at length (their Sec. I B), the slow-motion and isolated-body assumptions make no reference to the internal gravity of the object under study. Consequently, the Thorne-Hartle formalism in general, and the results of this paper in particular, can be applied even to strongly gravitating bodies, as long as the source of the external tidal field is far enough away to allow a "buffer zone" where gravity is weak. This buffer zone, called the local asymptotic rest frame, will be described more fully at the beginning of Sec. 4.4.

Two examples of isolated, slow-motion bodies are (i) a neutron star or black hole in a compact binary system that spirals inward due to emission of gravitational waves; and (ii) the satellite Io, which travels around Jupiter in an elliptic orbit and gets heated by Jupiter's tidal gravitational field [2].

The series of papers that has been developing the perturbative formalism for studying tidal effects in such slow-motion, isolated bodies is

1. The book *Gravitation* [3], Section 20.6 (written by John Wheeler): laid the conceptual foundations for analyzing the motion of such an isolated body through the external universe.

2. Thorne and Hartle [1]: formulated the problem of analyzing the effects of the external universe's tidal fields on such an isolated body, and conceived and initiated the development of the perturbative formalism for studying the influence of the tidal fields on the body's motion through the external universe, the precession of its spin axis, and its changes of mass-energy.

3. Thorne [4]: developed the theory of multipole moments of the isolated body in the form used by Thorne and Hartle.

4. Zhang [5]: developed the theory of multipole moments for the external universe's tidal gravitational fields, which underlies the work of Thorne and Hartle.

5. Zhang [6]: extended the Thorne-Hartle analysis of motion and precession to include higher order moments than they considered.

6. Thorne [7] and Flanagan [8]: initiated the study of tidally induced volume changes in the isolated body, using the above formalism. Their studies were motivated by numerical solutions of Einstein's equations by Wilson, Mathews, and Maronetti [9–12] which seemed to show each neutron star in a binary being compressed to the point of collapse by gravitational interaction with its companion. Thorne and Flanagan found no such effect of the large magnitude seen in the numerical solutions. An important piece of Thorne's analysis came from examining the work done on each star by its companion's tidal field—i.e., an analysis of "tidal heating."

Thorne's analysis of tidal heating required dealing with an issue that Thorne and Hartle had discussed, but avoided confronting: For an isolated body with mass quadrupole moment $\mathcal{I}_{jk}$, being squeezed by an external tidal gravitational field $\mathcal{E}_{jk} \equiv R_{j0k0}$ (with $R_{\alpha\beta\gamma\delta}$ the external Riemann

tensor), there appears to be an ambiguity in the body's total mass-energy M of order $\delta M \sim \mathcal{I}_{jk}\mathcal{E}_{jk}$. (Here and throughout we use locally Cartesian coordinates in the body's local asymptotic rest frame; cf. Thorne and Hartle [1]. Because the coordinates are Cartesian, it makes no difference whether tensor indices are placed up or down.)

One can understand this apparent ambiguity by examining the time-time part of the spacetime metric in the body's local asymptotic rest frame:

$$g_{00} = -1 + \frac{2M}{r} + \frac{3\mathcal{I}_{jk}n^j n^k}{r^3} + \ldots - \mathcal{E}_{jk}n^j n^k r^2 + \ldots \ . \tag{4.1}$$

Here $n^j = x^j/r$ is the unit radial vector and r is distance from the body in its local asymptotic rest frame. Among the terms omitted here are those of quadratic and higher order in the body's mass M and quadrupole moment $\mathcal{I}_{jk}$ and the external tidal field $\mathcal{E}_{jk}$—terms induced by nonlinearities of the Einstein field equations. Among these nonlinear terms is

$$\delta g_{00} \sim \frac{\mathcal{I}_{jk}\mathcal{E}_{jk}}{r} \ , \tag{4.2}$$

whose $1/r$ behavior can be deduced by dimensional considerations. This term has the multipolar structure (monopole)/r identical to that of the $2M/r$ term from which one normally reads off the body's total mass, and its numerical coefficient is ambiguous corresponding to the possibility to move some arbitrary portion of it into or out of the $2M/r$ term. Correspondingly, the body's mass is ambiguous by an amount of order

$$\delta M \sim \mathcal{I}_{jk}\mathcal{E}_{jk} \ . \tag{4.3}$$

In Sec. 4.3 of this paper we shall see that this ambiguity is not a purely relativistic phenomenon. In the Newtonian theory of gravity, there is also an ambiguity of magnitude (4.3) in that portion of the gravitational interaction energy of the body and external field which is contained within the body's local asymptotic rest frame. In Sec. 4.4 we shall explore the relativistic version of this "tidal-quadrupolar" interaction ambiguity by computing how the interaction energy changes under a relativistic change of gauge (infinitesimal coordinate transformation).

"Tidal heating" of the isolated body involves injecting into it an amount of energy that is of just the same magnitude as this ambiguity, $\Delta M \sim \mathcal{I}_{jk}\mathcal{E}_{jk}$. Does this mean that tidal heating is an ill-defined, unphysical concept? Certainly not, as is attested by photographs of volcanic plumes ejected from Jupiter's satellite Io (see, e.g., Ref. [14, 15]). That volcanism was predicted by Peale, Cassen, and Reynolds [2] before the Voyager spacecraft discovered it; and their explanation—that Io gets tidally heated to high internal temperature by the coupling of its quadrupole moment to Jupiter's tidal field—is firm (see, e.g., Refs. [16, 17]).

In this paper, we use the phrase "tidal heating" to mean the net work done by an external tidal

field on an isolated body. This phrase is slightly misleading, as the work done on the body need not necessarily go only into heat. The additional energy might be used to deform the body (i.e., raise a tide on it) or it might go into vibrational energy. If, however, timescales for changes of $\mathcal{E}_{jk}$ and $\mathcal{I}_{jk}$ are not close to the body's vibrational periods, then, when averaged over many cycles of change of $\mathcal{E}_{jk}$ and/or $\mathcal{I}_{jk}$, the work will contribute primarily to heat, as in the case of Io.

In his analysis of binary neutron star systems, Thorne [7] argued, but did not prove in detail, that although the tidal-quadrupole interaction energy is ambiguous, the amount of work done on an isolated body by an external tidal field (i.e., the amount of tidal heating) is unambiguously given by the formula[1]

$$\frac{dW}{dt} = -\frac{1}{2}\mathcal{E}_{ij}\frac{d\mathcal{I}_{ij}}{dt} \; ; \tag{4.4}$$

and he argued that this is true in general relativity theory as well as in Newtonian theory. In Sec. 4.3 we shall give a Newtonian demonstration of this claim. In Sec. 4.4 we shall give a relativistic demonstration—showing, more specifically, that although the quadrupole/tidal interaction energy is gauge dependent, the work done is gauge invariant and has the value (4.4).

4.3 Newtonian Analysis

In this section, we consider a Newtonian body, with weak internal gravity $|\Phi_{\rm o}| \ll 1$ (where $\Phi_{\rm o}$ is the body's gravitational potential), subjected to an external Newtonian tidal field. We assume that the external field is nearly homogeneous in the vicinity of the body, $\mathcal{L} \gg R$ (cf. Fig. 4.1; in the Newtonian case, the inner boundary of the vacuum "local asymptotic rest frame"[2]—indicated by the inner dashed circle—would be at the surface of the body).

In our analysis, we will consider a variety of contributions to the total energy inside a sphere which encompasses the body and whose boundary lies within the local asymptotic rest frame—i.e., the region where the external field is nearly homogeneous (again, cf. Fig. 4.1). We denote by $\mathcal{V}$ the interior of this sphere and by $\partial\mathcal{V}$ its boundary. Of greatest interest will be the interaction energy (between the body and the external tidal field) and the work done by the tidal field on the body. Both of these quantities are the result of slow changes of the tidal field $\mathcal{E}_{jk}$ and the body's quadrupole moment $\mathcal{I}_{jk}$.

As a foundation for our analysis, consider a fully isolated system that includes the body of interest and other "companion" bodies, which produce the tidal field $\mathcal{E}_{jk}$ that the body experiences. For simplicity, assume that all the bodies are made of perfect fluid (a restriction that can easily be abandoned). Then, for the full system, the Newtonian gravitational energy density and energy flux

[1] Actually, expression (4.4) is only the leading order term in the perturbative expansion of dW/dt. The next term is $-\frac{2}{3}\mathcal{B}_{ij}d\mathcal{S}_{ij}/dt$, where $\mathcal{B}_{ij}$ is the "magnetic type" tidal field of the external universe and $\mathcal{S}_{ij}$ is the body's current quadrupole moment [6]. In this paper we confine attention to the leading-order term.

[2] We shall discuss the concept of "local asymptotic rest frame" near the beginning of Sec. 4.4.

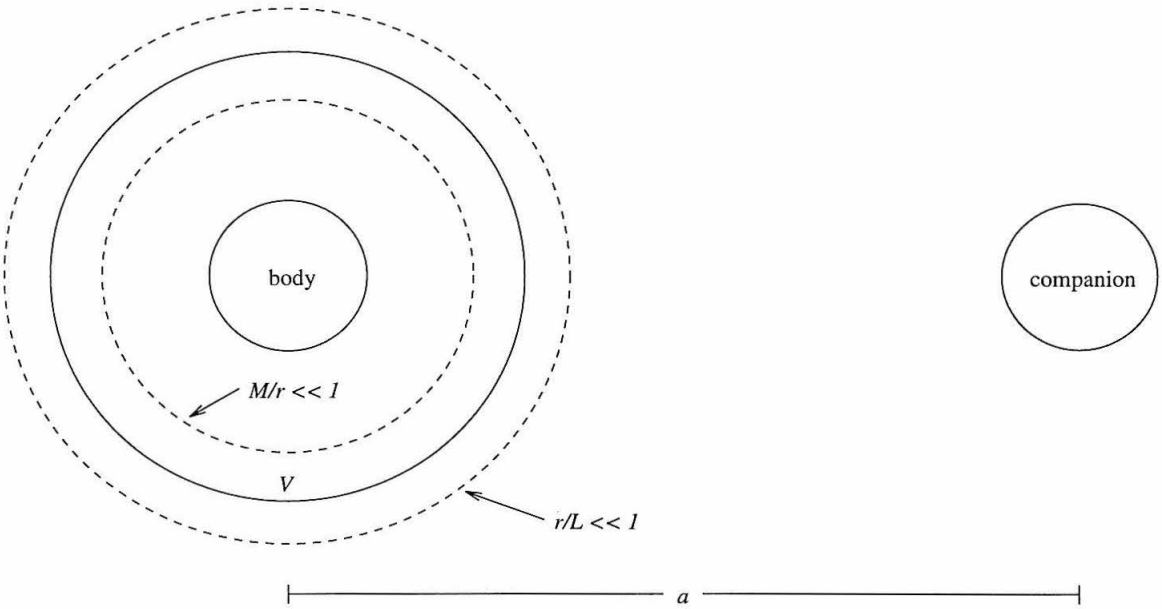

Figure 4.1: An example of an isolated, slow-motion body: a star or black hole in a binary system with $R/a \ll 1$, where R is the radius of the body and a is the separation of the body and companion. The dashed circles indicate the boundaries of the body's vacuum local asymptotic rest frame, the region in which $M/r \ll 1$ and $r/\mathcal{L} \ll 1$. Here, r is the radial coordinate, M is the mass of the body, and $\mathcal{L}$ is the scale of homogeneity of the gravitational field. The boundary of the sphere over which we integrate, denoted by $\partial\mathcal{V}$, lies within this region.

can be written as

$$\Theta_1^{00} = \rho\left(\frac{1}{2}v^2 + \Pi + \Phi\right) + \frac{1}{8\pi}\Phi_{,j}\Phi_{,j}\,, \tag{4.5}$$

$$\Theta_1^{0j} = \rho v^j\left(\frac{1}{2}v^2 + \Pi + \frac{p}{\rho} + \Phi\right) - \frac{1}{4\pi}\Phi_{,t}\Phi_{,j}\,, \tag{4.6}$$

where Φ, ρ, p, v, and Π are the Newtonian gravitational potential, mass density, pressure, velocity, and specific internal energy [7].

Using conservation of rest mass $\rho_{,t}+(\rho v^j)_{,j} = 0$, the first law of thermodynamics $\rho d\Pi/dt + pv^j{}_{,j} = 0$, the Euler equation for fluids $\rho dv^j/dt + \rho\Phi_{,j} + p_{,j} = 0$, Newton's field equation $\Phi_{,jj} = 4\pi\rho$, and the definition of the comoving time derivative $d/dt = \partial/\partial t + v^j\partial/\partial x^j$, it can be shown that Eqs. (4.5) and (4.6) satisfy conservation of energy

$$\Theta^{00}{}_{,t} + \Theta^{0j}{}_{,j} = 0. \tag{4.7}$$

Equations (4.5) and (4.6) for the energy density and flux, however, are not unique. Equally valid

are the following expressions:

$$\Theta_2^{00} = \rho\left(\frac{1}{2}v^2 + \Pi\right) - \frac{1}{8\pi}\Phi_{,j}\Phi_{,j} , \tag{4.8}$$

$$\Theta_2^{0j} = \rho v^j\left(\frac{1}{2}v^2 + \Pi + \frac{p}{\rho} + \Phi\right) + \frac{1}{4\pi}\Phi_{,tj}\Phi , \tag{4.9}$$

which also satisfy energy conservation (4.7) but localize the gravitational energy in a different manner from $\Theta_1^{0\mu}$. Energy conservation (4.7) will also be satisfied by any linear combination of $\Theta_1^{0\mu}$ and $\Theta_2^{0\mu}$. Imposing the additional condition that, for any acceptable Θ, the system's total energy

$$E = \int \Theta^{00} d^3x \tag{4.10}$$

must be independent of the choice of Θ^{00} forces the coefficients to sum to 1. Hence, a perfectly valid form for $\Theta^{0\mu}$ is

$$\Theta^{0\mu} = \alpha\Theta_1^{0\mu} + (1-\alpha)\Theta_2^{0\mu} , \tag{4.11}$$

where α is an arbitrary constant.

Notice that the choice of α gives a specific energy localization. For example, $\alpha = 0$ puts the gravitational energy entirely in the field $[-(\nabla\Phi)^2/(8\pi)]$, so it is nonzero outside the matter. This is analogous to the localization used in electrostatics ($1/8\pi$ times the square of the electric field). Choosing $\alpha = \frac{1}{2}$, by contrast, puts the gravitational energy entirely in the matter ($\frac{1}{2}\rho\Phi$), so it vanishes outside the body. When $\frac{1}{2}\rho\Phi$ is integrated over the entire system (body plus its companions), the result is a widely used way of computing gravitational energy (e.g., Sec. 17.1 of Ref. [18]).

The energy in the region $\mathcal{V}$ that contains and surrounds the body but excludes the companion,

$$E_{\mathcal{V}} = \int_{\mathcal{V}} \Theta^{00} d^3x , \tag{4.12}$$

will depend on α; i.e., it will depend on where the energy is localized. By contrast, the total energy (4.10) for the fully isolated system (body plus its companions) will be independent of α.

Another way to express this ambiguity of the localization of the gravitational energy is given by Thorne (Appendix of Ref. [7]): it is possible to add the divergence of $\eta_j = \beta\Phi\Phi_{,j}$ (where β is an arbitrary constant) to Θ_1^{00} and the time derivative of $-\eta_j$ to Θ_1^{0j} without affecting energy conservation (4.7) or the physics of the system. Indeed, this method is completely equivalent to the one presented above. The constants are related by $\beta = (\alpha - 1)/4\pi$.

Throughout the region $\mathcal{V}$, the Newtonian gravitational potential can be broken into two parts: the body's self field $\Phi_{\rm o}$ and the tidal field $\Phi_{\rm e}$ produced by the external universe (the companion

bodies), so that

$$\Phi = \Phi_{\rm o} + \Phi_{\rm e} \ . \tag{4.13}$$

The external field is quadrupolar and source-free in the region $\mathcal{V}$ so that

$$\Phi_{\rm e} = \frac{1}{2}\mathcal{E}_{ij}x^i x^j \ , \quad \Phi_{{\rm e},jj} = 0 \ , \tag{4.14}$$

and, furthermore, the tidal field $\mathcal{E}_{ij}$ evolves slowly with time. The body's (external) self field is monopolar and quadrupolar and has the body's mass distribution as a source:

$$\Phi_{\rm o} = -\frac{M}{r} - \frac{3}{2}\frac{\mathcal{I}_{ij}n^i n^j}{r^3} \ , \quad \Phi_{{\rm o},jj} = 4\pi\rho \ . \tag{4.15}$$

The quadrupole moment $\mathcal{I}_{ij}$, like that of the external field, evolves slowly with time, but the body's mass M is constant. Recall that $r \equiv \sqrt{\delta_{ij}x^i x^j}$ is radial distance from the body's center of mass and $n^j \equiv x^j/r$ is the radial vector.

A useful expression for the total energy $E_{\mathcal{V}}$ in the spherical region $\mathcal{V}$ can be derived by inserting Eqs. (4.11), (4.5), (4.8), and (4.13) into Eq. (4.12). The resulting expression can be broken into a sum of three parts—the body's self energy $E_{\rm o}$ (which depends only on $\Phi_{\rm o}$ and ρ), the external field energy $E_{\rm e}$ (which depends only on $\Phi_{\rm e}$), and the interaction energy $E_{\rm int}$ (which involves products of $\Phi_{\rm e}$ with ρ or $\Phi_{\rm o}$):

$$E_{\mathcal{V}} = E_{\rm o} + E_{\rm e} + E_{\rm int} \ , \tag{4.16}$$

where

$$E_{\rm o} = \int_{\mathcal{V}}\left[\rho\left(\frac{1}{2}v^2 + \Pi\right) + \alpha\rho\Phi_{\rm o} + \frac{(2\alpha-1)}{8\pi}\Phi_{{\rm o},j}\Phi_{{\rm o},j}\right]d^3x \ , \tag{4.17}$$

$$E_{\rm e} = \int_{\mathcal{V}}\left[\frac{(2\alpha-1)}{8\pi}\Phi_{{\rm e},j}\Phi_{{\rm e},j}\right]d^3x \ , \tag{4.18}$$

$$E_{\rm int} = \int_{\mathcal{V}}\left[\alpha\rho\Phi_{\rm e} + \frac{(2\alpha-1)}{4\pi}\Phi_{{\rm o},j}\Phi_{{\rm e},j}\right]d^3x \ . \tag{4.19}$$

Inserting Eqs. (4.14) and (4.15) into Eq. (4.19) and integrating gives the interaction energy inside $\mathcal{V}$ as

$$E_{\rm int} = \frac{(2+\alpha)}{10}\mathcal{E}_{ij}\mathcal{I}_{ij} \ , \tag{4.20}$$

which depends on α. In other words, it depends on our arbitrary choice of how to localize gravitational energy. This is the ambiguity of the interaction energy discussed in Sec. 4.2.

The rate of change of the total energy inside $\mathcal{V}$ can be expressed in the form

$$\frac{dE_{\mathcal{V}}}{dt} = -\int_{\partial\mathcal{V}} \Theta^{0j} n^j r^2 d\Omega \tag{4.21}$$

by taking the time derivative of Eq. (4.12), inserting Eq. (4.7), and applying the divergence theorem. This expression, like that for the energy, can be broken into a sum by combining Eqs. (4.11), (4.6), (4.9), (4.13), (4.14), (4.15), and (4.20):

$$\frac{dE_{\mathcal{V}}}{dt} = \frac{dE_{\rm e}}{dt} + \frac{dE_{\rm int}}{dt} - \frac{1}{2}\mathcal{E}_{ij}\frac{d\mathcal{I}_{ij}}{dt} + \int_{\partial\mathcal{V}} \frac{1}{4\pi}\left[\alpha\Phi_{{\rm o},t}\Phi_{{\rm o},j} + (\alpha-1)\,\Phi_{{\rm o},tj}\Phi_{\rm o}\right] n^j r^2 d\Omega\,. \tag{4.22}$$

The first term is the rate of change of the external field energy (4.18) inside $\mathcal{V}$, resulting from the evolution of the tidal field. The second term is the rate of change of the interaction energy (4.20). The third and fourth terms together, by comparison with Eq. (4.16), must be equal to $dE_{\rm o}/dt$, the rate of change of the body's self energy. The fourth term is the contribution from the body's own field moving across the boundary $\partial\mathcal{V}$. Therefore, the third term gives the change in the body's energy coming from the interaction with the tidal field; in other words, it is the rate of work done on the body by the tidal field. Furthermore, this term is independent of α and is, consequently, independent of how the Newtonian energy is localized, as claimed in Sec. 4.2, Eq. (4.4).

4.4 Relativistic Analysis

In this section, we will exhibit a relativistic version of the calculation in Sec. 4.3, again showing that the rate of work done on the body by the tidal field is gauge invariant and that it has the same value in a general relativistic perturbative treatment as in the Newtonian one: $-(1/2)\mathcal{E}_{ij}d\mathcal{I}_{ij}/dt$. The formalism to be used is the Landau-Lifshitz energy-momentum pseudotensor and multipole expansions as developed by Thorne and Hartle [1] and Zhang [5, 6], together with the slow-motion approximation, so time derivatives are small compared to spatial gradients.

We will work in the body's vacuum local asymptotic rest frame, which is defined as a region outside the body and far enough from it that its gravitational field can be regarded as a weak perturbation of flat spacetime, yet near enough that the tidal field of the external universe can be regarded as nearly homogeneous. This region is a spherical shell around the body; its inner boundary is near the body's surface but far enough away for gravity to be weak, and its outer boundary is at a distance where the external tidal field begins to depart from homogeneity (see Fig. 4.1). Somewhat more precisely, the local asymptotic rest frame is the region throughout which $r/\mathcal{L} \ll 1$, $r/\mathcal{R} \ll 1$, and $M/r \ll 1$, where r is the radial distance from the body, M is the mass of the body, and $\mathcal{R}$ and $\mathcal{L}$ are the radius of curvature and the scale of homogeneity of the external gravitational field. If this region exists (as in the case of a black hole binary far from merger, for example) and the

slow-motion limit applies, then the following analysis is valid.

As in the Newtonian case, we will consider contributions to the total energy inside a sphere $\mathcal{V}$ which encompasses the body and whose boundary $\partial\mathcal{V}$ lies within the local asymptotic rest frame (see Fig. 4.1).

4.4.1 deDonder Gauge

We shall begin by computing the work done on the body by the external tidal field, using deDonder gauge (this section). Then in the next section, we shall show that the work is gauge invariant.

DeDonder gauge is defined by the condition that $\bar{h}^{\alpha\beta}{}_{,\beta} = 0$, where $\bar{h}^{\alpha\beta}$ is defined in terms of the metric density as follows:

$$\mathfrak{g}^{\alpha\beta} \equiv \sqrt{-g}\, g^{\alpha\beta} \equiv \eta^{\alpha\beta} - \bar{h}^{\alpha\beta} \,. \tag{4.23}$$

At linear order in the strength of gravity, $\bar{h}^{\alpha\beta}$ is the trace-reversed metric perturbation. According to Zhang [6], the components of $\bar{h}^{\alpha\beta}$ in the body's local asymptotic rest frame are, at leading (linear) order in the strength of gravity and at leading non-zero order in our slow-motion expansion,

$$\bar{h}^{00} \equiv -4\Phi = 4\frac{M}{r} + 6\frac{\mathcal{I}_{ij}x^i x^j}{r^5} - 2\mathcal{E}_{ij}x^i x^j, \tag{4.24}$$

$$\bar{h}^{0j} \equiv -A_j = 6\frac{\dot{\mathcal{I}}_{ja}x^a}{r^3} + \frac{10}{21}\dot{\mathcal{E}}_{ab}x^a x^b x^j - \frac{4}{21}\dot{\mathcal{E}}_{ja}x^a r^2, \tag{4.25}$$

$$\bar{h}^{ij} = \mathcal{O}\left(\ddot{\mathcal{E}}_{ij}r^4 \;\&\; \frac{\ddot{\mathcal{I}}_{ij}}{r}\right), \tag{4.26}$$

where the dots indicate time derivatives (i.e., $\dot{\mathcal{I}}_{ij} \equiv d\mathcal{I}_{ij}/dt$) and the symbol "&" means "plus terms of the form and magnitude." Note that the higher-order (ℓ-order) multipoles have been omitted, since their contributions are smaller by $\sim (r/\mathcal{L})^{\ell-2} \leq r/\mathcal{L} \ll 1$ and $\sim (M/r)^{\ell-2} \leq M/r \ll 1$ than the quadrupolar ($\ell = 2$) terms that we have kept. The second time derivatives will also be neglected since they are unimportant in the slow-motion approximation; this effectively eliminates $\bar{h}^{ij}$ in this gauge. Also, note that the Φ in Eq. (4.24) has the same form as the Newtonian gravitational potential of Sec. 4.3, and the A_j of Eq. (4.25) is a gravitational vector potential, which does not appear in Newtonian theory.

In general, it would be possible to have a term $\propto \mathcal{I}_{jk}\mathcal{E}_{jk}/r$ in Eq. (4.24), as well as the $\propto M/r$ term. We have chosen to define the constant for the monopolar term to be $4M$, thereby eliminating any term $\propto \mathcal{I}_{jk}\mathcal{E}_{jk}/r$; this is arbitrary but convenient, as will be seen shortly.

The total mass-energy $\mathcal{M}_{\mathcal{V}}$ inside the sphere $\mathcal{V}$ (total stellar mass including the quadrupolar deformation energy and energy of interaction between the deformation and tidal field) is defined by Thorne and Hartle (Eq. (2.2a) of Ref. [1]) in terms of the Landau-Lifshitz superpotential as

$$\mathcal{M}_{\mathcal{V}} = \frac{1}{16\pi}\int_{\partial\mathcal{V}} H^{0\alpha 0j}{}_{,\alpha} n_j r^2 d\Omega \ , \tag{4.27}$$

where

$$H^{\mu\alpha\nu\beta} = \mathfrak{g}^{\mu\nu}\mathfrak{g}^{\alpha\beta} - \mathfrak{g}^{\alpha\nu}\mathfrak{g}^{\mu\beta} \ ; \tag{4.28}$$

cf. Eqs. (20.6), (20.3), and (20.20) of MTW [3] and Eqs. (100.14) and (100.2) of Landau and Lifshitz [19]. Using Eqs. (4.28), (4.23), and (4.24)–(4.26) in Eq. (4.27) and carrying out the integration gives

$$\mathcal{M}_{\mathcal{V}} = M + \mathcal{O}\left(\mathcal{E}\ddot{\mathcal{E}}r^7 \ \& \ \dot{\mathcal{E}}\dot{\mathcal{E}}r^7\right) + \mathcal{O}\left(\dot{\mathcal{I}}\dot{\mathcal{E}}r^2 \ \& \ \ddot{\mathcal{I}}\mathcal{E}r^2 \ \& \ \mathcal{I}\ddot{\mathcal{E}}r^2\right) + \mathcal{O}\left(\frac{\mathcal{I}\ddot{\mathcal{I}}}{r^3} \ \& \ \frac{\dot{\mathcal{I}}\dot{\mathcal{I}}}{r^3}\right) \ . \tag{4.29}$$

Hence, $\mathcal{M}_{\mathcal{V}} = M$ at leading order in our slow-motion approximation when we neglect the double- and higher-order time derivatives. This is the reason the constant of the monopolar term in Eq. (4.24) was chosen to be $4M$.

To calculate the rate of work done by the tidal field on the body when $\mathcal{E}_{jk}$ and $\mathcal{I}_{jk}$ change slowly, we consider the change of the mass-energy $\mathcal{M}_{\mathcal{V}}$,

$$-\frac{d\mathcal{M}_{\mathcal{V}}}{dt} \ = \ \int_{\partial\mathcal{V}} (-g) t^{0j} n_j r^2 d\Omega \ , \tag{4.30}$$

where $t^{\mu\nu}$ is the Landau-Lifshitz pseudotensor. That this expression is indeed the time derivative of Eq. (4.27) is a result of Gauss's theorem (see discussion after Eqs. (2.3) of Ref. [1]).

In the body's local asymptotic rest frame, the Landau-Lifshitz energy-momentum pseudotensor (Eq. (20.22) in MTW [3]) is, at the orders of accuracy we are considering,

$$(-g)t^{00} \ = \ \frac{1}{16\pi}\left(-\frac{7}{8}\right) g^{ij}\bar{h}^{00}{}_{,i}\bar{h}^{00}{}_{,j} = -\frac{7}{8\pi}\delta^{ij}\Phi_{,i}\Phi_{,j} \ , \tag{4.31}$$

$$\begin{aligned}(-g)t^{0j} \ &= \ \frac{1}{16\pi}\left(\frac{3}{4}\bar{h}^{00}{}_{,0}\bar{h}^{00}{}_{,j} + \bar{h}^{00}{}_{,m}\bar{h}^{0m}{}_{,j} - \bar{h}^{00}{}_{,m}\bar{h}^{0j}{}_{,m}\right) \\ &= \ \frac{3}{4\pi}\Phi_{,0}\Phi_{,j} + \frac{1}{4\pi}\left(A_{k,j} - A_{j,k}\right)\Phi_{,k} \ .\end{aligned} \tag{4.32}$$

Here the deDonder gauge condition $\bar{h}^{\alpha\beta}{}_{,\beta} = 0$ has been used to eliminate many terms from the general expression in MTW, but most of the simplification has come from keeping only terms of leading-order in the slow-motion approximation [zeroth and first time derivatives, respectively, in Eqs. (4.31) and (4.32)]. This restriction has given us only products of $\bar{h}^{\mu\nu}{}_{,\alpha}$ which will produce terms containing the products M^2, $M\mathcal{E}$, $M\mathcal{I}$, $\mathcal{I}\mathcal{E}$, $\mathcal{I}\mathcal{I}$, $\mathcal{E}\mathcal{E}$ for $(-g)t^{00}$ and $M\dot{\mathcal{I}}$, $M\dot{\mathcal{E}}$, $\mathcal{I}\dot{\mathcal{E}}$, $\mathcal{E}\dot{\mathcal{I}}$, $\mathcal{I}\dot{\mathcal{I}}$, $\mathcal{E}\dot{\mathcal{E}}$ for $(-g)t^{0j}$. This may be illustrated by expressing $(-g)t^{0\alpha}$ explicitly in terms of the quadrupole moments by substituting Eqs. (4.24) and (4.25) into Eqs. (4.31) and (4.32) to get

$$(-g)t^{00} = \frac{1}{16\pi}\left(-14\frac{M^2}{r^4} - 210\frac{\mathcal{I}_{ab}\mathcal{E}_{cd}x^a x^b x^c x^d}{r^7} + 84\frac{\mathcal{I}_{ab}\mathcal{E}_{bc}x^a x^c}{r^5} - 28\frac{M\mathcal{E}_{ab}x^a x^b}{r^3} - 14\mathcal{E}_{ab}\mathcal{E}_{bc}x^a x^c \right.$$
$$\left. -126\frac{M\mathcal{I}_{ab}x^a x^b}{r^8} - 126\frac{\mathcal{I}_{ab}\mathcal{I}_{bc}x^a x^c}{r^{10}} - \frac{315}{2}\frac{\mathcal{I}_{ab}\mathcal{I}_{cd}x^a x^b x^c x^d}{r^{12}}\right), \tag{4.33}$$

and

$$(-g)t^{0j} = \frac{1}{16\pi}\left(-18\frac{\dot{\mathcal{I}}_{ab}\mathcal{E}_{cj}x^a x^b x^c}{r^5} + 24\frac{\dot{\mathcal{I}}_{ab}\mathcal{E}_{bc}x^a x^c x^j}{r^5} - 24\frac{\dot{\mathcal{I}}_{aj}\mathcal{E}_{bc}x^a x^b x^c}{r^5} - 18\frac{\mathcal{I}_{aj}\dot{\mathcal{E}}_{bc}x^a x^b x^c}{r^5} \right.$$
$$\left. -24\frac{\mathcal{I}_{ab}\dot{\mathcal{E}}_{cj}x^a x^b x^c}{r^5} - 16\frac{\mathcal{I}_{ab}\dot{\mathcal{E}}_{bc}x^a x^c x^j}{r^5} + 85\frac{\mathcal{I}_{ab}\dot{\mathcal{E}}_{cd}x^a x^b x^c x^d x^j}{r^7}\right). \tag{4.34}$$

Note that we have kept only the $\mathcal{EI}$ cross terms in the expression for $(-g)t^{0j}$, as only they will contribute to our calculation of the interaction energy and work.

We find the rate of change of mass-energy inside our sphere $\mathcal{V}$ by inserting Eq. (4.34) into Eq. (4.30) and integrating. The result (only considering the cross terms) is

$$-\frac{d\mathcal{M}_{\mathcal{V}}}{dt} = \frac{d}{dt}\left(\frac{1}{10}\mathcal{E}_{ij}\mathcal{I}_{ij}\right) + \frac{1}{2}\mathcal{E}_{ij}\frac{d}{dt}\mathcal{I}_{ij}\,. \tag{4.35}$$

Since the interaction energy can depend only on the instantaneous deformation and tidal field, its rate of change must be a perfect differential, whereas the rate of work need not be. Also, if the tidal field changes but the body does not, there is no work done. From these two facts, we can conclude that the first term of Eq. (4.35) is the rate of change of the interaction energy between the tidal field and the body and that the second term represents the rate of work done by the external field on the body (the "tidal heating").

Notice that this value for the rate of work matches that discussed in Sec. 4.2, Eq. (4.4), and found via the Newtonian analysis in Sec. 4.3. Note the comparison with our Newtonian expressions (4.22) and (4.20). The first and fourth terms of Eq. (4.22) are missing here because we included in our $(-g)t^{0j}$ only the (body field)×(external field) cross terms. If we had also included (external)×(external) and (body)×(body) terms, Eq. (4.35) would have entailed expressions like the first and fourth terms of Eq. (4.22). Note also from the interaction energy terms in Eqs. (4.22), (4.20), and (4.35) that the Landau-Lifshitz way of localizing gravitational energy corresponds to the Newtonian choice $\alpha = -3$, a correspondence that has previously been derived by Chandrasekhar [20].

4.4.2 General Gauge

In Sec. 4.4.1, we considered the special case of deDonder gauge, which was particularly simple due to the gauge condition and to the $\bar{h}^{ij}$ terms being effectively zero. Now we will examine a general gauge, which can be achieved by a gauge transformation of the form

$$\begin{aligned} \bar{h}_{\mu\nu} &\rightarrow \bar{h}_{\mu\nu} + \delta\bar{h}_{\mu\nu} \ ; \\ \delta\bar{h}_{\mu\nu} &= \xi_{\mu,\nu} + \xi_{\nu,\mu} - \eta_{\mu\nu}\xi^{\alpha}{}_{,\alpha} \ , \end{aligned} \tag{4.36}$$

where ξ^{α} is a function to be chosen shortly. Using $\bar{h}_{\mu\nu} \equiv h_{\mu\nu} - \frac{1}{2}\eta_{\mu\nu}h^{\sigma}{}_{\sigma}$, where $h_{\mu\nu}$ is the perturbation of the metric away from the Minkowski metric in the local asymptotic rest frame, this can also be expressed as

$$\begin{aligned} h_{\mu\nu} &\rightarrow h_{\mu\nu} + \delta h_{\mu\nu} \ ; \\ \delta h_{\mu\nu} &= \xi_{\mu,\nu} + \xi_{\nu,\mu} \ . \end{aligned} \tag{4.37}$$

Note that in the deDonder gauge,

$$h_{00} = 2\frac{M}{r} + 3\frac{\mathcal{I}_{ij}x^i x^j}{r^5} - \mathcal{E}_{ij}x^i x^j, \tag{4.38}$$

$$h_{0j} = -6\frac{\dot{\mathcal{I}}_{ja}x^a}{r^3} - \frac{10}{21}\dot{\mathcal{E}}_{ab}x^a x^b x^j + \frac{4}{21}\dot{\mathcal{E}}_{ja}x^a r^2, \tag{4.39}$$

$$h_{ij} = \delta_{ij}\left(2\frac{M}{r} + 3\frac{\mathcal{I}_{k\ell}x^k x^\ell}{r^5} - \mathcal{E}_{k\ell}x^k x^\ell\right). \tag{4.40}$$

Since we are interested only in gauge changes of the same order as we have been using so far (leading-order in the slow-motion approximation), we include only terms in ξ_α that will produce $\delta h_{\mu\nu}$ of the same forms as Eqs. (4.38)–(4.40), but with different numerical coefficients. For example, consider $\delta h_{00} = 2\xi_{0,0} \propto M/r$; that gives $\xi_0 \propto Mt/r$, since M is a constant. This, in turn, implies $\delta h_{0j} = \xi_{0,j} \propto Mtx^j/r^3$, but this is not of the same form as the terms in Eq. (4.39); rather, it corresponds to a gauge that rapidly becomes ill-behaved as time passes. Similar arguments apply to $\delta h_{00} \propto \mathcal{I}_{jk}x^j x^k/r^5$ or $\delta h_{00} \propto \mathcal{E}_{jk}x^j x^k$; their coefficients cannot be altered by a gauge change because such a change would alter the mathematical form of h_{0j} and would make its magnitude unacceptably large in the slow-motion limit. As a result, we must set $\xi_0 = 0$. If we now consider $\delta h_{0j} = \xi_{j,0}$, possible terms are of the form $\propto \dot{\mathcal{I}}_{ja}x^a/r^3$, $\propto \dot{\mathcal{E}}_{ab}x^a x^b x^j$, or $\propto \dot{\mathcal{E}}_{ja}x^a r^2$; cf. Eq. (4.39). Each of these gives $\delta h_{00} = 0$ and δh_{ij} of the same form as Eq. (4.40); hence, terms of these forms are allowed. Consequently, the most general gauge change that preserves the mathematical forms of $h_{\mu\nu}$ but alters their numerical coefficients is

$$\begin{aligned}\xi_0 &= 0\,,\\ \xi_j &= \alpha\frac{\mathcal{I}_{ja}x^a}{r^3}+\beta\mathcal{E}_{ja}x^a r^2+\gamma\mathcal{E}_{ab}x^a x^b x^j\,,\end{aligned}\tag{4.41}$$

where α, β, and γ are arbitrary constants.

Using the trace-reversed gauge change (4.36) with Eq. (4.41), the new $\bar{h}^{\alpha\beta}$ become

$$\bar{h}^{00} = 4\frac{M}{r}+(5\gamma+2\beta-2)\mathcal{E}_{ij}x^i x^j+(6-3\alpha)\mathcal{I}_{ij}\frac{x^i x^j}{r^5}\,,\tag{4.42}$$

$$\bar{h}^{0j} = (2-\alpha)\dot{\mathcal{I}}_{ja}\frac{x^a}{r^3}+(\frac{10}{21}-\gamma)\dot{\mathcal{E}}_{ab}x^a x^b x^j-(\frac{4}{21}+\beta)\dot{\mathcal{E}}_{ja}x^a r^2\,,\tag{4.43}$$

$$\begin{aligned}\bar{h}^{jk} &= 2\alpha\mathcal{I}_{jk}\frac{1}{r^3}+3\alpha\delta^{jk}\mathcal{I}_{ab}\frac{x^a x^b}{r^5}-3\alpha\mathcal{I}_{ja}\frac{x^a x^k}{r^5}-3\alpha\mathcal{I}_{ka}\frac{x^a x^j}{r^5}+2\beta\mathcal{E}_{jk}r^2\\ &\quad -2(\beta+\gamma)\delta^{jk}\mathcal{E}_{ab}x^a x^b+2(\beta+\gamma)\mathcal{E}_{ja}x^a x^k+2(\beta+\gamma)\mathcal{E}_{ka}x^a x^j\,.\end{aligned}\tag{4.44}$$

In this general gauge, if we calculate the total mass-energy $\mathcal{M}_\mathcal{V}$ inside the sphere $\mathcal{V}$ using Eqs. (4.28), (4.23), and (4.42)–(4.44) in Eq. (4.27), we find

$$\mathcal{M}_\mathcal{V} = M+\left(2\gamma^2+\frac{29}{5}\beta\gamma-\frac{4}{5}\gamma+2\beta^2-2\beta\right)\mathcal{E}_{ij}\mathcal{E}_{ij}r^5+\left(\frac{1}{3}\alpha+2\beta+\frac{7}{5}\gamma-\frac{4}{3}\alpha\beta-\frac{23}{15}\alpha\gamma\right)\mathcal{I}_{ij}\mathcal{E}_{ij}\,.\tag{4.45}$$

The $\mathcal{I}_{ij}\mathcal{I}_{ij}/r^5$ term is zero. It is comforting to note that all the new terms vanish for $\alpha=\beta=\gamma=0$, giving the deDonder result $\mathcal{M}_\mathcal{V}=M$. The $\mathcal{E}\mathcal{E}r^5$ and $\mathcal{I}\mathcal{E}$ terms in Eq. (4.45) are large compared to the double time-derivative terms that formed the largest corrections to the mass-energy in deDonder gauge (4.29); however, they are still small compared to the mass M that appears in the expansion (4.24) of $\bar{h}^{00}$. Also note that, near the body of interest, the $\mathcal{E}\mathcal{E}r^5$ term will be small compared to the $\mathcal{I}\mathcal{E}$ term, due to its radial dependence. So, once again, we have $\mathcal{M}_\mathcal{V}\simeq M$ as a first approximation, although it is necessary to keep the extra terms in Eq. (4.45) to maintain the same level of accuracy as we have been using. Consequently, $\mathcal{M}_\mathcal{V}$ is gauge-dependent to the order that interests us, and it has the "$\mathcal{I}_{ij}\mathcal{E}_{ij}$" ambiguity discussed by Thorne and Hartle [1] and mentioned in Sec. 4.2.

Keeping only the leading-order terms in the slow-motion approximation, as described in Sec. 4.4.1, the Landau-Lifshitz pseudotensor in the new gauge is

$$(-g)t^{00} = \frac{1}{16\pi}\left(-\frac{7}{8}g^{ij}\bar{h}^{00}{}_{,i}\bar{h}^{00}{}_{,j}+\bar{h}^{00}{}_{,i}\bar{h}^{ij}{}_{,j}-\frac{1}{2}\bar{h}^{ij}{}_{,k}\bar{h}^{ik}{}_{,j}+\frac{1}{4}\bar{h}^{00}{}_{,i}\bar{h}^{jj}{}_{,i}+\frac{1}{4}\bar{h}^{ij}{}_{,k}\bar{h}^{ij}{}_{,k}-\frac{1}{8}\bar{h}^{ii}{}_{,k}\bar{h}^{jj}{}_{,k}\right)\,,\tag{4.46}$$

$$
\begin{aligned}
(-g)t^{0j} \;=\; & \frac{1}{16\pi}\Bigg(\frac{3}{4}\bar{h}^{00}{}_{,0}\bar{h}^{00}{}_{,j} + \bar{h}^{00}{}_{,m}\bar{h}^{0m}{}_{,j} - \bar{h}^{00}{}_{,m}\bar{h}^{0j}{}_{,m} + \bar{h}^{0j}{}_{,k}\bar{h}^{kl}{}_{,l} - \bar{h}^{00}{}_{,0}\bar{h}^{ij}{}_{,j} + \bar{h}^{ij}{}_{,k}\bar{h}^{ik}{}_{,0} \\
& -\bar{h}^{0i}{}_{,k}\bar{h}^{ik}{}_{,j} + \bar{h}^{0i}{}_{,k}\bar{h}^{ij}{}_{,k} - \bar{h}^{0i}{}_{,i}\bar{h}^{jk}{}_{,k} - \frac{1}{4}\bar{h}^{kk}{}_{,0}\bar{h}^{00}{}_{,j} - \frac{1}{4}\bar{h}^{00}{}_{,0}\bar{h}^{kk}{}_{,j} - \frac{1}{2}\bar{h}^{ik}{}_{,0}\bar{h}^{ik}{}_{,j} \\
& +\frac{1}{4}\bar{h}^{ii}{}_{,0}\bar{h}^{kk}{}_{,j}\Bigg) \,. \qquad (4.47)
\end{aligned}
$$

Note that the first term of Eq. (4.46) is the same as Eq. (4.31), and the first three terms of Eq. (4.47) are the same as Eq. (4.32). The additional terms all involve $\bar{h}^{jk}$, which was effectively zero in the deDonder gauge because of our slow-motion assumption.

Substituting Eqs. (4.47) and (4.42)–(4.44) into Eq. (4.30) and integrating gives the rate of change of mass-energy inside the sphere $\mathcal{V}$ as

$$
-\frac{d\mathcal{M}_{\mathcal{V}}}{dt} = \frac{d}{dt}\left[\left(\frac{7\alpha\gamma}{5} - \frac{9\gamma}{5} + \frac{7\alpha\beta}{5} - \frac{12\beta}{5} - \frac{\alpha}{5} + \frac{1}{10}\right)\mathcal{E}_{ij}\mathcal{I}_{ij}\right] + \frac{1}{2}\mathcal{E}_{ij}\frac{d\mathcal{I}_{ij}}{dt} \,. \qquad (4.48)
$$

Again, we have kept only the (external field)×(body field) cross terms. As expected, this expression reduces to the deDonder result (4.35) when $\alpha = \beta = \gamma = 0$. Using the same argument for Eq. (4.48) as for Eq. (4.35), we can conclude that the first term of Eq. (4.48) is the rate of change of the interaction energy between the tidal field and the body and that the second term represents the rate of work done by the external field on the body (the "tidal heating").

Notice the gauge dependence (dependence on α, β, γ) of the rate of change of interaction energy

$$
\frac{dE_{\rm int}}{dt} = \frac{d}{dt}\left[\left(\frac{7\alpha\gamma}{5} - \frac{9\gamma}{5} + \frac{7\alpha\beta}{5} - \frac{12\beta}{5} - \frac{\alpha}{5} + \frac{1}{10}\right)\mathcal{E}_{ij}\mathcal{I}_{ij}\right] \,. \qquad (4.49)
$$

By contrast, the "tidal heating" work done on the body has the same, gauge-invariant value as in Newtonian theory

$$
\frac{dW}{dt} = -\frac{1}{2}\mathcal{E}_{ij}\frac{d\mathcal{I}_{ij}}{dt} \,. \qquad (4.50)
$$

4.5 Conclusions

In this paper, we have shown that the rate of work done by an external tidal field on a body is independent of how gravitational energy is localized in Newtonian theory and that it is gauge invariant in general relativity. Furthermore, this quantity—which we are calling the "tidal heating"—is given unambiguously by Eq. (4.4). That the tidal heating should be a well-defined and precise quantity is reasonable, given that its physical effects have been observed in the form of volcanic activity of Jupiter's moon Io [2, 16, 17].

There remains one aspect of the uniqueness of the tidal heating that we have not explored: a

conceivable (but highly unlikely) dependence of dW/dt on the choice of energy-momentum pseudotensor in general relativity. The arbitrariness of the pseudotensor is general relativity's analog of Newtonian theory's arbitrariness of localization of gravitational energy. The fact that dW/dt is independent of the Newtonian energy localization suggests that it may also be independent of the general relativistic pseudotensor. In addition, the clear physical nature of dW/dt gives further confidence that it must be independent of the pseudotensor. Nevertheless, it would be worthwhile to verify explicitly that dW/dt is pseudotensor-independent.

4.6 Bibliography

[1] K. S. Thorne and J. B. Hartle, Phys. Rev. D, **31**, 1815 (1985).

[2] S. J. Peale, P. Cassen, and R. T. Reynolds, Science **203**, 894 (1979).

[3] C. W. Misner, K. S. Thorne and J. A. Wheeler, *Gravitation*, (W. H. Freeman, San Francisco, 1973).

[4] K. S. Thorne, Rev. Mod. Phys. **52**, 299 (1980).

[5] X.-H. Zhang, Phys. Rev. D, **34**, 991 (1986).

[6] X.-H. Zhang, Phys. Rev. D, **31**, 3130 (1985).

[7] K. S. Thorne, Phys. Rev. D, **58**, 124031 (1998).

[8] E. E. Flanagan, Phys. Rev. D, **58**, 124030 (1998).

[9] J. R. Wilson and G. J. Mathews, Phys. Rev. Lett. **75**, 4161 (1995).

[10] J. R. Wilson, G. J. Mathews and P. Maronetti, Phys. Rev. D **54**, 1317 (1996).

[11] G. J. Mathews, P. Maronetti, and J. R. Wilson, Phys. Rev. D **58**, 043003 (1998); gr-qc/9710140.

[12] For the explicit identification of an error in the Wilson-Mathews-Maronetti analysis, which presumably produced the stellar compression, see E. E. Flanagan, Phys. Rev. Lett. **82**, 1354 (1999); astro-ph/9811132.

[13] M. Favata, Phys. Rev. D **63**, 064013 (2001).

[14] B. A. Smith *et al.*, Science **204**, 951 (1979).

[15] L. A. Morabito *et al.*, Science **204**, 972 (1979).

[16] M. N. Ross and G. Schubert, Icarus **64**, 391 (1985).

[17] G. W. Ojakangas and D. J. Stevenson, Icarus **66**, 341 (1986).

[18] J. P. Cox and R. T. Giuli, *Principles of Stellar Structure* v.1, (Gordon and Breach, Science Publishers, New York, 1968).

[19] L. D. Landau and E. M. Lifshitz, *The Classical Theory of Fields* 2nd ed., (Addison-Wesley Publishing Company, Inc., Reading, Massachusetts, 1962).

[20] S. Chandrasekhar, Astrophys. J. **158**, 45 (1969).

Appendix A

FP Cavities as Optical Filters

As proposed by KLMTV [Sec. V B and Appendix C], Fabry-Perot cavities can be used as optical filters to achieve frequency-dependent homodyne detection. Here we shall briefly summarize and generalize their results.

Suppose we have one FP cavity of length $L_{\rm FP}$ and resonant frequency $\omega_0 - \xi_{\rm FP}\delta_{\rm FP}$. Also suppose this cavity has an input mirror with finite transmissivity $T_{\rm FP}$ and a perfect end mirror. When sideband fields at frequency $\omega_0 \pm \omega$ emerge from the cavity, they have a phase shift

$$\alpha_\pm \equiv 2\arctan(\xi_{\rm FP} \pm \omega/\delta_{\rm FP}) \,, \tag{A.1}$$

where

$$\delta_{\rm FP} = \frac{cT_{\rm FP}}{4L_{\rm FP}} \tag{A.2}$$

is the half bandwidth of the cavity. [Note that Eq. (A.1) is KLMTV Eqs. (88) and (C2), but a factor of 2 was missing from their equations. Fortunately, this appears to be a typographical error only in that particular equation; the factor of 2 is included in their subsequent calculations.] As a result of this phase shift, the input ($\tilde{b}_{1,2}$)–output ($b_{1,2}$) relation for sideband quadratures at frequency ω will be [KLMTV Eqs. (78)]

$$\begin{pmatrix} \tilde{b}_1 \\ \tilde{b}_2 \end{pmatrix} = e^{i\,\alpha_{\rm m}}\, \mathbf{R}_{\alpha_{\rm p}} \begin{pmatrix} b_1 \\ b_2 \end{pmatrix} \,, \tag{A.3}$$

where

$$\alpha_{\rm m} \equiv \frac{1}{2}(\alpha_+ - \alpha_-) \,, \quad \alpha_{\rm p} \equiv \frac{1}{2}(\alpha_+ + \alpha_-) \,, \tag{A.4}$$

and

$$\mathbf{R}_\phi \equiv \begin{pmatrix} \cos\phi & -\sin\phi \\ \sin\phi & \cos\phi \end{pmatrix} \,. \tag{A.5}$$

If a frequency-independent homodyne detection at phase shift θ follows the optical filter, the

measured quantity will be [KLMTV Eqs. (81) and (82)]

$$\tilde{b}_\theta = e^{i\alpha_m} b_\zeta \,, \tag{A.6}$$

where

$$\zeta(\omega) = \theta - \alpha_p \equiv \theta - \frac{1}{2}(\alpha_+ + \alpha_-) \,. \tag{A.7}$$

If more than one filter is applied in sequence (I, II, ...,) and followed by homodyne detection at angle θ, the measured quadrature will be [Eq. (83)]

$$\zeta(\omega) = \theta - \frac{1}{2}(\alpha_{I+} + \alpha_{I-} + \alpha_{II+} + \alpha_{II-} + \ldots) \,. \tag{A.8}$$

[Note that this $\zeta(\omega)$ (KLMTV's notation) is the same homodyne angle $\Phi(\omega)$ that we want to produce.] By adjusting the parameters ξ_J and δ_J, one might be able to achieve the FD homodyne phases needed. KLMTV worked out a particular case for their design [their Sec. V B, V C, and Appendix C].

Here we shall seek a more complete solution that works in a large class of situations. With the help of Eq. (A.1), Eq. (A.8) can be written in an equivalent form

$$\begin{aligned} \frac{1 + i\tan\zeta}{1 - i\tan\zeta} &= e^{2i\theta} \prod_{J=\mathrm{I,II},\ldots,s=\pm} \frac{1 - i\tan(\alpha_{Js}/2)}{1 + i\tan(\alpha_{Js}/2)} \,, \\ &= e^{2i\theta} \prod_{J=\mathrm{I,II},\ldots,s=\pm} \frac{\omega - s(-\xi_J\delta_J - i\delta_J)}{\omega - s(-\xi_J\delta_J + i\delta_J)} \,. \end{aligned} \tag{A.9}$$

Suppose the required $\tan\zeta(\omega)$ is a rational function in ω^2,

$$\tan\zeta(\omega) = \frac{\sum_{k=0}^{n} B_k \omega^{2k}}{\sum_{k=0}^{n} A_k \omega^{2k}} \,, \tag{A.10}$$

where A_k and B_k are real constants with $A_n^2 + B_n^2 > 0$. Then Eq. (A.9) requires that, for all ω,

$$\sum_{k=0}^{n} (A_k + iB_k)\omega^{2k} = D\, e^{i\theta} \prod_{J=\mathrm{I,II},\ldots,s=\pm} \Big[\omega - s(-\xi_J\delta_J - i\delta_J)\Big] \,, \tag{A.11}$$

where D can be any real constant. Equation (A.11) can be solved as follows. First, match the roots of the polynomials of ω on the two sides of the equation; denote these roots by $\pm\omega_J$ with $J = 1, 2, \ldots, n$. Then we can deduce that n filters are needed, and their complex resonant frequencies must be offset from ω_0 by

$$\omega_J = -\delta_J\xi_J - i\delta_J \,, \quad J = \mathrm{I, II}, \ldots \,, \tag{A.12}$$

where $\pm\omega_{\mathrm{I,II,...}}$ [with $\Im(\omega_J) > 0$] are the $2n$ roots of

$$\sum_{k=0}^{n}(A_k + iB_k)\,\omega^{2k}\,. \tag{A.13}$$

After this, the polynomials on the two sides of Eq. (A.11) can only differ by a complex coefficient whose argument determines θ. In fact, by comparing the coefficients of ω^{2n} on both sides, we have

$$\theta = \arg(A_{2n} + iB_{2n})\,. \tag{A.14}$$

Appendix B

Semi-Analytical Treatment of the Loss Terms

In this appendix, we present a semi-analytic treatment of each source of noise included in Sec. 3.6.1. We will use a notation similar to Eq. (3.12), but in matrix form:

$$\begin{pmatrix} \tilde{q}_1 \\ \tilde{q}_2 \end{pmatrix} = \begin{pmatrix} \tilde{q}_1 \\ \tilde{q}_2 \end{pmatrix}_{\text{lossless}} + \mathbf{N}_{\text{loss source}} , \tag{B.1}$$

where $\mathbf{N}_{\text{loss source}}$ is a vectorial representation of whichever source of loss we are considering at the moment. Each of these terms is associated with a vacuum field of the form $\sqrt{\mathcal{E}(\omega)}\tilde{n}(\omega)$ [cf. Eq. (3.50)], which enters the interferometer and increases the level of noise present. For generality, we let $\mathcal{E}(\omega)$ be frequency dependent. The (constant) characteristic fractional losses for each type of loss will be denoted by ε with an appropriate subscript. Each loss term appearing in Table 3.2 is presented in a subsection below.

B.1 Arms, Extraction Mirror, and Sloshing Cavity (AES)

The losses in the arms allow an unsqueezed vacuum field $\sqrt{\varepsilon_{\text{arm}}}\tilde{n}_{\text{arm}}$ to enter the optical train. By idealizing this field as arising entirely at the arm's end mirror, propagating the field through the interferometer to the output port, we obtain the following contribution to the output [cf. Eq. (3.50)]. The associated noise can be put into the following form

$$\mathbf{N}_{\text{arm}} = -\sqrt{\frac{\varepsilon_{\text{arm}}}{T_{\text{o}}}} \left[e^{i\psi} \frac{\omega\delta}{|\mathcal{L}(\omega)|} \begin{pmatrix} 1 & 0 \\ 0 & 1 \end{pmatrix} + e^{2i\psi} \begin{pmatrix} 0 & 0 \\ \kappa^*/2 & 0 \end{pmatrix} \right] \begin{pmatrix} \tilde{n}_{\text{arm1}} \\ \tilde{n}_{\text{arm2}} \end{pmatrix} , \tag{B.2}$$

where the vacuum operators from the two arms are combined as

$$\tilde{n}_{\text{arm}j} = \frac{\tilde{n}_{ej} - \tilde{n}_{nj}}{\sqrt{2}} . \tag{B.3}$$

The first term (independent of κ^*) is the shot-noise contribution, while the second term (proportional to κ^*) is the radiation-pressure noise. It turns out that several of the other loss sources $\mathcal{N}$ have a similar mathematical form.

We consider, specifically, the loss from the extraction mirror, which effectively allows $\sqrt{\varepsilon_{\rm ext}}\,\tilde{n}_{\rm ext}$ into the optical train. By propagating this field through the interferometer to the output port, we obtain the following contribution to the noise:

$$\mathbf{N}_{\rm ext} = \sqrt{\frac{\varepsilon_{\rm ext}}{T_{\rm o}}}\left[e^{i\psi}\frac{\omega\delta}{|\mathcal{L}(\omega)|}\begin{pmatrix}1&0\\0&1\end{pmatrix} + e^{2i\psi}\begin{pmatrix}0&0\\\kappa^*/2&0\end{pmatrix}\right]\begin{pmatrix}\tilde{n}_{\rm ext1}\\ \tilde{n}_{\rm ext2}\end{pmatrix}. \tag{B.4}$$

The loss from the sloshing cavity is a bit different: the imperfect end mirror of the sloshing cavity produces a vacuum noise field $\sqrt{\varepsilon_{\rm slosh}}\,\tilde{n}_{\rm slosh}$ which exits the cavity with the form

$$\sqrt{\frac{4\varepsilon_{\rm slosh}/T_{\rm s}}{1+\omega^2/(\delta_{\rm s}/2)^2}}\,e^{i\beta_{\rm s}}\tilde{n}_{\rm slosh\,1,2} \approx \sqrt{\varepsilon_{\rm slosh}}\frac{i\Omega}{\omega}\tilde{n}_{\rm slosh\,1,2}\,, \tag{B.5}$$

where $\beta_{\rm s} \equiv \arctan(2\omega/\delta_s) \approx \pi/2$ for most of the frequency band of interest. The associated noise is

$$\mathbf{N}_{\rm slosh} = -\sqrt{\frac{\varepsilon_{\rm slosh}}{T_{\rm o}}}\frac{i\Omega}{\omega}\left[e^{i\psi}\frac{\omega\delta}{|\mathcal{L}(\omega)|}\begin{pmatrix}1&0\\0&1\end{pmatrix} + e^{2i\psi}\begin{pmatrix}0&0\\\kappa^*/2&0\end{pmatrix}\right]\begin{pmatrix}\tilde{n}_{\rm slosh1}\\ \tilde{n}_{\rm slosh2}\end{pmatrix}. \tag{B.6}$$

Since the vacuum fields $\tilde{n}_{\rm arm}$, $\tilde{n}_{\rm ext}$, and $\tilde{n}_{\rm slosh}$ are independent and uncorrelated, we can effectively combine these four noises into a single expression

$$\mathbf{N}_{\rm AES} = \sqrt{\frac{\varepsilon_{\rm AES}}{T_{\rm o}}}\left[e^{i\psi}\frac{\omega\delta}{|\mathcal{L}(\omega)|}\begin{pmatrix}1&0\\0&1\end{pmatrix} + e^{2i\psi}\begin{pmatrix}0&0\\\kappa^*/2&0\end{pmatrix}\right]\begin{pmatrix}\tilde{n}_{\rm AES1}\\ \tilde{n}_{\rm AES2}\end{pmatrix}, \tag{B.7}$$

with

$$\varepsilon_{\rm AES} \sim \mathcal{E}_{\rm AES}(\omega) \equiv \varepsilon_{\rm arm} + \varepsilon_{\rm ext} + \varepsilon_{\rm slosh}\Omega^2/\omega^2\,. \tag{B.8}$$

We expect that $\varepsilon_{\rm arm} \sim \varepsilon_{\rm slosh} \sim \varepsilon_{\rm ext} \sim 2\times10^{-5}$, as discussed in the paragraph following Eq. (3.50) and as shown in Table 3.3.

B.2 Port-Closing Mirror

The imperfection of the closing mirror has two effects: (i) it introduces directly a fluctuation $-\sqrt{\varepsilon_{\rm close}R_{\rm o}}\,\tilde{n}_{\rm close}$ into the output, giving a shot noise

$$\mathbf{N}^{\rm shot\,direct}_{\rm close} = -\sqrt{\varepsilon_{\rm close}R_{\rm o}}\begin{pmatrix}\tilde{n}_{\rm close1}\\ \tilde{n}_{\rm close2}\end{pmatrix}; \tag{B.9}$$

and (ii) it introduces a fluctuation $\sqrt{\varepsilon_{\rm close}T_{\rm o}}\,\tilde{n}_{\rm close}$ into the light that passes from the arms into the sloshing cavity, giving (after propagation through the sloshing cavity and interferometer and into the output):

$$\mathbf{N}^{\rm indirect}_{\rm close} = -\sqrt{\varepsilon_{\rm close}}\left[e^{i\psi}\frac{\omega\delta}{|\mathcal{L}(\omega)|}\begin{pmatrix}1&0\\0&1\end{pmatrix} + e^{2i\psi}\begin{pmatrix}0&0\\\kappa^*/2&0\end{pmatrix}\right]\begin{pmatrix}\tilde{n}_{\rm close1}\\ \tilde{n}_{\rm close2}\end{pmatrix}. \tag{B.10}$$

Combining these two expressions gives, to leading order (in the various transmissivities and the small parameters $\omega L/c$ and $\varepsilon_{\rm close}$),

$$\mathbf{N}_{\rm close} = \sqrt{\varepsilon_{\rm close}}\left[ie^{i\psi}\frac{\Omega^2-\omega^2}{|\mathcal{L}(\omega)|}\begin{pmatrix}1&0\\0&1\end{pmatrix} - e^{2i\psi}\begin{pmatrix}0&0\\\kappa^*/2&0\end{pmatrix}\right]\begin{pmatrix}\tilde{n}_{\rm close1}\\ \tilde{n}_{\rm close2}\end{pmatrix}. \tag{B.11}$$

Since $\varepsilon_{\rm close}$ is simply the loss from the port-closing mirror itself, we can assume that $\varepsilon_{\rm close} \lesssim 2\times10^{-5}$. Then, this and the above expression (B.11) show that the output noise from the closing mirror is $T_{\rm o}$ times smaller than the AES loss [Eq. (B.8)].

B.3 The RSE Cavity

The losses in the region between the internal mirrors and the RSE mirror, i.e., the RSE cavity, are more complicated than the previous cases. As before, we suppose that, during each propagation from one end to the other of the RSE cavity, a fraction $\varepsilon_{\rm RSE}$ of the light power is dissipated and replaced by a corresponding vacuum field, $\sqrt{\varepsilon_{\rm RSE}}\,\tilde{n}_{\rm in}$ or $\sqrt{\varepsilon_{\rm RSE}}\,\tilde{n}_{\rm out}$ (depending whether the light is propagating in towards the arms or out towards the extraction mirror and sloshing cavity). These two fields $\tilde{n}_{\rm in}$ and $\tilde{n}_{\rm out}$ are independent vacuum fields. At the leading order in $\varepsilon_{\rm RSE}$, we have a modified version of the "input–output" relation for the RSE cavity:

$$\begin{pmatrix}B\\D\end{pmatrix} = \begin{pmatrix}1-\frac{1+R_{\rm i}}{2T_{\rm i}}\varepsilon_{\rm RSE} & \frac{\sqrt{R_{\rm i}}}{T_{\rm i}}\varepsilon_{\rm RSE}\\ \frac{\sqrt{R_{\rm i}}}{T_{\rm i}}\varepsilon_{\rm RSE} & 1-\frac{1+R_{\rm i}}{2T_{\rm i}}\varepsilon_{\rm RSE}\end{pmatrix}\begin{pmatrix}A\\C\end{pmatrix} + \sqrt{\frac{\varepsilon_{\rm RSE}}{T_{\rm i}}}\begin{pmatrix}1&-\sqrt{R_{\rm i}}\\-\sqrt{R_{\rm i}}&1\end{pmatrix}\begin{pmatrix}\tilde{n}_{\rm in}\\ \tilde{n}_{\rm out}\end{pmatrix}, \tag{B.12}$$

where A, B, C, D are the field amplitudes shown in Fig. 3.3. Note that, for simplicity, we are looking at only one arm; we could equally well use the other (substituting $B \to F$ and $C \to G$) or the proper combination of both. Also, notice that if $\varepsilon_{\rm RSE} = 0$, then we find $B = A$ and $D = C$, which illustrates the fact that the internal and RSE mirrors have no effect on the sidebands (described in Sec. 3.2 where we introduced the RSE mirror).

From Eq. (B.12), we find that the loss inside the RSE cavity has two effects. First, it makes the cancellation of the effect of the internal and the RSE mirrors imperfect. (Recall that an RSE mirror with the same transmissivity as the internal mirrors effectively cancels the effect of the internal

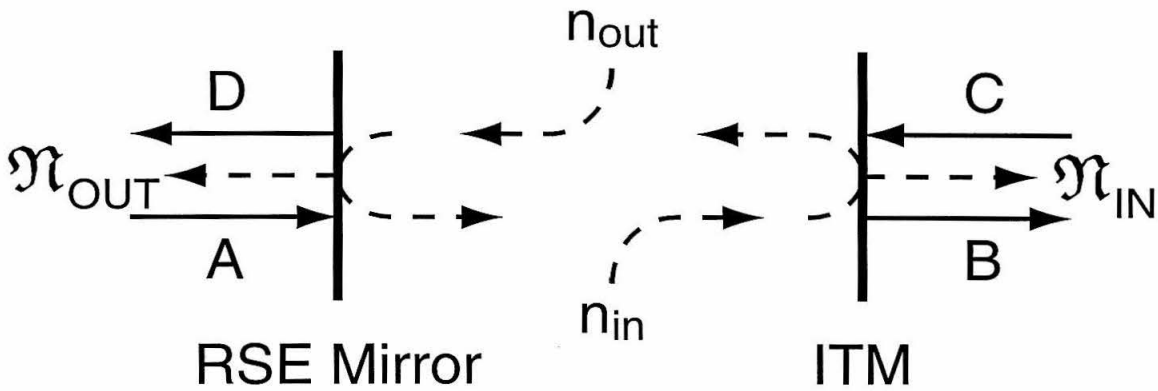

Figure B.1: Schematic diagram of a simplified version of the RSE cavity. The quantities $\tilde{n}_{\rm in}$ and $\tilde{n}_{\rm out}$ enter inside the RSE cavity, whereas $\mathfrak{N}_{\rm in}$ and $\mathfrak{N}_{\rm out}$ are external to the cavity and exist in different locations.

mirrors on the sidebands; this was discussed in Sec. 3.2.) This imperfect cancellation will not be important in our situation. Indeed, there is no corresponding term appearing in the input–output relation given in Eq. (3.51).

Secondly, the loss inside the RSE cavity adds two vacuum fields to light that travels through the RSE cavity in opposite directions [i.e., from A to B (IN) and from C to D (OUT)]. We denote them by

$$\tilde{\mathfrak{N}}_{\rm IN} \equiv \sqrt{\frac{\varepsilon_{\rm RSE}}{T_{\rm i}}}(\tilde{n}_{\rm in} - \sqrt{R_{\rm i}}\tilde{n}_{\rm out})\,, \tag{B.13a}$$

$$\tilde{\mathfrak{N}}_{\rm OUT} \equiv \sqrt{\frac{\varepsilon_{\rm RSE}}{T_{\rm i}}}(-\sqrt{R_{\rm i}}\tilde{n}_{\rm in} + \tilde{n}_{\rm out})\,. \tag{B.13b}$$

Note that $\tilde{n}_{\rm in}$ and $\tilde{n}_{\rm out}$ arise *inside* the RSE cavity as a result of the loss that occurred there and that $\tilde{\mathfrak{N}}_{\rm IN}$ and $\tilde{\mathfrak{N}}_{\rm OUT}$ are the vacuum fluctuations *emerging* from the RSE cavity. As a result, $\tilde{\mathfrak{N}}_{\rm IN}$ and $\tilde{\mathfrak{N}}_{\rm OUT}$ *exist in different locations:* $\tilde{\mathfrak{N}}_{\rm IN}$ denotes the vacuum field inside the arm cavity with B, and $\tilde{\mathfrak{N}}_{\rm OUT}$ denotes the vacuum field at the RSE mirror, heading towards the extraction mirror and sloshing cavity with D. This is depicted in Fig. B.1.

The fields $\tilde{\mathfrak{N}}_{\rm IN}$ and $\tilde{\mathfrak{N}}_{\rm OUT}$ both have a power spectral density a factor $\sim 1/T_{\rm i}$ larger than the one-time loss coefficient. This can be explained by the fact that the sideband light bounces back and forth inside the RSE cavity roughly $\sim 1/T_{\rm i}$ times before exiting. As a result, the (power) loss coefficient is amplified by the same factor. However, since these fields are quite correlated (both contain similar amounts of $\tilde{n}_{\rm in}$ and $\tilde{n}_{\rm out}$), we need to analyze them carefully.

For the shot noise, we need to find the amplitude of the vacuum fluctuations that the loss introduces into the output. To understand the effect of this type of loss, we ask how much vacuum fluctuation is added to the field D by $\tilde{\mathfrak{N}}_{\rm IN}$ and $\tilde{\mathfrak{N}}_{\rm OUT}$. The answer is obtained by propagating $\tilde{\mathfrak{N}}_{\rm IN}$

one round trip inside the interferometer's arm(s) and then combining it with $\tilde{\mathfrak{N}}_{\rm OUT}$. This gives

$$\begin{aligned} D &\rightarrow D + \left[\tilde{\mathfrak{N}}_{\rm OUT} + e^{2i\omega L/c}\tilde{\mathfrak{N}}_{\rm IN}\right] \\ &\approx D + \sqrt{\frac{\varepsilon_{\rm RSE}T_{\rm i}}{4}\left(1+\frac{\omega^2}{\delta_{\rm i}^2}\right)}\left(e^{i\beta_{\rm i}}\tilde{n}_{\rm in} + e^{-i\beta_{\rm i}}\tilde{n}_{\rm out}\right), \end{aligned} \tag{B.14}$$

where $\delta_{\rm i} \equiv T_{\rm i}c/4L$ and $\beta_{\rm i} \equiv \arctan(\omega/\delta_{\rm i})$. Propagating this to the output, we get the shot noise contribution to be

$$\mathrm{N}^{\rm shot}_{\rm RSE} = \sqrt{\frac{\varepsilon_{\rm RSE}T_{\rm i}}{4T_{\rm o}}\left(1+\frac{\omega^2}{\delta_{\rm i}^2}\right)}e^{i\psi}\frac{\omega\delta}{|\mathcal{L}(\omega)|}\left[e^{+i\beta_{\rm i}}\begin{pmatrix}\tilde{n}_{\rm in1}\\ \tilde{n}_{\rm in2}\end{pmatrix} + e^{-i\beta_{\rm i}}\begin{pmatrix}\tilde{n}_{\rm out1}\\ \tilde{n}_{\rm out2}\end{pmatrix}\right]. \tag{B.15}$$

This noise is not of the magnitude that Eqs. (B.13) would appear to indicate. Instead of having a coefficient of $\sim \sqrt{\varepsilon_{\rm RSE}/T_{\rm i}}$, it has a much smaller value when $\omega \lesssim \delta_{\rm i}$. The reason is that the two vacuum fluctuations traveling in opposite directions are anticorrelated and largely cancel each other, since they are summed in the outgoing field D. This cancellation becomes less perfect as ω grows and becomes much larger than $\delta_{\rm i}$. This effect is shown in Fig. 3.11.

For the RSE contribution to the radiation-pressure noise, we are interested in how much the two noise fields $\tilde{\mathfrak{N}}_{\rm IN}$ and $\tilde{\mathfrak{N}}_{\rm OUT}$ contribute to the carrier amplitude fluctuation *at the position of the test masses*. Therefore, we ask what the sum of $\tilde{\mathfrak{N}}_{\rm IN}$ and $\tilde{\mathfrak{N}}_{\rm OUT}$ is when they combine at the end mirrors of the arm cavities. Since $\tilde{\mathfrak{N}}_{\rm OUT}$ is superposed on D, $\tilde{\mathfrak{N}}_{\rm OUT}$ must be propagated through the sloshing cavity and back to the arm cavity, where it is combined with $\tilde{\mathfrak{N}}_{\rm IN}$. There is a phase factor of $e^{i\omega L/c}$ due to the propagation from the internal mirror to the end mirror (in addition to the phases acquired on the way to and inside the sloshing cavity; these are explained below), producing

$$\begin{aligned} B &\rightarrow B + e^{i\omega L/c}\left[\tilde{\mathfrak{N}}_{\rm IN} - \tilde{\mathfrak{N}}_{\rm OUT}(1-T_{\rm o})\frac{e^{2i\beta_{\rm s}}}{1-T_{\rm o}e^{2i\beta_{\rm s}}}\right] \\ &\approx B + 2T_{\rm o}\sqrt{\frac{\varepsilon_{\rm RSE}}{T_{\rm i}}}\left[\frac{\omega(\delta_{\rm i}+\delta)+i\Omega^2}{\omega\delta}\tilde{n}_{\rm in} + \frac{\omega(\delta_{\rm i}-\delta)-i\Omega^2}{\omega\delta}\tilde{n}_{\rm out}\right]. \end{aligned} \tag{B.16}$$

where $\beta_{\rm s} = \arctan(2\omega/\delta_{\rm s})$ is the phase associated with the sloshing cavity. Propagating the new B to the output produces a radiation-pressure contribution

$$\begin{aligned} \mathrm{N}^{\rm rad\,pres}_{\rm RSE} &= \sqrt{\frac{\varepsilon_{\rm RSE}T_{\rm o}}{T_{\rm i}}}e^{2i\psi}\begin{pmatrix}0 & 0\\ -\kappa^* & 0\end{pmatrix} \\ &\quad\times\left[\frac{\omega(\delta_{\rm i}+\delta)+i\Omega^2}{\omega\delta}\begin{pmatrix}\tilde{n}_{\rm in1}\\ \tilde{n}_{\rm in2}\end{pmatrix} + \frac{\omega(\delta_{\rm i}-\delta)-i\Omega^2}{\omega\delta}\begin{pmatrix}\tilde{n}_{\rm out1}\\ \tilde{n}_{\rm out2}\end{pmatrix}\right]. \end{aligned} \tag{B.17}$$

As before, this noise does not have a magnitude $\sim \sqrt{\varepsilon_{\rm RSE}/T_{\rm i}}$; it is much smaller. The reason is that

when $\tilde{\mathfrak{N}}_{\rm OUT}$ travels to the sloshing cavity and back to the arms, it gains two phase shifts. First is a constant phase shift of π, due to the distance it traveled (twice) between the RSE and sloshing mirror. The other is from the sloshing cavity, where for frequencies much larger than the bandwidth $\delta_{\rm s}$ of the sloshing cavity, this phase shift is roughly π. Adding these two phase shifts, $\tilde{\mathfrak{N}}_{\rm OUT}$ will appear roughly unchanged when it combines with $\tilde{\mathfrak{N}}_{\rm IN}$ in the arm cavity. Since these two vacuum fields are anticorrelated, there is again an effective cancellation between the two noises at frequencies above $\delta_{\rm s}$. This cancellation becomes less complete at low frequencies; see Fig. 3.11.

We assume the fractional loss $\varepsilon_{\rm RSE} \sim 2 \times 10^{-5}$, since it arises primarily from losses in the RSE cavity's optical elements (mirrors and beam splitter). (See Appendix C for a discussion of the noise due to mode mismatching, which we do not consider here.)

B.4 Detection and Filter Cavities

First, we consider the losses involved in the detection of the signal (without filter cavities). Two important sources of photon loss are mode mismatching associated with the local oscillator used for frequency-independent homodyne detection ($\varepsilon_{\rm lo}$) and the inefficiency of the photodiode ($\varepsilon_{\rm pd}$). In a squeezed-input speed meter, there will also be a circulator (with fractional loss $\varepsilon_{\rm circ}$) through which the squeezed vacuum is fed into the system and through which the output light will have to pass. These losses have no frequency dependence, so they are modeled by an equation of the form of [Eq. (3.50)] with

$$\mathcal{E}_{\rm OPC}(\omega) = \varepsilon_{\rm OPC} = \varepsilon_{\rm lo} + \varepsilon_{\rm pd} + \varepsilon_{\rm circ} \tag{B.18}$$

[cf. KLMTV Eq. (104)]. The contribution to the noise is then

$$\mathbf{N}_{\rm OPC} = \sqrt{\varepsilon_{\rm OPC}} \begin{pmatrix} \tilde{n}_{\rm OPC1} \\ \tilde{n}_{\rm OPC2} \end{pmatrix} , \tag{B.19}$$

where the $\tilde{n}_{{\rm OPC}j}$ are linear combinations of the individual (independent) vacuum fields entering at each location (so the spectral densities of these fields are unity and there are no cross-correlations) and propagated to the output port. KLMTV assumed that each of these losses is about 0.001, giving $\varepsilon_{\rm OPC} \sim 0.003$.

We next turn our attention to optical filters on the output (as in the case of frequency-dependent homodyne detection for a squeezed-variational speed meter, discussed in Sec. 3.5.2). Such cavities will have losses that may contribute significantly to the noises of QND interferometers, as has been seen in KLMTV. In their Sec. VI, KLMTV carried out a detailed analyses of such losses; our investigation is essentially the same as theirs.

The loss in the optical filters can come from scattering or absorption in the cavity mirrors, which

can be modeled by attributing a finite transmissivity T_e to the end mirrors, as we did for the arm cavities. The effect of lossy filters is again analogous to [Eq. (3.50)]. This time the loss coefficient $\mathcal{E}_F(\omega)$ does have some frequency dependence:

$$\mathcal{E}_F = 2\varepsilon_{mm} + \sum_{J=I,II} \bar{\mathcal{E}}_J = 2\varepsilon_{mm} + \frac{1}{2} \sum_{J=I,II} (\mathcal{E}_{J+} + \mathcal{E}_{J-}) , \tag{B.20}$$

where $\varepsilon_{mm} \sim 0.001$ is the mode-mismatching into each filter cavity and where

$$\mathcal{E}_{J\pm} = \frac{4T_e}{T_J\,[1 + (\pm\omega/\delta_J - \xi_J)^2]} \tag{B.21}$$

are the loss coefficents of the two different filter cavities ($J = I, II$) [cf. Eqs. (103) and (106) of KLMTV]. The noise contribution is

$$\mathbf{N}_F = \sqrt{\mathcal{E}_F} \begin{pmatrix} \tilde{n}_{F1} \\ \tilde{n}_{F2} \end{pmatrix} . \tag{B.22}$$

The weak frequency-dependence of $\mathcal{E}_F$ will be neglected (as KLMTV did), giving

$$\varepsilon_F \simeq \mathcal{E}_F \sim 0.005 \tag{B.23}$$

[cf. Eqs. (107) and (104) of KLMTV]. The value of ε_F may vary slightly for the different optimizations we have used, but it remains less than 0.006.

Appendix C

Effects due to Mode-Mismatching: A Simple Analysis

In the practical implementation of GW interferometers, the mismatching of spatial modes between different optical cavities will degrade the sensitivity because signal power will be lost into higher-order modes and, correspondingly, vacuum noises from those modes will be introduced to the signal. In a way, this is similar to other sources of optical loss discussed in the previous appendix. However, the higher-order modes do not simply get dissipated — they too will propagate inside the interferometer (although with a different propagation law). As a consequence, the exchange of energy between fundamental and higher modes due to mode-mismatching is *coherent*, and the formalism we have been using for the loss does not apply. In this section, we shall extend our formalism to include one higher-order mode and give an extremely simplified model of the mode-mismatching effects[1].

In a conventional interferometer (LIGO-I), the mode-mismatching comes predominantly from the mismatch of the mirror shapes between the two arms, which makes the wavefronts from the two arms different at the beam splitter. In particular, the cancellation of the carrier light at the dark port is no longer perfect, and additional (bright-port) noises are introduced into the dark-port output. For our speed meter, a third cavity—the sloshing cavity—has to be matched to the two arm cavities, further complicating the problem.

In order to simplify the situation, we approximate all the waves propagating in the corner station (the region near the beam splitter, where the distances are short enough that) as following the same phase-propagation law as a plane wave. The only possible source of mismatch is assumed to come from the difference of wavefront shapes (to first order in the fractional difference of the radii of curvature) and waist sizes for the light beams emerging from the two arm cavities and the sloshing cavity. Suppose, in the region of the corner station, we have a fiducial fundamental Gaussian mode $\Psi^{(0)}$ (which is being pumped by the carrier) with waist size w_0 and wavefront curvature $\alpha_0 \equiv 1/R_0$

[1]This way of modeling the mode-mismatching effects was suggested to us by Stan Whitcomb.

that is roughly the same as those of the three cavities[2]:

$$\Psi^{(0)}(x,y) \propto \frac{1}{w_0} \exp\left(-\frac{\rho^2}{w_0^2} + ik\frac{\alpha_0\rho^2}{2}\right), \quad \rho = \sqrt{x^2+y^2}. \tag{C.1}$$

At leading order in the mismatches, the fundamental modes of the three cavities (in the region of the corner station), which have waist sizes w_J and curvatures $\alpha_J \equiv 1/R_J$ [J =n, e, or slosh (for the north arm, east arm, and sloshing cavity, respectively)], can be written in the form:

$$\begin{aligned}\Psi^{J}_{\rm fnd}(x,y) \;\propto\; & \frac{1}{w_0} \exp\left(ikw_0^2\,\frac{\alpha_J-\alpha_0}{4}\right) \exp\left(-\frac{\rho^2}{w_0^2} + ik\frac{\alpha_0\rho^2}{2}\right) \\ & \times\left\{1 + \left(\frac{w_J-w_0}{4w_0} + ikw_0^2\frac{\alpha_J-\alpha_0}{16}\right)\left[H_2\left(\frac{\sqrt{2}x}{w_0}\right) + H_2\left(\frac{\sqrt{2}y}{w_0}\right)\right]\right\},\end{aligned} \tag{C.2}$$

where $H_2(u)$ is the second-order Hermite polynomial of u. This $\Psi^{J}_{\rm fnd}(\pi,y)$ can be expressed as $\Psi^{(0)}$ plus a small admixture of a higher-order mode $\Psi^{(1)}$, which consists of equal amounts of TEM_{02} and TEM_{20} modes [and thus is orthogonal to $\Psi^{(0)}$]. This admixture changes the waist size from ω_0 to ω_J and the curvature from α_0 to α_J. We can choose our fiducial fundamental mode $\Psi^{(0)}$ in such a way that the two arm cavities have an opposite mismatch with it, i.e., $\alpha_n + \alpha_e = 2\alpha_0$, $w_n + w_e = 2w_0$, and at leading order,

$$\begin{pmatrix} \Psi^{n,e}_{\rm fnd} \\ \Psi^{n,e}_{\rm exc} \end{pmatrix} = \begin{pmatrix} 1 & \pm\mu_{\rm arm} \\ \mp\mu^*_{\rm arm} & 1 \end{pmatrix} \begin{pmatrix} \Psi^{(0)} \\ \Psi^{(1)} \end{pmatrix}, \tag{C.3}$$

where "exc" denotes the excited mode and the admixing amplitude $\mu_{\rm arm}$ is, in general, complex. We also denote the fundamental and excited modes of the sloshing cavity as

$$\begin{pmatrix} \Psi^{\rm slosh}_{\rm fnd} \\ \Psi^{\rm slosh}_{\rm exc} \end{pmatrix} = \begin{pmatrix} 1 & \mu_{\rm slosh} \\ -\mu^*_{\rm slosh} & 1 \end{pmatrix} \begin{pmatrix} \Psi^{(0)} \\ \Psi^{(1)} \end{pmatrix}; \tag{C.4}$$

again, $\mu_{\rm slosh}$ can be complex. We shall also assume that the higher-order modes involved here are far from resonance inside the cavities and will be rejected by them, gaining a phase of π upon reflection from each cavity's input mirror. In the output, we assume the mode $\Psi^{(0)}$ is selected for detection. (The local oscillator associated with the homodyne detection is chosen to have the same spatial mode as $\Psi^{(0)}$, thereby "selecting" $\Psi^{(0)}$. Note that the potential mode-mismatch effect here is already taken into account in the fractional loss $\varepsilon_{\rm lo}$ of the local oscillator, as described in Sec. B.4.)

Quite naturally, we have to introduce two sets of quadrature operators to describe the two modes.

[2]We have chosen to use the curvature instead of the radius of curvature because in this region the wavefronts are very flat.

For example, for the field $P(\zeta)$ entering through the extraction mirror, we have

$$\tilde{\mathbf{p}}^{(0)} \equiv \begin{pmatrix} \tilde{p}_1^{(0)} \\ \tilde{p}_2^{(0)} \end{pmatrix}, \quad \tilde{\mathbf{p}}^{(1)} \equiv \begin{pmatrix} \tilde{p}_1^{(1)} \\ \tilde{p}_2^{(1)} \end{pmatrix}. \tag{C.5}$$

For each of the three cavities, we have to decompose the optical field into its own fundamental and excited modes, propagate them separately and then combine them. The input–output (a–b) relation of one of the cavities with mirrors held fixed can be written as

$$\begin{pmatrix} \tilde{\mathbf{b}}^{(0)} \\ \tilde{\mathbf{b}}^{(1)} \end{pmatrix} = \left[e^{i\Phi_{\rm fnd}} \mathbf{P}_{\rm fnd} + e^{i\Phi_{\rm exc}} \mathbf{P}_{\rm exc} \right] \begin{pmatrix} \tilde{\mathbf{a}}^{(0)} \\ \tilde{\mathbf{a}}^{(1)} \end{pmatrix}, \tag{C.6}$$

where

$$\mathbf{P}_{\rm fnd} = \begin{pmatrix} 1 \\ \mu \end{pmatrix} \begin{pmatrix} 1 & \mu^* \end{pmatrix}, \quad \mathbf{P}_{\rm exc} = \begin{pmatrix} -\mu^* \\ 1 \end{pmatrix} \begin{pmatrix} -\mu & 1 \end{pmatrix}, \tag{C.7}$$

are the projection operators, and $\Phi_{\rm fnd}$ and $\Phi_{\rm exc} = \pi$ are the phases gained by the fundamental mode and excited mode after being reflected back by the cavity.

The mode-mismatching can cause both shot and radiation pressure noises at the output, giving:

$$\tilde{\mathbf{q}}^{(0)} \to \tilde{\mathbf{q}}^{(0)} + \mathbf{N}_{\rm MM}^{\rm shot} + \mathbf{N}_{\rm MM}^{\rm rad\,pres}. \tag{C.8}$$

Assuming the mirrors are held fixed and applying the new input–output relations (C.6) of the non-perfect cavities, we get the following shot noise in the output (to leading order in $\mu_{\rm arm}$ and $\mu_{\rm slosh}$):

$$\begin{aligned} \mathbf{N}_{\rm MM}^{\rm shot} &= -e^{i\psi} \mu_{\rm arm}^* \sqrt{\frac{4}{T_{\rm o}}} \frac{\sqrt{T_{\rm p}}}{1+\sqrt{1-T_{\rm p}}} \frac{1-\sqrt{1-T_{\rm i}}}{\sqrt{T_{\rm i}}} \frac{\omega\delta}{|\mathcal{L}(\omega)|} \tilde{\mathbf{i}}^{(1)} \\ &\approx e^{-i\psi} \mu_{\rm arm}^* \sqrt{\frac{T_{\rm i} T_{\rm p}}{4T_{\rm o}}} \frac{\omega\delta}{|\mathcal{L}(\omega)|} \tilde{\mathbf{i}}^{(1)}; \end{aligned} \tag{C.9}$$

see Eq. (B.1). The quantity $\tilde{\mathbf{i}}^{(1)}$ refers to the excited mode of the noise coming in the bright port [$I(\zeta)$ in Fig. 3.3].

The main results embedded in Eq. (C.9) are

(i) the mode-mismatching with the sloshing cavity does not give any contribution at leading order in μ, and

(ii) the mode-mismatching shot noise comes from the higher-order mode entering from the *bright port*, strongly suppressed by the presence of the internal and power-recycling mirrors.

These two effects are both due to the coherent interaction between the fundamental ($\Psi^{(0)}$) and excited ($\Psi^{(1)}$) modes (of our idealized cavity), in which energy is not simply dissipated from $\Psi^{(0)}$

but exchanged coherently between the two modes as the light flows back and forth between the sloshing cavity and the arm cavities. Detecting an appropriate linear combination of the two modes can then be expected to reverse the effect of mode mismatching. In our case, the properties of the cavities are carefully chosen such that $\Psi^{(0)}$ itself is the desired detection mode (for the sloshing mismatch). Consequently, the mode mismatching with the sloshing cavity does not contribute at leading order [item (i) above]. Regarding item (ii), the mismatch of the two arm cavities does give rise to an additional noise, but it can only come from the higher mode in the bright port, because at leading order in mismatches, (a) the propagation of $\Psi^{(0)}$ from the bright port to the dark port is suppressed and (b) there is no propagation of dark-port $\Psi^{(1)}$ into dark-port $\Psi^{(0)}$ since we have chosen $\Psi^{(0)}$ in such a way that the two arm cavities have exactly opposite mismatches with it.

The reason why this noise is suppressed by the factor $1/T_{\rm p}$ is simple: because $\Psi^{(1)}$ is not on resonance with the composite cavity formed by the power-recycling mirror and the arm cavities, its fluctuations inside the system (like its classical component) are naturally suppressed by a factor $1/\sqrt{T_{\rm p}}$ compared to the level outside the cavity. The reason for the factor of $1/T_{\rm i}$ is similar: the $\Psi^{(1)}$ mode does not resonate within the system formed by the arm cavities and the RSE mirror and will consequently be suppressed.

By computing at the fields at the end mirrors and from them the fluctating radiation pressure, we obtain the radiation-pressure noise due to mode-mismatching:

$$\mathbf{N}_{\rm MM}^{\rm rad\,pres} = -\frac{e^{2i\psi}}{2}\mu_{\rm arm}^{*}\sqrt{\frac{T_{\rm i}T_{\rm p}}{4T_{\rm o}}}\begin{pmatrix} 0 & 0 \\ -\kappa^{*} & 0 \end{pmatrix}\tilde{\mathbf{i}}^{(1)}\,. \tag{C.10}$$

This radiation-pressure noise is suppressed by a factor similar to the shot noise.

By comparing Eqs. (C.9) and (C.10) with, e.g., Eqs. (B.7), we see that mode mismatching produces noise with essentially the same form as optical-element losses from the arms, extraction mirror and sloshing cavity (AES), with (assuming the input laser is shot-noise limited in the higher modes)

$$\varepsilon_{\rm MM} = \frac{T_{\rm i}T_{\rm p}}{4}|\mu_{\rm arm}^{*}|^{2}\,. \tag{C.11}$$

The factor $T_{\rm i}T_{\rm P}/4$ happens to be the ratio between the input power (at the power-recycling mirror) and the circulating power, which will be $\sim 10^{-4}$. Suppose $\Re(\mu_{\rm arm}) \sim \Im(\mu_{\rm arm}) \sim 0.03$. The effect of mode-mismatching will then be much less significant (*in our simple model*) than the losses from the optical elements.

It should be evident that other imperfections in the cavity mirrors, which cause admixtures of other higher-order ("excited") modes, will lead to similar "dissipation factors," $\mathcal{E}_{\rm MM} \sim \frac{T_{\rm i}T_{\rm p}}{4}|\mu_{\rm arm}^{*}|^{2}$. For this reason, we expect mode mismatching to contribute negligibly to the noise, and we ignore it in the body of the paper.

Appendix D

Transmissivity Mismatch between the Internal Mirror and the RSE Mirror

Recall from Sec. 3.2 that when the internal and RSE mirrors have the same transmissivity, their effects on the gravity-wave sideband cancel. If, however, the transmissivity of the internal mirror, $T_{\rm i}$, is not perfectly matched by that of the RSE mirror, $T_{\rm RSE}$, then this cancellation will no longer be perfect. As a result, the RSE cavity (i.e., the cavity between the internal and RSE mirrors) will have the same effect as an additional mirror (with a small reflectivity). Suppose the transmissivity of this effective mirror is $T_{\rm RSE} = (1 + \varepsilon_{\rm RSE})T_{\rm i}$. Then a simple calculation yields its (amplitude) reflectivity:

$$\mu = \frac{\sqrt{1-T_{\rm i}} - \sqrt{1-T_{\rm RSE}}}{1 - \sqrt{1-T_{\rm i}}\sqrt{1-T_{\rm RSE}}} \approx \frac{\varepsilon_{\rm RSE}}{2\sqrt{1-T_{\rm i}}} \approx \frac{\varepsilon_{\rm RSE}}{2} \,. \tag{D.1}$$

Adding this effective mirror with reflectivity μ to our interferometer yields a new set of input–output relations similar to Eq. (3.12), but with modified κ and ψ. The functional form of κ can be maintained by appropriately redefining the quantities Ω and δ. To leading order in μ, we obtain

$$\kappa \to \kappa_{\rm TM} = \frac{\Omega_{\rm I}^3 \delta_{\rm TM}}{(\omega^2 - \Omega_{\rm TM}^2)^2 + \omega^2 \delta_{\rm TM}^2} \,, \tag{D.2}$$

with

$$\Omega \to \Omega_{\rm TM} = (1-\mu)\Omega \,, \quad \delta \to \delta_{\rm TM} = (1-2\mu)\delta \,. \tag{D.3}$$

Consequently, we can re-optimize the system to compensate for this transmissivity-mismatch effect.